Water effects on the interaction and friction between polar surfaces

im Fachbereich Physik der Freien Universität Berlin eingereichte
Dissertation

zur Erlangung des akademischen Grades eines Doktors der
Naturwissenschaften (Dr. rer. nat.)

vorgelegt von
Alexander Schlaich

Berlin, 2017

Erster Gutachter:	Prof. Dr. Roland R. Netz Freie Universität Berlin
Zweiter Gutachter:	Prof. Dr. Joachim Dzubiella Helmholtz-Zentrum Berlin für Materialien und Energie & Humboldt-Universität zu Berlin
Tag der Disputation:	10.11.2017

Abstract

The effects of water on the interaction and friction between surfaces are important both in biological and technological systems. For a quantitative description, the molecular details require modeling of all relevant degrees of freedom. The aim of this work is to obtain atomistic information from Molecular Dynamics simulations and incorporate them into continuum models, which are extended where necessary. Throughout this work we study interactions between water-separated surfaces, which requires control of the water chemical potential.

First, we study the dielectric properties of water confined between flexible polar groups, which reveals a highly asymmetric behavior at separations below 1 nm: while the component of the dielectric permittivity parallel to the surface slightly increases compared to bulk, the perpendicular one drastically decreases due to the anti-correlated polarization of neighboring water molecules. The obtained molecular information is incorporated into a tensorial box-model suitable for coarse-grained electrostatic modeling.

Second, we investigate the origin of the overwhelmingly repulsive hydration force that universally acts between hydrated surfaces. We model the indirect, water–mediated forces in terms of a Landau–Ginzburg free energy and obtain all phenomenological parameters from the simulations. We find that polarization related order parameters quantitatively describe the decay length of the indirect pressures, but only account for about ten percent of the amplitude, which we attribute to effects that are not captured within the one-dimensional mean-field model. Contributions from other order parameters are negligible.

Third, we compare the pressure as a function of separation between uncharged and charged surfaces with neutralizing counterions. At separations larger than 0.5 nm and at low surface charge, we find that the continuum Poisson–Boltzmann model accounts for the additional pressures. For small separations, the ion–surface repulsion is dominating. Our simulations at controlled chemical potential offer the possibility to investigate such effects in explicit water for the first time.

Last, we study the shear friction between polar surfaces in the linear response regime at low shearing velocity, which is the relevant regime for typical biological applications. With decreasing water film thickness we find three consecutive friction regimes: For thick films friction is governed by bulk water viscosity. At separations of about a nanometer the highly viscous interfacial water layers dominate and increase the surface friction, while at the transition to the dry friction limit interfacial slip sets in. We construct a confinement-dependent friction model which accounts for the additive friction contributions from bulk-like water, interfacial water layers and slip on arbitrary lengthscales.

Zusammenfassung

Der Einfluss von Wasser auf die Wechselwirkung und Reibung zwischen Oberflächen ist relevant in biologischen und technischen Systemen. Um diese quantitativ zu beschreiben, müssen auf molekularer Ebene alle relevanten Freiheitsgrade berücksichtigt werden. Ziel dieser Arbeit ist die Extraktion der Information auf atomarer Ebene aus Moleküldynamiksimulationen und deren Einbindung in Kontinuumsmodelle, die wir gegebenenfalls erweitern. Diese Arbeit behandelt die Wechselwirkung zwischen Oberflächen in Wasser, wobei stets das chemische Potential von Wasser kontrolliert werden muss.

Zunächst beschäftigt sich die Arbeit mit den dielektrischen Eigenschaften von Wasser zwischen polaren Kopfgruppen. Bei Abständen unter 1 nm ist die Komponente parallel zur Oberfläche etwas größer als in reinem Wasser, wogegen die senkrechte Komponente durch die anti-korrelierte Polarisierung benachbarter Wasser reduziert wird. Aus den dielektrischen Profilen berechnen wir ein Boxmodell, das sich zur effektiven elektrostatischen Modellierung eignet.

Im zweiten Teil befassen wir uns mit dem Ursprung der extrem starken Hydrationsrepulsion, die generell zwischen hydratisierten Oberflächen wirkt. Wir beschreiben die indirekten, durch Wasser vermittelten Kräfte mit einer Landau–Ginzburg Freien Energie und leiten die phänomenologischen Parameter aus Simulationsdaten ab. Ordnungsparameter, die auf der Polarisierung basieren, liefern quantitativ die korrekte Länge, auf welcher der indirekte Druck abfällt, erklären jedoch nur zehn Prozent des Drucks, was wir auf Effekte zurückführen, die sich nicht in der eindimensionalen Näherung beschreiben lassen. Andere Ordnungsparameter liefern einen viel kleineren Beitrag.

Das dritte Kapitel befasst sich mit Druck-Abstands-Kurven für neutrale und geladene Oberflächen, die durch Gegenionen neutralisiert werden. Bei Abständen über 0.5 nm und kleinen Ladungsdichten beschreibt das Poisson–Boltzmann–Modell die zusätzlichen Drücke. Für kleine Abstände dominiert die Repulsion zwischen Ionen und Oberfläche. Unsere Simulationen unter Berücksichtigung des chemischen Potentials von Wasser ermöglichen erstmals die Analyse solcher Effekte in explizitem Wasser.

Zuletzt betrachten wir die Scherkraft zwischen polaren Oberflächen im linearen Bereich bei kleinen Schergeschwindigkeiten, was typischen biologischen Situationen entspricht. Mit abnehmender Wasserschichtdicke treten drei Regimes auf: Die Viskosität von purem Wasser beschreibt große Abstände. Unterhalb eines Nanometers dominieren die hochviskosen Grenzschichten und erhöhen die Reibung. Beim Übergang zur trockenen Reibung kommt es zu Schlupf. Mit einem abstandsabhängigen Modell beschreiben wir die drei additiven Beiträge auf beliebigen Längenskalen.

Contents

1. Introduction

Water is an essential ingredient in biological cells and comprises more than a passive constituent of life in general [1]. It is also of major technical relevance, with rising significance concerning green technology [2]. The presence of water has a major influence on the interactions between solutes. For example, clays [3], surfactant films [4, 5] and uncharged lipid bilayers [6, 7], as well as biological membranes [8–11], swell in aqueous solutions. The molecular details in aqueous solutions determine the stability of colloidal suspensions [12]. Water as a solvent affects the structure of proteins [13] and conformational changes are supposed to be related to neurodegenerative diseases such as Alzheimer's or Parkinson's disease [14]. The resulting membrane–membrane separation is directly affected by the cell membrane composition and its interactions across the aqueous solvent, which not only regulates the physiological function but is also strongly correlated to dysfunctions such as the impaired neurotransmitter-triggered signal transduction appearing in age-related diseases [15]. The inter-membrane separation is further responsible for dermal function and dysfunction in skin cells [16], and also the internal cell organization relies on the well-defined membrane–membrane separation [17], just to name a few examples. Lubricated biological systems such as cartilage experience low friction due to the water layers that resist high normal loads [18]. The viscosity of nano-confined water determines the behavior of colloidal suspensions and is essential in industrial applications ranging from ceramics through cement and chocolate [19]. Thus a detailed understanding of surface–surface interactions in the aqueous environment is of utmost importance.

Often the description of biological matter and colloidal stability is separated into long-range and short-range forces [20]. For many systems, the force between charged surfaces interacting through a liquid medium is at large separations well described within the classical Derjaguin–Landau–Verwey–Overbeek (DLVO) theory [12, 21–23], which combines the van der Waals force and the electrostatic double layer repulsion, enabling a quantitative description of the aggregation of aqueous dispersions. However, on the lengthscale of the solvent molecules, which for water is on nanometer separations, the combination of van der Waals forces, that summarize the interactions between permanent and induced dipoles, and repulsive double layer forces, that occur between charged objects in aqueous solution, often fails to describe the interaction because of the emergence of other non-DLVO forces [24, 25]. Going beyond the pairwise additivity assumed in the van der Waals forces, McLachlan and Lifschitz in the 1950s generalized the work of Casimir, who studied the force between metal plates due to vacuum fluctuations [26–29]. The calculation of the resulting Hamaker constants [30] requires knowledge of the frequency-dependent dielectric permittivity functions of the aqueous and non-aqueous phase. The corresponding effective pair potential accounting also for retardation effects was algebraically derived by Podgornik et al. [31], however, at nanometer separations the resulting forces do not describe the experimental measures pressures between biological membranes.

For biological systems, also membrane undulations [32, 33] and protrusions of single lipid molecules have to be considered; but numerical studies have shown that their contributions on the relevant lengthscales is negligible [34, 35]. The overwhelmingly repulsive, or in the case of structured, rather hard surfaces, oscillatory forces have been summarized as solvation forces, or, more specifically, hydration forces. As discussed below, the mechanisms so far lack quantitative theoretical description, which is of central relevance in the present work. While theoretical models provide conceptual insight and scaling laws for the mechanisms proposed [36–42], they cannot predict the contribution of each mechanism on a quantitative level, since this depends on molecular details such as the conformational behavior and subtle differences in the interaction enthalpy of molecular groups, demanding rigorous modeling of all components including all relevant degrees of freedom.

Often the failure of continuum models like DLVO theory is attributed to the statement that these descriptions become invalid at scales corresponding to the molecular size. Although the statement is correct in many situations, it is typically based on the assumption that such models need to be described by homogeneous, bulk-like and local response functions. Consider, however, the dielectric response function of water, which we discuss in detail in Chapter 2: it is well established that the bulk water response function becomes non-local [43] and at interfaces it is non-isotropic [44]. Once the corresponding material parameters are obtained, e.g. from computer simulations, they quantitatively describe experimental data for which the common continuum approaches previously failed, if correctly employed in the theoretical description [45, 46]. In this work we study the effects of confined water on the interaction between planar surfaces, extract the molecular information from Molecular Dynamics (MD) simulations and extend the existing continuum models where necessary.

1.1. Hydration and solvation forces

Whenever liquid molecules are confined between two surfaces, they are induced to form quasi-discrete layers, giving rise to oscillatory solvation forces. These forces are related to the density oscillations which are mainly geometric in origin and are commonly observed for stiff surfaces both in water and non-aqueous solutions [47–49]. The hydration force denotes a special case in which a strong short-range repulsive force which is not captured within the DLVO forces acts between polar surfaces separated by a thin water layer of less than about 3 nm thickness [50, 51]. Pressure–distance measurements on phospholipid membranes, where the oscillatory contribution to the force is absent due to the soft, fluctuating nature of the lipid bilayers, showed that the hydration force obeys an approximately exponential decay with a characteristic length between 0.1 nm and 0.6 nm [52–55]. Later experiments revealed that the exponential decay applies to a much wider range of bio-materials [56]. The first account of the hydration force dates back to I. Langmuir in 1938 [57], yet its mechanism is still under debate and the description is basically empirical [58].

In Chapter 3 we discuss the repulsion due to the unfavorable overlap of ordering profiles of interfacial water layers which has been originally proposed by Marčelja and Radić [41]. We identify the indirect, water-mediated forces between hydrophilic surfaces with the contribution due to water ordering and obtain the free phenomenological parameter using Gaussian field theory, which allows to quantitatively predict the pressure from the corresponding water response function. The relevant order parameters follow from the water polarization, which we show by comparing with the pressures due to other order parameters that we find to be orders of magnitude smaller. This concludes the long-standing discussions on the appropriate choice of order parameters [20]. For the polarization-related order parameters we find quantitative agreement between polarization profiles and the decay lengths of the pressure for different surfaces.

1.2. Dielectric effects and electrostatic interactions

Most biologically or industrial relevant surfaces are charged in contact with water. Examples range from charged phospholipids in cell membranes [59–61] over monolayers of ionic surfactants [5] to solid surfaces such as glass, silica and mica [47, 49, 50, 52]. The description of the interaction between charged surfaces across aqueous electrolyte solutions is one of the fundamental problems in colloid science. Within the Derjaguin approximation [21] the conceptional work on (infinite) planar surface can be generalized to the interaction between curved surfaces, like e.g. colloidal suspensions.

Electrostatic interactions in aqueous solution are strongly influenced by water's dielectric properties. The large relative dielectric constant of bulk water of $\varepsilon_{\text{bulk}} = 80$ means that Coulomb interactions in water are reduced down to roughly 1 percent compared to vacuum. Stern's groundbreaking analysis of experimental surface capacitance data demonstrated that at a solid-water interface a thin interfacial layer exists with a dielectric constant much reduced compared to the bulk water value [62]. Although this interfacial layer has a thickness of only about a tenth of a nanometer, its effects on the surface capacitance as well as electrokinetic transport properties such as zeta potentials and surface conductivities are significant [63].

In Chapter 2 we investigate the two independent components of the dielectric response function, parallel and perpendicular to the surface. For a water slab thickness below 1 nm the dielectric response is highly asymmetric: while the parallel component slightly increases compared to bulk, the perpendicular one decreases drastically due to the anti-correlated polarization of neighboring water molecules. Within the work on this thesis the author has co-supervised a Master thesis and two Bachelor theses, in the work of which the dielectric permittivity profile has been obtained also for cylindrical nano-confinement, which is the relevant symmetry e.g. in carbon nanotubes or many protein channels (Ref. [xi], not discussed within this thesis). Solution of the anistropic Green's function then allows to compute electrostatic interactions using the dielectric profiles obtained from MD simulations both in planar and cylindrical symmetry, and to compute ion self-energies (Ref. [xi]).

The interaction between charged particles and surfaces across aqueous solution is commonly modeled by continuum theories and solvent-implicit simulations assuming constant dielectric properties in the water slab [64–67]. To obtain the explicit contribution of electrostatic interactions across an aqueous water slab, we study charged polar surfaces with neutralizing counterions immersed in the solvent in Chapter 4. The Hamiltonian for a system of N_{ion} counterions of valence q and two charged walls located at $z = -d/2$ and $z = d/2$ with a number charge density σ is in units of thermal energy $k_{\mathrm{B}}T$ given by

$$\frac{H}{k_{\mathrm{B}}T} = \sum_{j=1}^{N_{\mathrm{ion}}-1} \sum_{k=j+1}^{N_{\mathrm{ion}}} \frac{q^2 \ell_{\mathrm{B}}}{|\mathbf{r}_k - \mathbf{r}_k|} + 2\pi \ell_{\mathrm{B}} \sigma \sum_{j=1}^{N_{\mathrm{ion}}} (z_j + d/2) + 2\pi \ell_{\mathrm{B}} \sigma \sum_{j=1}^{N_{\mathrm{ion}}} (d/2 - z_j), \tag{1.1}$$

where $\ell_{\mathrm{B}} = e^2/4\pi\varepsilon\varepsilon_0 k_{\mathrm{B}}T$ is the Bjerrum length (e is the elementary charge, ε is the relative dielectric constant). The first term contains the Coulombic repulsion between the ions, the other two terms account for the electrostatic attraction to the wall (which is assumed to be infinite in lateral direction). Rescaling all lengths by the Gouy–Chapman length $\mu = 1/(2\pi q \ell_{\mathrm{B}} \sigma)$ according to $\tilde{r} = r/\mu$, the Hamiltonian Eq. (1.1) can be rewritten as

$$\frac{H}{k_{\mathrm{B}}T} = \sum_{j=1}^{N_{\mathrm{ion}}-1} \sum_{k=j+1}^{N_{\mathrm{ion}}} \frac{\Xi}{|\tilde{\mathbf{r}}_k - \tilde{\mathbf{r}}_k|} + \sum_{j=1}^{N_{\mathrm{ion}}} (\tilde{z}_j + \tilde{d}/2) + \sum_{j=1}^{N_{\mathrm{ion}}} (\tilde{d}/2 - \tilde{z}_j), \tag{1.2}$$

such that the Hamiltonian now depends only on the coupling parameter $\Xi = 2\pi q^3 \ell_{\mathrm{B}}^2 \sigma$. From Eq. (1.2) two limiting cases can be derived: for $\Xi \ll 1$, or at large separations $\Xi < \tilde{d}^2$, the ion interaction with the surface is dominant in this weak coupling limit and the mean-field approach, from which the Poisson–Boltzmann (PB) approach is derived, becomes valid (see e.g. Ref. [iii]). The interaction between the walls in this limit is repulsive (see Section 4.5.5) and has been analyzed first more than 100 years ago by Gouy and Chapman [68, 69]. In the opposite limit $\Xi \to \infty$ of strong coupling (SC) [70], the counterions essentially form a flat layer with mean lateral distance $\tilde{a} = \sqrt{\Xi}$ and the non-dimensonalized pressure

$$\tilde{\Pi} = \frac{\Pi}{2\pi \ell_{\mathrm{B}} \sigma^2 k_{\mathrm{B}} T} = \frac{2}{\tilde{d}} - 1 \tag{1.3}$$

is attractive at large separations [71]. In an intuitive picture, the first term of Eq. (1.3) can be interpreted as the entropic pressure due to an ideal gas of counter-ions and the second term as the electrostatic attraction between the charged surfaces and the counter-ions.

We show in Chapter 4 that if the hydration pressure Π_{hyd} is correctly accounted for, the mean-field approach is confirmed for low surface charge σ and monovalent ions $q = 1$ (such that $\Xi \ll 1$) also if the atomistic details are treated explicitly. The additivity of hydration and electrostatic interactions has been proposed to explain diffraction data of charged and uncharged lipids [72], however the precise value of the surface charge and its position is usually not known [73]. In the simulations we then vary the surface charge density σ such that the values $0.5 < \Xi < 6$ are in the intermediate coupling regime, where quantitative theoretical expressions are missing, but which is relevant for typical experimental and biological charge densities with monovalent counterions. We observe minima in the pressure–distance curves, which also in experiments is observed by coexisting phases [74, 75]. In Ref. [x], which is not discussed within this thesis, we investigated the solution of the non-linear Poisson–Boltzmann equation with additive and non-additive ion-specific surface potentials, where attraction or repulsion between the surfaces is observed depending on surface charge and potential [76].

1.3. Friction in aqueous confinement

The viscous properties of nanoscopically confined water are important when hydrated surfaces in close contact are sheared against each other [18, 19, 77]. Numerous experiments have probed the friction between atomically flat hydrated surfaces in the sub-nanometer separation regime [78–80] and suggested an increased water viscosity, but the precise value of the effective viscosity of ultra-confined water and the mechanism of hydration layer friction remains unclear [80–85]. A fundamental question that is difficult to address experimentally is how the friction between wet surfaces crosses over to the dry-friction limit, which is obtained for high loads when all water is squeezed out from between the surfaces. This limit, however, is of high relevance in bio-lubrication applications: For example, in joint lubrication, forces corresponding to the weight of a few grams are sufficient to squeeze the water completely out if the surface area is small enough. Hydrodynamic theory predicts the shear friction between surfaces that are separated by a fluid layer to diverge as the fluid film thickness goes to zero, but at the same time the friction forces between dry surfaces are expected to be finite.

To obtain a microscopic picture of water-mediated nanoscale friction at the border between hydrodynamic friction and dry friction, we perform extensive non-equilibrium molecular dynamics simulations in the linear-response regime at low shearing velocity, which is the relevant regime for typical biological applications, in Chapter 5. The experimental probe of this transition from wet to dry friction is challenging, because the high pressures needed to squeeze all water out cannot be easily generated with common techniques. With decreasing water film thickness we find three consecutive friction regimes: For thick films friction is governed by bulk water viscosity. At separations of about a nanometer the highly viscous interfacial water layers dominate and increase the surface friction, while at the transition to the dry friction limit interfacial slip sets in. Based on our simulation results, we construct a confinement-dependent friction model which accounts for the additive friction contributions from bulk-like water, interfacial water layers and interfacial slip and which is valid for arbitrary water film thickness. We use hydrodynamic equations, which reflect the conservation of momentum, a condition that arguably holds at any length scale, in conjunction with non-local linear-response theory, to define a spatially dependent effective viscosity profile without invoking any locality or continuum assumption. The main reason why the standard hydrodynamic description fails at the nanoscale, is not related to the discreteness of water molecules, but rather to the finite range of surface–fluid interactions, which we fix in terms of an effective viscosity profile.

1.4. Experimental measurements of the interaction pressure

In this section, we briefly review common experimental methods of obtaining the interaction between surfaces in aqueous solution and present the corresponding measurement ensemble. This will become important in the next section, where we discuss the computer simulations performed in this work, as also there the correct ensemble has to be taken into account.

In experiments, one way of obtaining the interaction between surfaces across solutions is the surface force apparatus (SFA) established by Israelachvili and co-workers. Here, the membranes are immobilized on two crossed cylinders of radius R and brought close together [86]. The distance d between the surfaces of both cylinders is determined by interferometry with Ångstrom precision. The force $F(d)$ acting between the cylinders is

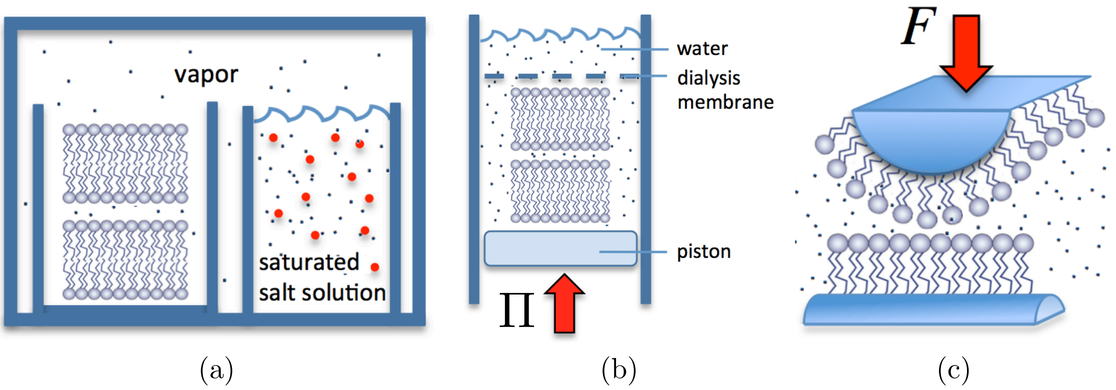

Figure 1.1.: **Schematics of the three methods for measuring the interaction pressure between lipid bilayers.** (a) In the osmotic stress method the lipid is in equilibrium with water vapor (or liquid) of known chemical potential μ at atmospheric pressure, (b) in the hydrostatic method the lipid is squeezed under pressure Π in a cell from which water can escape through a semipermeable membrane, and (c) in the SFA method the lipids are grafted on two crossed cylindrical surfaces and brought into contact under an externally controlled force F. Modified from Ref. [iii], with permission.

determined by the cantilever deflection. The interaction free energy per area, $\mathcal{F}/\mathcal{A}$, follows from the Derjaguin approximation [87],

$$\mathcal{F}(d)/\mathcal{A} = \frac{2\pi F(d)}{R}, \tag{1.4}$$

and the interaction pressure Π can be evaluated by differentiation. It is also common to measure pressure–distance curves of membrane multilayers by applying either hydrostatic or so-called equivalent pressures and measuring the lamellar periodicity L_z via neutron or X-ray diffraction [53]. These equivalent pressures are realized by shifting the chemical potential μ of the surrounding water according to the Gibbs–Duhem equation, $-S\mathrm{d}T + V\mathrm{d}\Pi = N\mathrm{d}\mu$. A shift $\Delta\mu$ at constant temperature then corresponds to an equivalent pressure $\Delta\Pi = \Delta\mu/v_{\mathrm{w}}^{\mathrm{b}}$, where $v_{\mathrm{w}}^{\mathrm{b}} = V/N_{\mathrm{w}}$ denotes the volume of a single water molecule in bulk. Equivalent pressures $\Pi < 100\,\mathrm{bar}$ are typically achieved by bringing the multilayers into osmotic contact with aqueous polymer solutions that compete for water through semi-permeable membranes. The equivalent pressure is then identical to the osmotic pressure exerted by the polymer solution. For higher equivalent pressures ($\Pi > 100\,\mathrm{bar}$), the multilayers are dehydrated via vapor exchange with a water reservoir of controlled chemical potential. Significant shifts $\Delta\mu$ can be realized by changing the temperature or the amount of salt in the water reservoir.

The membrane separation is usually quantified as the water layer thickness d_{w}, deduced from the measured lamellar periodicity L_z, either structurally from scattering length density profiles [88], or gravimetrically from the known volumes of lipids and water molecules (V_l and v_w) and from the number of water molecules per lipid $n_\mathrm{w} = N_\mathrm{w}/N_\mathrm{l}$ [6],

$$d_\mathrm{w} = L_z \frac{n_\mathrm{w} v_\mathrm{w}}{n_\mathrm{w} v_\mathrm{w} + V_\mathrm{l}}. \tag{1.5}$$

As in the presented experimental approaches the membranes are subject to different boundary conditions, the obtained pressure–distance curves are not completely equivalent. In an SFA experiment, the area per lipid remains approximately constant while varying the distance and exerting perpendicular mechanical force on membranes. In an equivalent-pressure experiment, membranes are free to rearrange their molecular organization upon dehydration. Finally, in an hydrostatic pressure experiment the isotropic pressure compresses membranes at constant water chemical potential. These distinct method differences must be kept in mind when analyzing experimental and simulation results, as we discuss next.

1.5. Molecular Dynamics modeling

Computer simulations can be used to numerically handle many-body problems such as the time evolution of complex biomolecular systems. In the very popular approach of Molecular Dynamics (MD), the system is composed of classical particles (e.g. atoms or molecules) and one integrates their Newton's equation of motion to sample conformations, calculate observables, etc. [89, 90].

In modeling biological system, water plays a very important role and different water models have been developed in the last several decades. We here use the Simple Point Charge / Extended (SPC/E) model [91], where a water molecule is represented by three interaction sites, corresponding to the three atoms of a water molecule. The two hydrogen sites possess positive electric charges, which are exactly balanced by the negative charge on the oxygen. These partial charges give rise to the water dipole moment and mimic the formation of hydrogen bonds. Additionally, the oxygen atoms in water molecules interact between each other via Lennard-Jones (LJ) interaction, accounting for both dispersion attraction and Pauli repulsion. Formally, the interaction between two water molecules a and b is defined as

$$W_{ab} = \sum_i^{\text{on } a} \sum_j^{\text{on } b} \frac{q_i q_j}{4\pi\varepsilon_0 r_{ij}} + \frac{C_{12}}{r_\mathrm{OO}^{12}} - \frac{C_6}{r_\mathrm{OO}^{6}}, \tag{1.6}$$

where the two sums run over all three sites in a molecule, q_i and q_j are partial charges, r_{ij}

the corresponding distance between the interacting sites, and C_{12} as well as C_6 the LJ coefficients that act between two oxygen atoms r_{OO} apart. Also other, more complex, water models have been developed, like TIP4P and TIP5P, which use four and five interaction sites, respectively. Computationally more demanding water models account also for its polarizability, which in principle can yield a more accurate description of water properties, but often doesn't.

In our MD simulations, we will analyze a model bilayer membrane consisting of Decanol ($CH_3(CH_2)_9OH$) molecules, for which force-field parameters are based on GROMOS53A6 [92]. This set of parameters is basically optimized to reproduce experimental solvation energies of alkanes. In another set of simulations we focus on experimentally well-studied bilayers consisting of dipalmitoyl-phosphatidyl-choline (DPPC). Like Decanol, they are represented via bonded, point-electrostatic, and LJ interactions. We use the united-atom Berger force field for DPPC, which defines effective interactions between lipids and water molecules. The parameters were determined by a combination of ab initio calculations and empirical optimization in such a way as to reproduce correct lipid densities from experiments [93], however we have recently shown that the surface interactions are quite robust with respect to the force field employed [94].

Simulations at controlled chemical potential

Simulations can be performed in various ensembles, which enables comparison with experimental data obtained under different boundary conditions. Typically the temperature T and the number of particles N are fixed in simulations. In addition, either the volume V (NVT ensemble) or the pressure Π ($N\Pi T$ ensemble) are kept constant. In the latter case, the constant pressure is maintained by continuous adjustments of the box size. However, as discussed above, experimental setups that investigate membrane interactions usually fix or control the water chemical potential. Explicit simulation of a water reservoir with bulk chemical potential is possible [95], but realizing realistic representations of interacting lipid membranes has been hampered by the exceedingly large associated numerical expenses [96]. There are, however, alternative approaches to account for the chemical potential of water, for example, through stochastic deletions and insertions of water molecules. Such a Grand Canonical Monte Carlo (GCMC) approach was established by Grunze, Pertsin, and co-workers [97] but so far only at moderate pressure resolution.

In this work we follow an alternative approach based on the Thermodynamic Extrapolation method [98]. To this end for the simulations in the $N_{\mathrm{w}}AL_zT$ ensemble, which we perform in analogy to SFA measurements at fixed lateral area A for different box heights L_z, we measure the chemical potential μ at different water numbers N_{w} with a precision as high as $0.01 k_{\mathrm{B}} T$ (Appendix A). The water number $N_{\mathrm{w}}(\mu_{\mathrm{b}})$ and interaction pressure $\Pi(\mu_{\mathrm{b}})$ are then extrapolated linearly, where μ_{b} denotes the chemical potential of bulk water and which is explained in detail in Appendix A. Similarly, for the simulations in the $N\Pi T$ ensemble we measure the chemical potential at ambient pressure Π_0 and determine the interaction pressure using a Gibbs–Duhem relation, see Appendix A.

2. Water dielectric effects in planar confinement

Bibliographic information: Parts of this chapter and of Appendix A have previously been published. Reprinted with permission from Ref. [i]. Copyright 2016 American Physical Society.

2.1. Introduction

The water structure at surfaces has a profound influence on wetting properties, adhesion between surfaces and adsorption of ions, molecular solutes and macromolecules [25, 36, 99, 100]. The understanding of hydration and hydrophobic interactions between surfaces has been possible by groundbreaking experimental techniques [52, 101, 102] and more recently been advanced by computer simulations that include explicit water [95, 98, 103–105].

Most biologically or technologically relevant surfaces such as lipid membranes [106], mineral surfaces and colloids [107] bear surface charges. Electrostatic interactions in aqueous solution are strongly influenced by water's dielectric properties. The large relative dielectric constant of bulk water of $\varepsilon_{\text{bulk}} = 80$ means that Coulomb interactions in water are reduced down to roughly 1 percent compared to vacuum. Stern's groundbreaking analysis of experimental surface capacitance data demonstrated that at a solid-water interface a thin interfacial layer exists with a dielectric constant much reduced compared to the bulk water value [62]. Although this interfacial layer has a thickness of only about a tenth of a nanometer, its effects on the surface capacitance as well as electrokinetic transport properties such as zeta potentials and surface conductivities are significant [63].

The interaction between charged particles and surfaces across aqueous solution is standardly modeled by continuum theories and solvent-implicit simulations assuming constant dielectric properties in the water slab [64–67]. Clearly, any modification of the water dielectric constant as the surfaces approach would strongly modify the electrostatic inter-surface interactions.

Whereas the bulk dielectric response of polar fluids is well understood [43, 108–110], atomistic simulations as well as analytic theories confirmed that it is strongly modified at interfaces [44, 111–113]. For a planar interface, the dielectric response becomes anisotropic and can be described by two local profiles $\varepsilon_{\|}(z)$ and $\varepsilon_{\perp}(z)$. The perpendicular component is particularly relevant and has been used to predict the surface zeta potential and capacitance in quantitative agreement with experimental data [45]. The effect of confinement on the dielectric constant, however, is highly relevant but far from settled [25]. Previous simulation studies suggested a reduced dielectric constant in confinement [114–117], however, some of these studies were debated because of ill-defined boundary conditions [118, 119].

In this chapter we extract the water dielectric properties between two soft polar model surfaces using extensive molecular dynamics (MD) simulations. Both parallel and perpendicular dielectric components reach the bulk value for water slab thickness larger than about 1 nm, for smaller thickness the parallel dielectric component is enhanced while the perpendicular component is drastically reduced. This symmetry breaking is solely due to collective polarization effects: The parallel polarization correlations between neighboring water molecules is slightly enhanced, while the perpendicular dipoles of neighboring water molecules are predominantly anti-correlated, leading to a negative collective contribution. We also show that the orientational freedom of polar headgroups adds significantly to the local dielectric constant. We cast our results in the form of a tensorial dielectric box model which can be straightforwardly implemented in future coarse-grained modeling of the interaction between charged surfaces and electrokinetic effects in confinement [120, 121].

2.2. Linear response theory

We write the change of the dielectric displacement field $\Delta\mathbf{D}(\mathbf{r})$ at position $\mathbf{r}$ due to the local change of the electric field $\Delta\mathbf{E}(\mathbf{r})$ as an integral over the non-local dielectric response tensor $\overleftrightarrow{\varepsilon}_{nl}$,

$$\Delta\mathbf{D}(\mathbf{r}) = \varepsilon_0 \int \overleftrightarrow{\varepsilon}_{nl}(\mathbf{r},\mathbf{r}') \cdot \Delta\mathbf{E}(\mathbf{r}')\mathrm{d}\mathbf{r}'. \tag{2.1}$$

For planar symmetry in the xy-directions, all fields and response functions only depend on the z-coordinate. Furthermore, the static Maxwell relation $\nabla \times \Delta\mathbf{E}(z) = 0$ shows that the parallel electric field $\Delta E_{||}$ is constant and thus Eq. (2.1) simplifies to

$$\Delta D_{||}(z) = \varepsilon_0 \varepsilon_{||}(z) \Delta E_{||}, \tag{2.2}$$

where we define the local parallel response as $\varepsilon_{||}(z) = \int \varepsilon_{nl}^{||}(z,z')\mathrm{d}z'$. Similarly, the Maxwell relation in the absence of free charges $\nabla \cdot \Delta\mathbf{D}(z) = 0$ shows that the perpendicular displacement field $\Delta D_{\perp}$ is constant which leads to the perpendicular local response relation

$$\Delta E_{\perp}(z) = \varepsilon_0^{-1} \varepsilon_{\perp}^{-1}(z) \Delta D_{\perp}. \tag{2.3}$$

We define parallel and perpendicular polarization correlation functions as

$$c_\alpha(z) = \langle m_\alpha(z) M_\alpha \rangle - \langle m_\alpha(z) \rangle \langle M_\alpha \rangle \,, \tag{2.4}$$

with $m_\alpha(z)$ being the laterally averaged polarization density at position z and $\alpha = \perp, \parallel$. The total polarization follows by an integral over the entire simulation box height, $M_\alpha = A \int_{-L_z/2}^{L_z/2} \mathrm{d}z\, m_\alpha(z)$, where the lateral simulation box area is $A = L_x L_y$.

Using the fluctuation-dissipation theorem, $\varepsilon_\parallel(z)$ is related to polarization correlations via [44, 111]

$$\varepsilon_\parallel(z) = 1 + \frac{c_\parallel(z)}{\varepsilon_0 k_\mathrm{B} T}, \tag{2.5}$$

where $k_\mathrm{B}T$ is the thermal energy and ε_0 denotes the vacuum permittivity. In contrast, the inverse perpendicular dielectric profile for a periodic system follows as [122]

$$\varepsilon_\perp^{-1}(z) = 1 - \frac{c_\perp(z)}{\varepsilon_0 k_\mathrm{B} T + C_\perp / V}, \tag{2.6}$$

where $V = A L_z$ is the simulation box volume and the variance of the total polarization is denoted as $C_\alpha = A \int_{-L_z/2}^{L_z/2} \mathrm{d}z\, c_\alpha(z)$. Note that for a homogeneous system we have $c_\perp(z) = C_\perp / V$ and thus $\varepsilon_\perp = 1 + c_\perp / \left(\varepsilon_0 k_\mathrm{B} T\right)$, in full analogy to the parallel component in Eq. (2.5) and Ref. [123]. However, in the general interfacial scenario, where $c_\perp(z)$ depends on the coordinate z, the parallel and perpendicular expressions Eqs. (2.5) and (2.6) are intrinsically different, as we will discuss in detail.

2.3. MD simulations

The slab between two planar surfaces consisting of 100 polar Decanol molecules each is filled with $N_\mathrm{w} = 170$ up to 19 752 SPC/E water molecules [91] (see Fig. 2.1 for a snapshot). The SPC/E model represents bulk water dielectric properties quite well [124]. Force-field parameters are based on GROMOS53A6 [92], Decanol hydroxyl groups are represented in atomistic detail, CH_2 and CH_3 groups as united atoms. The repulsion between headgroup oxygens is increased to reduce intra-surface hydrogen bonding [125]. To avoid slow reorientation events, we restrain all Decanols on the second CH_2 group counting from the OH headgroup with force constants $k_x = k_y = 500\,\mathrm{kJ/(mol\,nm^2)}$ and $k_z = 10\,\mathrm{kJ/(mol\,nm^2)}$ and the terminal CH_3 group with $k_x = k_y = 5\,\mathrm{kJ/(mol\,nm^2)}$ on a centered rectangular lattice with a lateral area per headgroup of $A/100 = 0.234\,\mathrm{nm}^2$. This corresponds to the tensionless state in vacuum with a Decanol tilt angle of 30°. Simulations

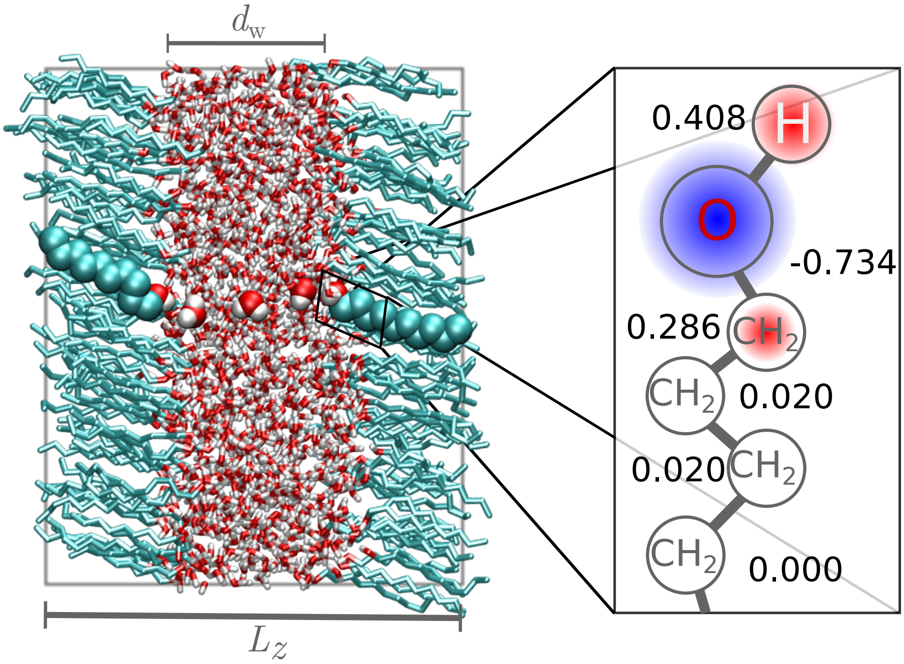

Figure 2.1.: **Simulation snapshot for a water layer thickness** $d_w = 1.5\,\text{nm}$. Selected molecules are shown using van-der-Waals spheres. Each monolayer consists of 100 Decanol molecules. The inset on the right shows the distribution of partial charges on the flexible polar headgroups.

are performed using version 5.0 of the GROMACS simulation package [126] at $T = 300\,\mathrm{K}$ with periodic boundary conditions and analyzed using the MDAnalysis package [127].

In analogy to experiments [53], we define the water layer thickness d_w using the bulk molecular water volume $v_\mathrm{w}^\mathrm{b} = 0.0304\,\mathrm{nm}^3$ and the number of water molecules N_w as $d_\mathrm{w} = N_\mathrm{w} v_\mathrm{w}^\mathrm{b}/A$. For small separations $d_\mathrm{w} < 3\,\mathrm{nm}$, simulations are done in the $N_\mathrm{w} A L_z T$ ensemble at constant volume $V = AL_z$ and the number of water molecules N_w is adjusted via thermodynamic extrapolation to yield a constant chemical potential [98], see Section 2.6.1 and Appendix A. For $d_\mathrm{w} > 3\,\mathrm{nm}$, the interaction pressure is negligible and we use the $N_\mathrm{w} A \Pi_0 T$ ensemble at fixed vertical pressure $\Pi_0 = 1\,\mathrm{bar}$. Lennard Jones interactions are truncated at $r_\mathrm{c} = 0.9\,\mathrm{nm}$, for the electrostatic interactions the Particle Mesh Ewald method [128] is employed with a real-space cut-off $r_\mathrm{c} = 0.9\,\mathrm{nm}$. Simulations for $d_\mathrm{w} < 8\,\mathrm{nm}$ have a length of $1\,\mu\mathrm{s}$, trajectories at larger separations are obtained for at least 100 ns.

2.4. Dielectric profiles

We analyze the water and Decanol polarization contributions separately according to

$$m_\alpha(z) = m_\alpha^\mathrm{w}(z) + m_\alpha^{dec}(z). \tag{2.7}$$

The perpendicular polarization profile is calculated via integration of the charge density $\rho(z)$ according to $m_\perp(z) = -\int_{-L_z/2}^{z} \rho(z')\mathrm{d}z'$, the parallel polarization profile is calculated from the boundary polarization charge distribution [129], see Section 2.7 for details. Figure 2.2 (a) shows the water, Decanol and the total mass density profiles $\rho_\mathrm{m}(z)$ for $d_\mathrm{w} = 1.5\,\mathrm{nm}$ and demonstrates that water density oscillations (blue line) are absent as expected for our relatively soft surfaces [125, 130, 131]. The total mass density (black line) is rather uniform throughout the system. The vertical gray lines denote the Gibbs dividing surface positions, z_GDS, which thermodynamically define the surface positions and follow from our definition of the water slab thickness as $z_\mathrm{GDS} = \pm d_\mathrm{w}/2$. The charge density profile in Fig. 2.2 (b) reveals that the main contribution comes from the Decanols (red line) which is due to the pronounced orientation of the headgroups with respect to the surface normal.

The parallel dielectric data in Fig. 2.2 (c) demonstrate that the headgroups (red line) significantly contribute and produce a maximum in the total dielectric profile (black line) of $\varepsilon_\parallel = 75$ close to the interface position, slightly larger than the bulk value $\varepsilon_\mathrm{bulk} = 70.0 \pm 0.2$ (denoted by a horizontal broken line, determined independently from bulk simulations and consistent with literature values for SPC/E water [124, 132]).

In Figure 2.2 (d) we show $1 - \varepsilon_\perp^{-1}(z)$ which according to Eq. (2.6) is proportional to the perpendicular polarization correlations $c_\perp(z)$ and thus can be decomposed into the

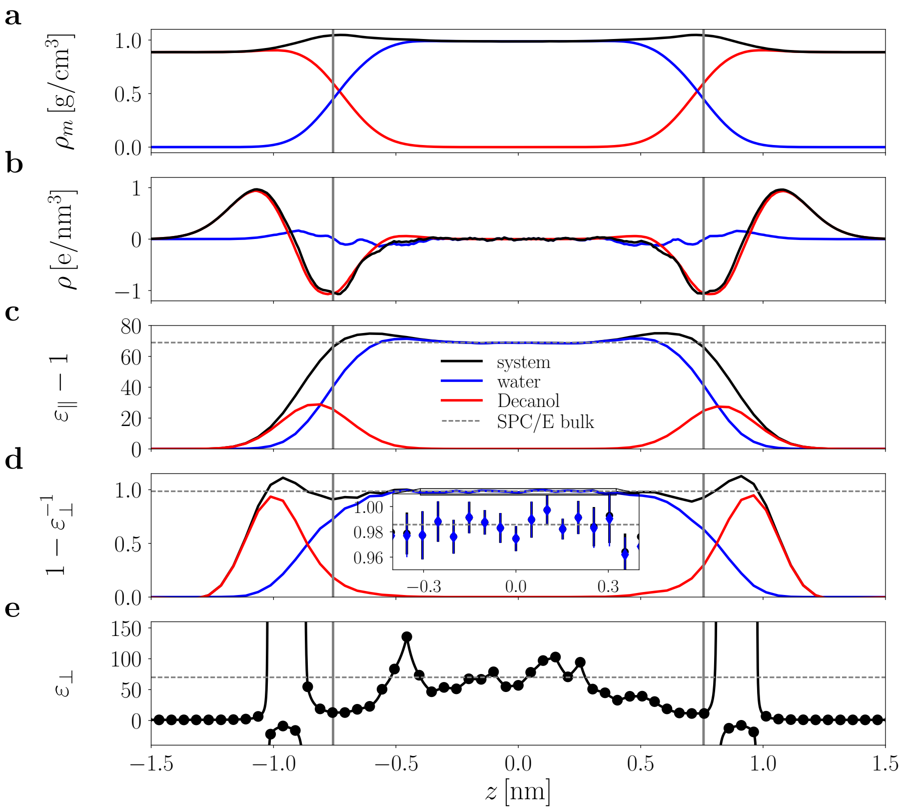

Figure 2.2.: **MD results for a water slab thickness $d_\mathrm{w} = 1.5\,\mathrm{nm}$.** Profiles for (a) mass density, (b) charge density, (c) parallel dielectric response, (d) inverse perpendicular dielectric response and (e) perpendicular dielectric response are shown, contributions of water and Decanol are indicated by blue and red lines, respectively. The horizontal broken lines denote the bulk value of SPC/E water. The inset in (d) zooms into the slab central region where bulk water behavior is obtained. The vertical gray lines indicate the Gibbs dividing surface positions.

water and Decanol contributions. We see that headgroups (red line) contribute even more than in the parallel direction and that $1-\varepsilon_\perp^{-1}(z)>1$ inside the headgroup region. This means that the perpendicular dielectric profile $\varepsilon_\perp(z)$, shown in Fig. 2.2 (e), exhibit poles close to the surface and is negative in a finite region. We will further below see that these divergencies are unproblematic for coarse-grained modeling applications. The inset in Fig. 2.2 (d) demonstrates that $1-\varepsilon_\perp^{-1}(z)$ in the slab center approaches the expected bulk value $1-1/70=0.986$ with high precision. Not surprisingly, the data for $\varepsilon_\perp(z)$ in Fig. 2.2 (e) show significant numerical noise (error bars larger than figure height) but are consistent with the expected bulk value $\varepsilon_{\mathrm{bulk}}=70$ (denoted by a horizontal broken line) in the slab middle. As this shows, the inverse relation between $c_\perp(z)$ and $\varepsilon_\perp(z)$ in Eq. (2.6) makes the estimation of the perpendicular dielectric profile in thin slabs numerically highly demanding.

2.4.1. Self and collective polarizations

Using that the total polarization can be written as $M_\alpha=\sum_i p_{i,\alpha}$, where p_i is the dipole moment of molecule i, we split the polarization variance $C_\alpha=C_\alpha^{\mathrm{self}}+C_\alpha^{\mathrm{coll}}$ into self and collective contributions defined as

$$C_\alpha^{\mathrm{self}}=\sum_i\left\langle p_{i,\alpha}^2\right\rangle-\left\langle p_{i,\alpha}\right\rangle^2 \qquad \text{and} \tag{2.8}$$

$$C_\alpha^{\mathrm{coll}}=\sum_i\sum_{j\neq i}\left\langle p_{i,\alpha}p_{j,\alpha}\right\rangle-\left\langle p_{i,\alpha}\right\rangle\left\langle p_{j,\alpha}\right\rangle. \tag{2.9}$$

The parallel total variance $C_\parallel/(Ad_{\mathrm{w}}\varepsilon_0k_{\mathrm{B}}T)$ in Fig. 2.3 approaches the bulk value $\varepsilon_{\mathrm{bulk}}-1=69$ (solid line) already for $d_{\mathrm{w}}>2\,\mathrm{nm}$, i.e., the parallel polarization fluctuations exhibit bulk-like behavior even in thin slabs. In contrast, the perpendicular variance is far from the bulk limit, and based on Eq. (2.6) is expected to approach the limit $C_\perp/(Ad_{\mathrm{w}}\varepsilon_0k_{\mathrm{B}}T)=69$ only at separations larger than hundreds of nanometers, reflecting that electrostatic boundary effects have long-range consequences.

Interestingly, both self contributions, $C_\parallel^{\mathrm{self}}$ and $C_\perp^{\mathrm{self}}$ approach the value for an isolated water molecule in the Langevin model $\varepsilon_{\mathrm{bulk}}^{\mathrm{self}}-1=19$ for $d_{\mathrm{w}}\gtrsim 1\,\mathrm{nm}$, see Section 2.8. This shows that the single water response is weakly perturbed by correlation effects both in parallel and perpendicular directions. In fact, the slow crossover of $C_\perp$ is entirely due to the collective contribution $C_\perp^{\mathrm{coll}}$, which turns out to be negative for all separations considered by us (red open diamonds in Fig. 2.3). This means that the perpendicular water polarizations of neighboring water molecules are anti-correlated.

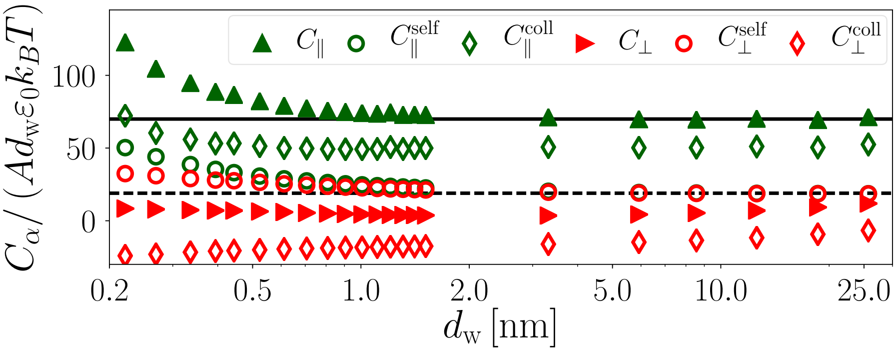

Figure 2.3.: **Self and collective contributions to the polarization variances.** Total (solid triangles) as well as self (open circles) and collective (open diamonds) polarization variances as a function of water slab thickness d_w. The solid horizontal line represents the expected bulk limit $C_\alpha/(Ad_\mathrm{w}\varepsilon_0 k_\mathrm{B}T) = 70 - 1 = 69$, the dashed horizontal line shows the Langevin model prediction for an isolated water molecule $C_\alpha^\mathrm{self}/(Ad_\mathrm{w}\varepsilon_0 k_\mathrm{B}T) = 19$.

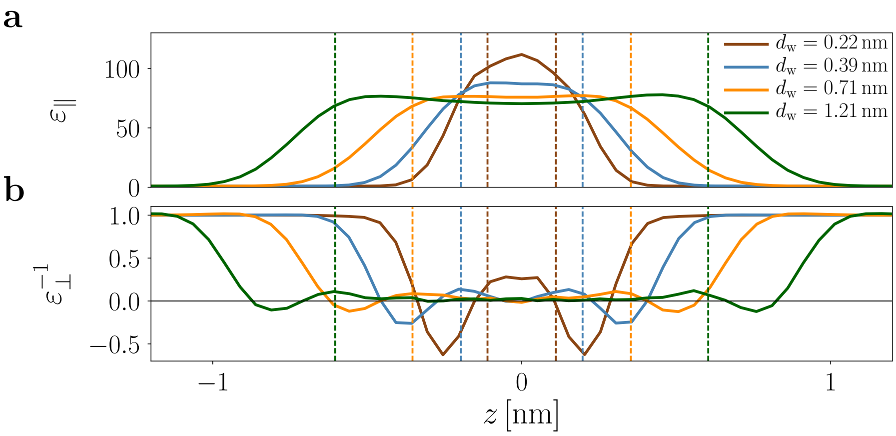

Figure 2.4.: **Dielectric profiles at various water slab thicknesses** (a) Parallel and (b) inverse perpendicular dielectric profiles. The vertical broken lines indicate the corresponding water slab thickness d_w.

2.4.2. Dielectric box model

Figure 2.4 shows the parallel and inverse perpendicular dielectric profiles for a few different separations. At the smallest separations, $\varepsilon_{\|}(z)$ is enhanced in the slab center while $\varepsilon_{\perp}^{-1}(z)$ is negative over an extended range. To cast these features into a description suitable for coarse-grained modeling and analytical approaches, we derive a simple dielectric box model based on effective medium theory concepts [133].

Since in the parallel direction $\Delta E_{\|}$ is constant, we demand that an effective dielectric box model reproduces the integral over the parallel displacement field, $\int_{-L_z/2}^{L_z/2} \mathrm{d}z\, \Delta D_{\|}(z)$. Assuming an effective dielectric constant $\varepsilon_{\|}^{\mathrm{eff}}$ in a box of width d^{eff}, Eq. (2.2) leads to

$$d_{\|}^{\mathrm{eff}} \left(\varepsilon_{\|}^{\mathrm{eff}} - 1\right) + L_z = \int_{-L_z/2}^{L_z/2} \varepsilon_{\|}(z) \mathrm{d}z. \tag{2.10}$$

In the perpendicular direction $\Delta D_{\perp}$ is constant, thus we demand the effective box model to reproduce the integral over the electric field, $\int_{-L_z/2}^{L_z/2} \mathrm{d}z\, \Delta E_{\perp}(z)$, which is nothing but the electrostatic potential difference at the system boundaries. Using Eq. (2.3), we obtain

$$\int_{-L_z/2}^{L_z/2} \mathrm{d}z\, \varepsilon_{\perp}^{-1}(z) = d_{\perp}^{\mathrm{eff}} \left(\frac{1}{\varepsilon_{\perp}^{\mathrm{eff}}} - 1\right) + L_z. \tag{2.11}$$

Obviously, Eqs. (2.10) and (2.11) depend on two unknowns each, the box width $d_{\alpha}^{\mathrm{eff}}$ and the effective dielectric constant $\varepsilon_{\alpha}^{\mathrm{eff}}$. In Figure 2.5 (a) we show $d_{\alpha}^{\mathrm{eff}} - d_{\mathrm{w}}$ as a function of the water slab thickness d_{w} when assuming $\varepsilon_{\alpha}^{\mathrm{eff}} = \varepsilon_{\mathrm{bulk}}$. For both components we observe $d_{\alpha}^{\mathrm{eff}} - d_{\mathrm{w}} > 0$, meaning that water slabs at polar surfaces possess a dielectric interfacial excess that we associate with contributions from polar orientable headgroups. For the parallel component, the effective box width increases at small separations, indicating that confined water becomes a more efficient parallel dielectric. In contrast, $L_{\perp}^{\mathrm{eff}}$ decreases for small d_{w}, thus the perpendicular dielectric efficiency of confined water decreases. The shifts $d_{\alpha}^{\mathrm{eff}} - d_{\mathrm{w}}$ saturate for large d_{w} at $d_{\|}^{\mathrm{eff}} - d_{\mathrm{w}} \equiv \delta_{\|} = 0.4\,\mathrm{nm}$ and $L_{\perp}^{\mathrm{eff}} - d_{\mathrm{w}} \equiv \delta_{\perp} = 0.7\,\mathrm{nm}$, indicated by dashed lines in Fig. 2.5 (a). Using now for the effective box widths the asymptotic results for large surface separation $d_{\alpha}^{\mathrm{eff}} = d_{\mathrm{w}} + \delta_{\alpha}$, Fig. 2.5 (b) shows the resulting effective dielectric constants. $\varepsilon_{\|}^{\mathrm{eff}}$ increases for small separations and reaches a value of about $\varepsilon_{\|}^{\mathrm{eff}} = 85$ at the smallest separation. In contrast, $\varepsilon_{\perp}^{\mathrm{eff}}$ drastically decreases for $d_{\mathrm{w}} < 1\,\mathrm{nm}$ and saturates at about $\varepsilon_{\perp}^{\mathrm{eff}} = 10$ at the smallest separation. We thus predict that electrostatic interactions between surfaces, which are described by the perpendicular dielectric component, will be strongly enhanced at small separations.

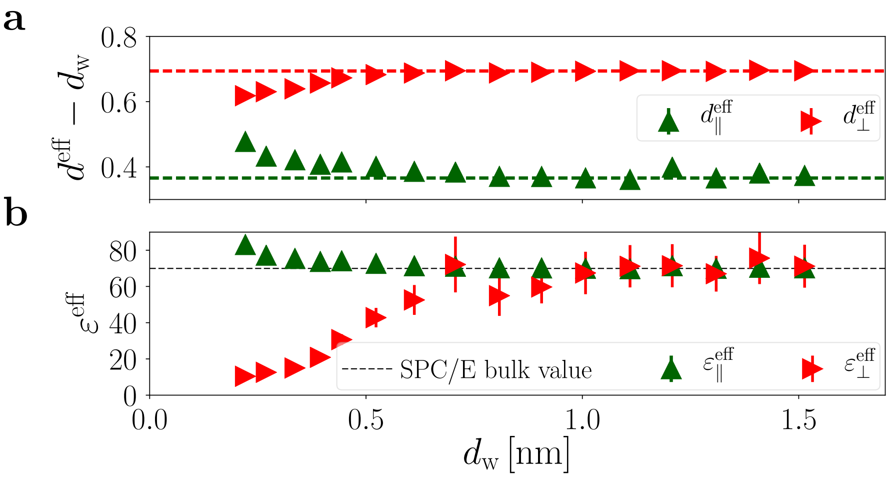

Figure 2.5.: **Dielectric shifts and effective dielectric constant for a box model.** (a) Shifts of the effective dielectric box widths $d_{\alpha}^{\mathrm{eff}} - d_{\mathrm{w}}$ assuming effective dielectric constants corresponding to the bulk value as defined by Eqs. (2.10) and (2.11). The horizontal dashed lines denote the asymptotic shifts $\delta_{\alpha} = d_{\alpha}^{\mathrm{eff}} - d_{\mathrm{w}}$ for large separation. (b) Effective dielectric constants $\varepsilon_{\alpha}^{\mathrm{eff}}$ when assuming effective box widths given by $d_{\alpha}^{\mathrm{eff}} = d_{\mathrm{w}} + \delta_{\alpha}$.

2.5. Conclusion

While we expect details of the dielectric profiles to depend on the surface stiffness and the specific surface chemistry, preliminary simulation results for different surface types suggest the decrease of the perpendicular dielectric component for small separations to be a rather universal feature. Since sub-nanometer water layers are typical for strongly compressed surfaces in technological and biological applications, our results have consequences for a number of applications. In particular, we suggest that part of the deviations of experimentally measured interactions between charged surfaces from standard Poisson-Boltzmann predictions, that are typically ascribed to hydration interactions [73], might in fact be due to a decreasing perpendicular dielectric constant at strong confinement.

2.6. Supplemental material

2.6.1. Simulations at prescribed chemical potential

For small separations $d_\mathrm{w} < 3\,\mathrm{nm}$, we adjust the number of water molecules in the $N_\mathrm{w}AL_zT$ ensemble, such that the water chemical potential equals the bulk value. The water chemical potential and the resulting interaction pressure are therefore state functions of the independent quantities, $\Pi(N_\mathrm{w}, A, L_z, T)$ and $\mu(N_\mathrm{w}, A, L_z, T)$. The simulation pressure can be measured directly in MD simulations, however precisely measuring the chemical potential is challenging and discussed in detail in Appendix A.

2.6.2. Interaction pressure between the polar Decanol surfaces

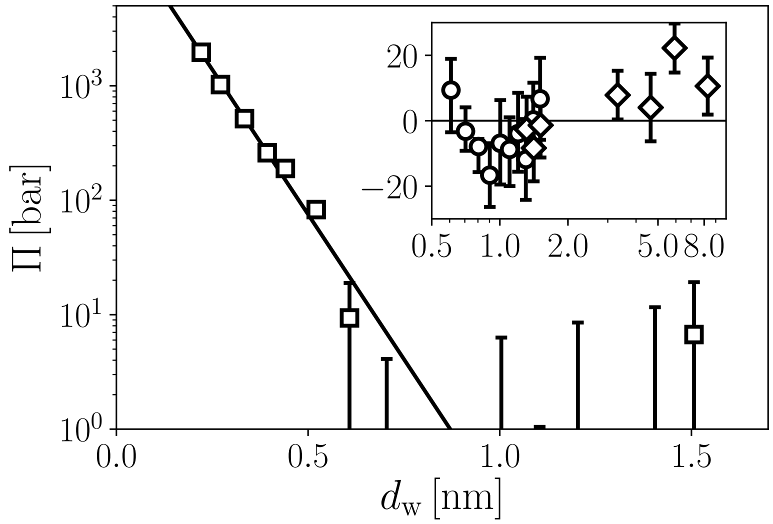

Figure 2.6.: **Interaction pressure between Decanol surfaces across water.** Simulation data was obtained using thermodynamic extrapolation via N_w adjustment (Eq. (A.12), squares) as well as via volume adjustment at larger separations (Eq. (A.17), diamonds). The solid line denotes an exponential fit to the logarithmic data. In the inset the data at larger separations is shown.

Soft hydrophilic surfaces, as used in our study, typically exhibit an exponentially decaying repulsive interaction across water [51, 53, 54, 86]. The hydration repulsion universally acts between sufficiently polar hydrated surfaces with a characteristic decay length of a fraction of a nanometer [47, 53, 86]. Figure 2.6 shows the interaction pressure for our simulation system as described in the main text, yielding a characteristic length of $\lambda = 0.86\,$Å(represented by the solid line in Fig. 2.6).

Figure 2.6 shows data for the $N_\mathrm{w}AL_zT$ simulations used in the main text, where the number of waters N_w is adjusted such that $\mu \approx \mu_0$ (full squares). At separations $d_\mathrm{w} > 3\,\mathrm{nm}$, the interaction pressure is zero within our measurement resolution of about 10 bars, which we confirm by thermodynamic extrapolation via L_z-adjustment in the $N_\mathrm{w}A\Pi T$ ensemble (diamonds in Fig. 2.6)), where the pressure in normal direction is set to $\Pi_0 = 1\,\mathrm{bar}$ using semi-isotropic Berendsen pressure coupling [134].

2.7. Calculation of the parallel polarization density

To calculate the parallel polarization density, we introduce a virtual cut perpendicular to the x-axis at an arbitrary position inside the simulation box. This cut splits some water molecules as shown in Fig. 2.7, creating virtual charge densities $\pm\mathcal{P}_0(x,z)$ on both sides of the cut, which corresponds to a surface charge density σ. In the y-direction, the system is spatially invariant. Note that the cut leaves intact molecules that cross the periodic boundaries of the simulation system, i.e., the virtual surface charge density is nonzero only at the position of the cut.

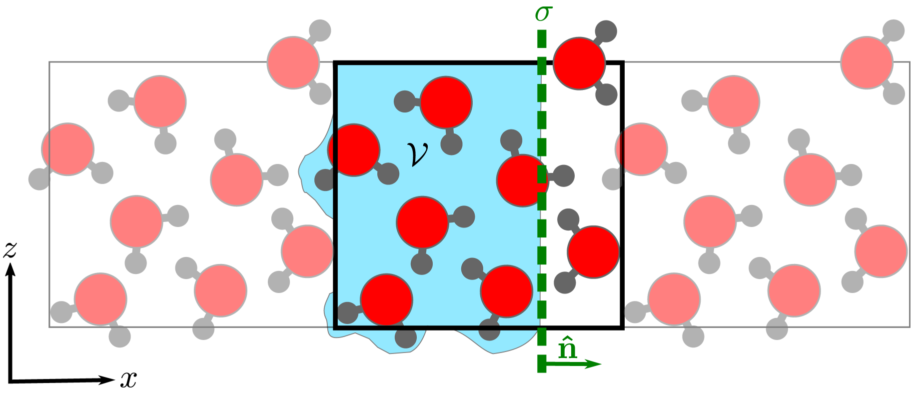

Figure 2.7.: **Schematic illustration of the calculation of the parallel polarization density.** The volume $\mathcal{V}$ used for calculating the parallel polarization density in Eq. (2.13) is shown in blue. On the left boundary, the volume has been chosen such that water molecules are not split across the periodic boundary, whereas on the right boundary molecules are cut. The central simulation box is denoted by a black rectangle.

The integral over the volume $\mathcal{V}$ (blue shaded region in Fig. 2.7), equals the projection of the polarization density onto the surface normal $\hat{\mathbf{n}}$ of the cut,

$$\int \mathcal{P}_0(x,z)\mathrm{d}x = -\mathbf{m}(z)\cdot\hat{\mathbf{n}}. \tag{2.12}$$

Since the virtual cut is perpendicular to the x-axis, it follows that $\mathbf{m}(z)\cdot\hat{\mathbf{n}} = \pm m_x(z)$ and with Eq. (2.12), we find

$$m_x(z) = \mp \int \mathcal{P}_0(x, z)\,\mathrm{d}x, \tag{2.13}$$

where the different signs refer to the two possible directions of the surface normal, thus integrating $\mathcal{P}_0(x, z)$ over the volume $\mathcal{V}$ on the different sides of the cut. To obtain $m_y(z)$ the same procedure is applied.

2.8. Langevin model for the water dipole

We consider water as an ideal dipole in an external field. Then the interaction energy of a single dipole $\mathbf{P}$ in an electric field $\mathbf{E}$ is given as

$$W = -\mathbf{P} \cdot \mathbf{E} = -PE\cos(\vartheta). \tag{2.14}$$

For a freely rotating dipole the probability distribution is given by the Boltzmann factor,

$$\exp\left(-\frac{W}{k_\mathrm{B}T}\right) = \exp\left(\frac{PE\cos\vartheta}{k_\mathrm{B}T}\right), \tag{2.15}$$

which for a constant electric field in z-direction yields

$$\begin{aligned} \langle P_z \rangle = P\,\langle \cos\vartheta \rangle &= P\,\frac{\int_0^\pi \cos\vartheta\ \mathrm{e}^{PE\cos\vartheta/k_\mathrm{B}T}\sin\vartheta\ \mathrm{d}\vartheta}{\int_0^\pi \mathrm{e}^{PE\cos\vartheta/k_\mathrm{B}T}\sin\vartheta\ \mathrm{d}\vartheta} \\ &= P\left[\coth\left(\frac{PE}{k_\mathrm{B}T}\right) - \frac{k_\mathrm{B}T}{PE}\right] =: PL(P,T), \end{aligned} \tag{2.16}$$

where we have defined the temperature-dependent Langevin function L. Expansion up to the third order yields

$$L(x) = \coth(x) - \frac{1}{x} \ = \frac{x}{3} - \frac{x^3}{45} + \mathcal{O}(x^5), \tag{2.17}$$

where we used the abbreviation $x = PE/k_\mathrm{B}T$. For the dipole moment of the SPC/E water model, $P_0 = 2.35\,\mathrm{D} = 0.49\,\mathrm{e}\text{Å}$, and assuming only moderate field strengths of about $E = 10^7\,\mathrm{V/m}$, at 300 K the expansion is perfectly valid as $x \approx 0.019$.

For linear dielectric response the polarization per volume $\mathbf{m} = \langle \mathbf{P} \rangle / v$ is proportional to the applied field,

$$\mathbf{m} = \varepsilon_0\,(\varepsilon - 1)\,\mathbf{E}. \tag{2.18}$$

Combining Eqs. (2.16) (2.17) and (2.18) we obtain for the SPC/E water model

$$\varepsilon = 1 + \frac{P^2}{3v_{\mathrm{w}}^{\mathrm{b}}\varepsilon_0 kT} = 19.65, \tag{2.19}$$

with $v_{\mathrm{w}}^{\mathrm{b}} = V/N = 0.0304\,\mathrm{nm}^3$ being the bulk volume of a single water molecule.

3. Landau–Ginzburg theory for membrane–membrane interactions

Bibliographic information: The content of this chapter is in preparation to be submitted to a peer-reviewed journal (Ref. [iv]) and builds upon prior research that was conducted within this thesis (Refs. [ii] and [iii]).

3.1. Introduction

The hydration force denotes a strong short-range repulsive force that acts between polar surfaces separated by a thin water layer (< 3 nm). Its first account goes back to I. Langmuir in 1938 [57] and it also applies to some other polar solvents [135–137]. The hydration force determines the behavior of many industrial and biological systems, such as the stability of colloidal dispersions [75] and soap films [4, 138], the swelling of clays [139], and the interactions of biological membranes [34] and macromolecules [56]. Pressure–distance measurements in the late 1970s and '80s on phospholipid membranes, which constitute a typical model for biomembranes, showed that the hydration repulsion obeys an approximately exponential decay with a characteristic length between 0.1 nm and 0.6 nm [52–55].

Later studies on phospholipid membranes [140–143] revealed that the decay lengths agree with a wide class of interacting macromolecular systems in aqueous solution such as DNA double helices, stiff polysaccharides, and proteins [56], however the repulsion mechanisms still elude quantitative theoretical description [58]. Three fundamentally different mechanisms have been proposed: (i) repulsion due to the enforced release of water molecules that are strongly bound to the membrane surface [36, 37], (ii) repulsion due to the reduction in configurational entropy of membrane lipids [38, 39] and (iii) repulsion due to the unfavorable overlap of ordering profiles of interfacial water layers [41].

A first attempt to rationalize the hydration repulsion based on water structuring characterized in terms of suitably defined order parameter profiles has been proposed by Marčelja and Radić in the 1970s [41]. The basic concept was further refined [42] and frequently discussed in terms of the water molecules' dipole orientation and its non-local dielectric response function [144–146]. Whereas the theoretical models provide conceptual insight and scaling laws for the proposed mechanisms, they are not analyzed quantitatively because of the dependence on molecular details and the presence of unknown parameters. Moreover, the interactions based on water ordering in a Marčelja–Radić model consider the solvent contribution to the interaction only, which experimentally is not accessible due to the presence of direct membrane–membrane interactions and hence necessitates simulations. For a quantitative description of the hydration repulsion between membranes thus a rigorous atomistic modeling of all relevant degrees of freedom is necessary, which is continuously improved since the early days of lipid molecular dynamics (MD) simulations [147, 148]. Only recently we have developed a method to perform such simulations at controlled water chemical potential μ [98], which is the experimentally relevant ensemble, and which allows to quantitatively compare interaction pressures between MD simulations and experiments [94, 149].

By performing simulations at bulk water chemical potential μ_b we study a model system of Decanol ($CH_3(CH_2)_9OH$) bilayers and the experimentally well studied system of Dipalmitoylphosphatidylcholine (DPPC) bilayers in the ordered L_β and disordered L_α state. In this setup, the simulation pressure is entirely due to the interaction between the surfaces and the water, thus different order parameters can be evaluated explicitly [105] and be compared with the indirect, water-mediated interaction pressures. To this end we first review the Marčelja–Radić result including a surface field [42], which is the relevant boundary condition for repulsion [105]. We then obtain the free parameters for predicting the interaction pressures from an analysis of the order parameter profiles and their fluctuations. The Marčelja–Radić model has been criticized amongst others by Ninham [20], since the order parameter is often associated with polarization, whereas it could also be, e.g. , the water tetrahedrality accounting for the hydrogen bond network. Of all possible order parameters some yield attractive, some repulsive pressures. In Section 3.5.7 we exemplarily analyze the repulsive pressure due to the antisymmetric octupole orientation profile and the attractive pressure due to the symmetric quadrupole orientation profile and find both to be negligible compared to the pressures from the polarization profiles.

Our observations reveal that a single order parameter cannot explain the repulsion alone; for all considered order parameters the profiles agree with the prediction of the Marčelja–Radić model. Choosing the polarization as order parameter, the remaining free parameter in the Landau–Ginzburg model, which is the amplitude of the repulsive pressures, in bulk is related to the dielectric permittivity. The water polarization density profiles $m_\perp$ projected onto the membrane normal and the polarization contributions in a multipole expansion predict the correct decay length of the water-mediated repulsion and yield significant pressures which are not additive. The total indirect pressures are about ten times larger than expected from the contributions in the Landau–Ginzburg model. However, the shape of the indirect pressures is well described by the Landau–Ginzburg theory; we conclude that this difference might arise due to the fact that in a one-dimensional mean-field analysis the lateral correlations are neglected as well as the discrete nature of the surface [150, 151].

Moreover, the surface polarity profile (which here enters via a delta-shaped surface field) contributes significantly to the resulting pressure [152].

3.2. Landau–Ginzburg free energy

In their pioneering work, Marčelja and Radić predicted for separations that are larger than the order parameter correlation length an exponential decay of the hydration repulsion based on a continuum order-parameter accounting for the structural properties of water confined between the membrane surfaces. The solvent perturbation due to the lipid head groups is described within a general scalar mean-field theory and the water structure is expressed in terms of a spatially-dependent order parameter; the effects of the membranes enter via surface boundary conditions. In this work we focus on the perpendicular polarization density $m_\perp$ and its contributions in a multipole expansion as order parameters. Due to rotational symmetry around the membrane normal and translational invariance in the direction parallel to the membrane, the perpendicular component is the only non-vanishing contribution of the polarization in a one-dimensional mean-field model.

We expand the free energy of the water slab in terms of the scalar order parameter according to Landau theory [22]. Considering only the lowest-order terms [41] and including the surface effects via surface fields $h_\pm$ that couple linearly to the order parameter $m_\perp$ at the interfaces located at $z = d/2$ and $z = -d/2$, the free energy $\mathcal{F}$ per area A and reduced temperature $\beta = 1/k_\mathrm{B}T$, as was first introduced by Cevc et al. [42], can be written as

$$\frac{\beta\mathcal{F}\left[\eta(\cdot)\right]}{A} = \int_{-d/2}^{d/2} \left[a m_\perp^2(z) + b\left(\nabla m_\perp(z)\right)^2\right] \mathrm{d}z + \, h_+ m_\perp(d/2) \, + \, h_- m_\perp(-d/2). \quad (3.1)$$

Here, a and b are positive phenomenological parameters, which measure the stiffness of the order parameter and the spatial range of interactions, respectively. In Section 3.5.4 we show that Eq. (3.1) is obtained from a general expansion of the free energy density including a term that couples quadratically to the surface field. Podgornik and Žekš [153] showed that the expression of a constant surface field as proposed by Cevc et al. [42], corresponding to Eq. (3.1), can then be obtained as limiting case when the stiffness of the surface coupling dominates over the water stiffness a

The order parameter profiles can be derived from Eq. (3.1) by variational minimization, yielding

$$am_\perp(z) - b\nabla^2 m_\perp(z) = 0, \tag{3.2}$$

$$h_+ + 2b\nabla m_\perp(d/2) = 0, \tag{3.3}$$

$$h_- - 2b\nabla m_\perp(-d/2) = 0. \tag{3.4}$$

Near the membrane surface, water molecules have a preferred orientation due to interactions with the membrane head groups [154]. In this case the order parameter profile is an odd function with respect to the symmetry plane in the middle of the water slab at $z = 0$, and for symmetric surfaces we obtain $m_\perp(-z) = -m_\perp(z)$ and $h_+ = -h_- \equiv h$. Using $m_\perp(\pm d/2) = \pm m_{\perp 0}$, the antisymmetric solution of the linear second-order differential equation (3.2) is given by

$$m_\perp(z) = m_{\perp 0}\frac{\sinh(z/\lambda)}{\sinh(d/2\lambda)}, \tag{3.5}$$

where we have defined the correlation length $\lambda = (b/a)^{1/2}$. Combining Eqs. (3.3) to (3.5) we obtain the polarization at the surface,

$$m_{\perp 0} = -\frac{h}{2a}\frac{1}{\lambda}\tanh(d/2\lambda). \tag{3.6}$$

The free energy Eq. (3.1) then follows as [42]

$$\frac{\beta\mathcal{F}}{A} = -\frac{h^2}{2a\lambda}\tanh(d/2\lambda), \tag{3.7}$$

from which the normal pressure is obtained via derivative with respect to the separation,

$$\beta\Pi_{\text{ind}} = -\frac{\partial\beta F/A}{\partial d} = \left(\frac{h}{a}\right)^2 \frac{a}{4\lambda\cosh^2(d/2\lambda)} \approx \beta\Pi^\star_{\text{ind}}\mathrm{e}^{-d/\lambda}. \tag{3.8}$$

The last result is valid for large distances $d \gg \lambda$ and shows that the pressure is repulsive and decays exponentially with an amplitude $\beta\Pi^\star_{\text{ind}} = (h/a)^2 a/\lambda$. The subscript "ind" in Eq. (3.8) denotes the fact that the free energy Eq. (3.1) does not include direct, membrane–membrane interactions, and thus only refers to the indirect, water–mediated, part.

3.2.1. Field theory

The phenomenological parameters in the Landau–Ginzburg model Eq. (3.1) are related to the polarization fluctuations of water. To obtain explicit expressions for these parameters we introduce the Landau–Ginzburg Hamiltonian of bulk water,

$$\beta H[\mathbf{m}] = \int \left[a\,(\mathbf{m}(\mathbf{r}))^2 + b(\nabla\cdot\mathbf{m}(\mathbf{r}))^2\right]\mathrm{d}\mathbf{r}, \tag{3.9}$$

with $\mathbf{m}$ the vectorial polarization density at position $\mathbf{r}$. For simplicity we consider the α-component of the polarization only in the following, with $\alpha \in \{x, y, z\}$. The Fourier transform $\tilde{m}_\alpha(\mathbf{q}) = \int e^{-i\mathbf{q}\cdot\mathbf{r}} m_\alpha(\mathbf{r})\,\mathrm{d}\mathbf{r}$ of the α-component of Eq. (3.9) yields

$$\beta H_\alpha[\tilde{m}_\alpha] = \int \frac{\mathrm{d}\boldsymbol{q}}{(2\pi)^3}\,\tilde{m}_\alpha(-\boldsymbol{q})\left(a + b\boldsymbol{q}^2\right)\tilde{m}_\alpha(\boldsymbol{q}). \tag{3.10}$$

The correlation function $\langle m_\alpha(\mathbf{r})m_\alpha(\mathbf{r}')\rangle$ can be obtained from the partition function in path integral representation,

$$\mathcal{Z}\left[h\right] = \int \mathcal{D}m_\alpha\,\exp\left\{-\beta H\left[m_\alpha\right] + \int \mathrm{d}\mathbf{r}\,h(\mathbf{r})m_\alpha(\mathbf{r})\right\}, \tag{3.11}$$

by functional derivatives,

$$\frac{\delta}{\delta h(\mathbf{r})}\frac{\delta}{\delta h(\mathbf{r}')}\log\mathcal{Z}[h]\Bigg|_{h=0} = \left\langle m_\alpha(\mathbf{r})m_\alpha(\mathbf{r}')\right\rangle - \left\langle m_\alpha(\mathbf{r})\right\rangle\left\langle m_\alpha(\mathbf{r}')\right\rangle \equiv G(\mathbf{r},\mathbf{r}'). \tag{3.12}$$

To calculate the functional derivative in Eq. (3.12), we introduce the kernel

$$G(\mathbf{q}) \equiv \frac{1}{2\left(a + b\boldsymbol{q}^2\right)}, \tag{3.13}$$

to obtain

$$\begin{aligned}\mathcal{Z}\left[h\right] &= \int \mathcal{D}\tilde{m}_\alpha\,\exp\left\{-\int \frac{\mathrm{d}\boldsymbol{q}}{(2\pi)^3}\,\tilde{m}_\alpha(-\boldsymbol{q})\frac{1}{2G(\boldsymbol{q})}\tilde{m}_\alpha(\boldsymbol{q}) + \int \frac{\mathrm{d}\boldsymbol{q}}{(2\pi)^3}\,\tilde{h}(-\boldsymbol{q})\tilde{m}_\alpha(\boldsymbol{q})\right\}\\ &= \mathcal{Z}[h=0]\exp\left\{\int \frac{d\boldsymbol{q}}{(2\pi)^3}\,\tilde{h}(-\boldsymbol{q})\frac{1}{2}G(\boldsymbol{q})\tilde{h}(\boldsymbol{q})\right\}.\end{aligned} \tag{3.14}$$

Using equation Eq. (3.12) we obtain for the correlation

$$G(\mathbf{r},\mathbf{r}') = \int \frac{d\boldsymbol{q}}{(2\pi)^3}\,\frac{1}{2\left(a + b\boldsymbol{q}^2\right)}e^{-i\boldsymbol{q}\cdot(\mathbf{r}-\mathbf{r}')}, \tag{3.15}$$

where we have back-transformed to real space. Making use of the rotational symmetry we perform the integral in spherical coordinates, and use $\langle m_\alpha(\mathbf{0})\rangle\,\langle m_\alpha(\mathbf{r})\rangle = \langle m_\alpha(\mathbf{0})\rangle^2$ to obtain

$$G(r) = \int \frac{\mathrm{d}\boldsymbol{q}}{(2\pi)^3} \frac{1}{2\,(a + b\boldsymbol{q}^2)} e^{-i\boldsymbol{q}\cdot\mathbf{r}} = \frac{1}{(2\pi)^2} \int_0^\infty \mathrm{d}q \, \frac{\sin(qr)}{r} \frac{q}{(a + bq^2)}. \tag{3.16}$$

Using residual calculus we can further evaluate this integral,

$$G(r) = \frac{1}{8\pi} \frac{\exp^{-r/\lambda}}{br}, \tag{3.17}$$

where we have used $\lambda = \sqrt{b/a}$. Equation (3.17) reveals a monotonic decay of the correlation function. However, due to the finite size of a water molecule it is unreasonable to go to wavelengths $2\pi/q$ smaller than the molecular size. We thus introduce a cutoff $q_{\max}$,

$$G(r) = \frac{1}{(2\pi)^2} \int_0^{q_{\max}} \mathrm{d}q \, \frac{\sin(qr)}{r} \frac{q}{a\,(1 + \lambda^2 q^2)}, \tag{3.18}$$

where $q_{\max}$ is an additional free parameter. We discuss the bulk water correlation function in Section 3.5.6 and only by introducing the cutoff oscillations are introduced to Eq. (3.18), which are also present in the bulk water correlation function. We obtain in Section 3.5.6 a value of $2\pi/q_{\max} \approx 0.2\,\mathrm{nm}$, roughly corresponding to the size of a water molecule.

3.2.2. Relation to the dielectric permittivity in bulk

A direct relation to the bulk dielectric permittivity can be obtained by performing the volume integral

$$\begin{aligned} C_\alpha &= \int \mathrm{d}\mathbf{r}\mathrm{d}\mathbf{r}' \left\langle m_\alpha(\mathbf{r}) m_\alpha(\mathbf{r}') \right\rangle - \left\langle m_\alpha(\mathbf{r}) \right\rangle \left\langle m_\alpha(\mathbf{r}') \right\rangle \\ &= \int \mathrm{d}\mathbf{r} G(r) V = V \int \mathrm{d}r 4\pi r^2 G(r) \\ &= V \int \mathrm{d}r \frac{r}{2b} \mathrm{e}^{-r/\lambda} = V \frac{\lambda^2}{2b} = \frac{V}{2a}, \end{aligned} \tag{3.19}$$

where we have used Eq. (3.17) in the last line.

Using the total polarization of the system, $\mathbf{M} = \int \mathrm{d}\mathbf{r}\,\mathbf{m}(\mathbf{r})$, Eq. (3.19) can be identified with the dielectric constant of an isotropic system [155],

$$\varepsilon_{\text{bulk}} = 1 + \frac{\langle \mathbf{M} \cdot \mathbf{M} \rangle}{3V\varepsilon_0 k_B T} = 1 + \frac{C_\alpha}{V\varepsilon_0 k_B T}. \tag{3.20}$$

Combining Eqs. (3.19) and (3.20) we obtain $a = [2(\varepsilon_{\text{bulk}} - 1)\varepsilon_0 k_B T]^{-1} \approx 5\,\mathrm{nm/e^2}$, where we used $\varepsilon_{\text{bulk}} = 70$ for SPC/E water at 300 K. Note, however, that Eq. (3.20) only holds in bulk, whereas the boundary conditions in confinement lead to different fluctuation formulae and the dielectric constant becomes both anisotropic and depending on the confinement [44, 156]. Also note that the above argument holds only if an isotropic, three-dimensional system is considered.

3.2.3. Elimination of the free parameters

We perform a step-wise elimination of the parameters in Eq. (3.1): First, we analyze the polarization profiles $m_\perp(z)$ and their contributions from the multipole expansion for different separations d by fitting Eq. (3.5) to the simulation data, where we enforce $\lambda = \sqrt{(b/a)}$ for each system to be independent of d. From these fits, the value at the surface $m_{\perp 0}$ is obtained, thus by fitting Eq. (3.6) we obtain the ratio h/a. Then, $a = V/2C_\perp$ following from Eq. (3.19) gives the last free parameter (which is proportional to the amplitude of the pressure, see Eq. (3.8)) and allows quantitative comparison of the pressure predicted by Eq. (3.8) with the simulation data Π_{ind}.

Before turning to the polarization profiles, we discuss the definition of the separation d in the following section. Then we show that our simulations are capable of reproducing experimental pressure–distance curves and decompose the total interaction pressure $\Pi_{\text{tot}} = \Pi_{\text{dir}} + \Pi_{\text{ind}}$ into direct membrane–membrane and indirect, water-mediated contributions.

3.3. Results

3.3.1. Definition of the separation

The proper definition of the membrane separation is crucial but not unique. We define the surface separation d for the analysis of the order parameter profiles based on the structural separation d_s, which is defined as the mean distance between the oxygen atoms of the opposing layers for Decanol and the mean distance between the phosphorus atoms of the opposing DPPC layers, respectively (see Fig. 3.1 (c)). From d_s we subtract the equilibrium separation at zero water content, $d = d_\text{s} - d_\text{s}^0$, see Fig. 3.1 (b). We obtain values $d_\text{s}^0 = 0.27\,\text{nm}$ for the Decanol system and $d_\text{s}^0 \approx 0.46\,\text{nm}$ for the phosphorus atoms in DPPC.

This definition of the effective surface separation describes the profiles and their surface values better when compared with Eqs. (3.5) and (3.6) than the water slab thickness d_w, defined in analogy to experiments [53] as $d_\text{w} = N_\text{w} v_\text{w}^\text{b}/A$, with the bulk molecular water volume $v_\text{w}^\text{b} = 0.0304\,\text{nm}^3$ and N_w the number of water molecules confined between the surfaces of lateral area A. Note that though this is the unambiguous thermodynamic surface position, in the Landau–Ginzburg description d is given by the position where the surface

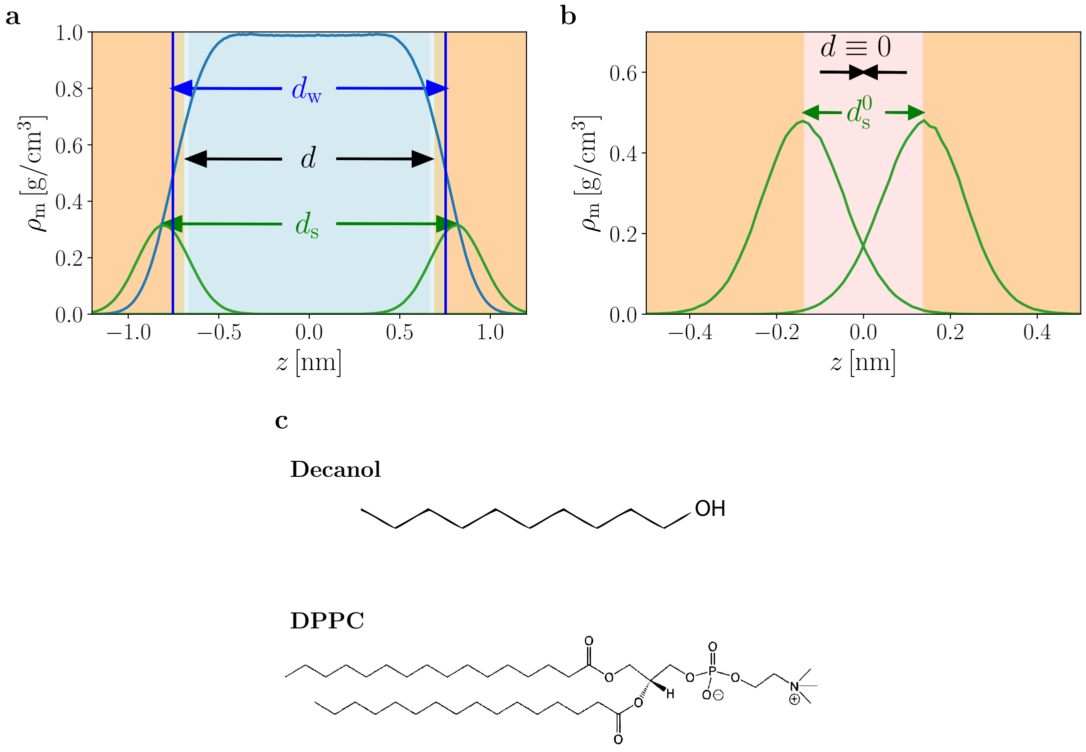

Figure 3.1.: **Definition of the separation d.** (a) Mass density ρ_m of water (blue line) and the headgroup (green line) for the Decanol system at a water slab thickness $d_\mathrm{w} = 1.5\,\mathrm{nm}$. Horizontal blue lines indicate the Gibbs Dividing surface positions, which define d_w, the light blue shaded area denotes the distance d, which follows from the difference between the headgroup separation d_s and the value at zero water content $N_\mathrm{w} = 0$, shown in (b). (c) Chemical structure of a Decanol a molecule and a DPPC lipid molecule.

coupling field $h_\pm$ enters the boundary condition in Eqs. (3.3) and (3.4). This boundary condition adds ambiguity to the definition of the surface separation. A comparison of both definitions is given in Section 3.5.2

3.3.2. Interaction Pressures

We now turn to the analysis of the interaction pressures. In Figure 3.3 (a) we show the interaction pressure for DPPC in the osmotic stress ensemble where the pressure is fixed to its bulk value, $\Pi_0 = 1\,\mathrm{bar}$. In our simulations we measure the chemical potential $\mu(N_\mathrm{w})$ and analogous to experiments convert this to equivalent osmotic pressures,

$$\Pi(N_\mathrm{w}) = \Pi_0 + \frac{\mu_\mathrm{b} - \mu}{v_\mathrm{w}^\mathrm{b}}, \tag{3.21}$$

where $v_\mathrm{w}^\mathrm{b} = 0.0304\,\mathrm{nm}$ denotes the simulated molecular volume of water in bulk at 1 bar pressure. Equation (3.21) follows from the formally exact thermodynamic Gibbs–Duhem equation as shown in Appendix A.

Comparison of the simulations (triangles in Fig. 3.2) with experimental data in gel and fluid states of the membranes taken from Refs. [7, 88, 140, 157, 158] shows excellent agreement among experimental and simulated pressure curves. The experimental decay length in the gel state is $\tilde{\lambda}^\mathrm{gel}_{\Pi\,(\mathrm{exp})} = 0.21 \pm 0.01\,\mathrm{nm}$, in the fluid state we obtain $\tilde{\lambda}^\mathrm{fluid}_{\Pi\,(\mathrm{exp})} = 0.38 \pm 0.02\,\mathrm{nm}$. The tilde indicates that the decay lengths are measured with respect to the water slab thickness d_w, which we plot in Fig. 3.3 (a) in order to compare our simulations to experimental data. Our simulations yield excellent agreement with $\tilde{\lambda}^\mathrm{gel}_{\Pi} = 0.22\,\mathrm{nm}$ and $\tilde{\lambda}^\mathrm{fluid}_{\Pi} = 0.36\,\mathrm{nm}$. In Figure 3.2 we also include simulation results for Decanol bilayers as black circles, which are performed at constant box volume $V = AL_z$ and the chemical potential is measured at a fixed value of L_z for different water numbers N_w, which allows extrapolating the pressures linearly from $\Pi(\mu)$ to $\Pi(\mu_\mathrm{b})$. Also for this system we observe an exponential decay with a length of $\tilde{\lambda}^\mathrm{Decanol}_{\Pi} = 0.08\,\mathrm{nm}$, indicated by the black line in Fig. 3.3 (a).

Using MD simulations at controlled water chemical potential via the Thermodynamic Extrapolation Method (TEM) to model hydrated bilayers in atomistic detail allows not only to quantitatively compare experimental and simulated interaction pressures but also to gain further insights into the interaction mechanisms (see Refs. [94, 98] and Appendix A). In the following analysis we perform simulations of DPPC in the hydrostatic ensemble, i.e., at bulk water chemical potential μ_b using the pressures extrapolated via Eq. (3.21), which allows to split the total interaction pressure Π_tot measured in this ensemble into direct membrane–membrane interactions Π_dir and an indirect, water mediated part Π_ind according to $\Pi_\mathrm{tot} = \Pi_\mathrm{dir} + \Pi_\mathrm{ind}$. For the simulations of Decanol the water num-

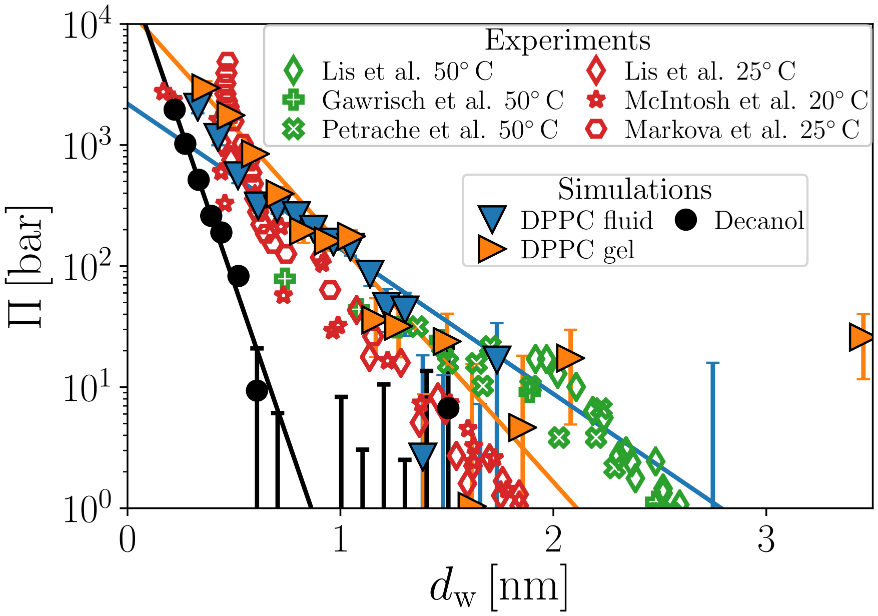

Figure 3.2.: **Interaction pressures between DPPC membranes and Decanol bilayers as a function of the water slab thickness d_w.** Experimental and simulation data for DPPC in the L_α and L_β phase, with exponential fits yielding $\tilde{\lambda}_\Pi^\mathrm{fluid} = 0.36\,\mathrm{nm}$ (blue line) and $\tilde{\lambda}_\Pi^\mathrm{gel} = 0.22\,\mathrm{nm}$ (orange line). Simulation data for the Decanol bilayers are shown as black circles with an exponential decay $\tilde{\lambda}_\Pi^\mathrm{Decanol} = 0.08\,\mathrm{nm}$. For comparison with experiments we show the pressure as a function of the water slab thickness d_w, denoted by the tilde in the decay lengths. Experimental data are taken from Refs. [7, 88, 140, 157, 158].

ber N_w correspondingly is adjusted such that the chemical potential equals the bulk value, $\mu = \mu_\mathrm{b}$, which allows to perform the latter analysis in this case.

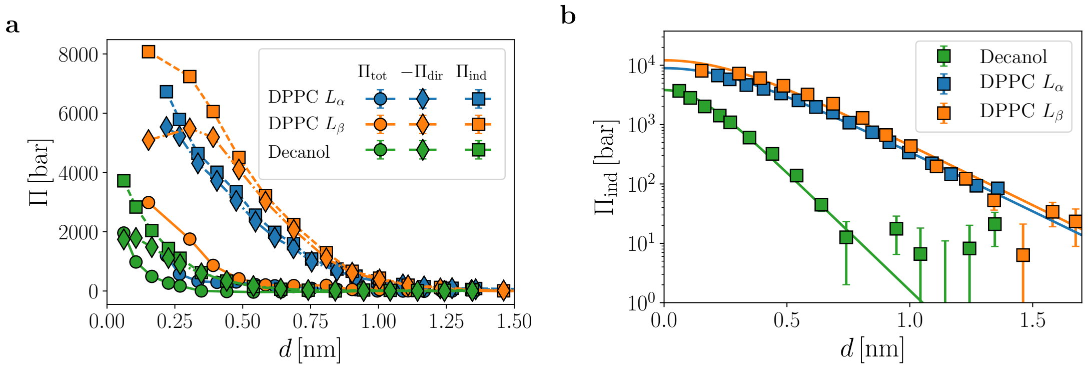

Figure 3.3.: **Interaction pressures decomposition.** (a) Decomposition of the total pressure Π_tot (circles) for the simulated systems into negative direct, membrane-membrane interactions $-\Pi_\mathrm{dir}$(diamonds) and indirect, water mediated contributions Π_ind (squares). (b) Indirect pressures and fits to the Landau–Ginzburg pressure Eq. (3.8). The corresponding decay lengths $\lambda_{\Pi_\mathrm{ind}}$ are given in Table 3.1.

The pressure decomposition in Fig. 3.3 (a) shows that for all systems the direct membrane–membrane interaction is strongly attractive, whereas the water-mediated forces are repulsive and slightly overcompensate the direct attraction, giving rise to the observed exponential decay of the total interaction. The attractive behavior between the surfaces directly rules out the membrane–membrane interactions as explanation for the hydration repulsion [98]. The near-cancellation of the two nearly exponential contributions at larger separations has been discussed recently [94] and is expected from electrostatic considerations: The direct attraction is mainly electrostatic in nature [98] and due to the electrostatic interaction of the polar headgroups across vacuum. The polarization of water reduces this energy to about $1/\varepsilon \approx 0.01$ of its value in vacuum, thus this simple electrostatic consideration, where $\varepsilon_\mathrm{bulk} = 70$ independent of the confinement is assumed, already shows that the two contributions compensate to a large degree; yet the electrostatic interactions alone result in attraction according to this viewpoint.

The indirect pressures are shown in Fig. 3.3 (b) on a logarithmic scale and indeed show the shape predicted by the Landau–Ginzburg theory, Eq. (3.8), which is shown as solid lines in Fig. 3.3 (b). The resulting values $\lambda_{\Pi_\mathrm{ind}}$ from fits to the indirect pressures in Fig. 3.3 (b) are given in Table 3.1. The amplitudes $\Pi^\star_\mathrm{ind}$ obtained are about 4 kbar for Decanol and 9 and 12 kbar for DPPC in the fluid and gel phase, respectively and compared to the results from analysis of the polarization in Table 3.3.

	Decanol	DPPC L_α	DPPC L_β
$\lambda_{\Pi_{\text{ind}}}$ [nm]	0.11	0.22	0.21
$\lambda_{m_\perp}$ [nm]	0.14	0.28	0.25
$\lambda_{m_\perp^{(1)}}$ [nm]	0.13	0.27	0.24
$\lambda_{m_\perp^{(2)}}$ [nm]	0.14	0.25	0.21

Table 3.1.: **Decay lengths of the indirect pressure.** The values $\lambda_{\Pi_{\text{ind}}}$ are obtained from fitting Eq. (3.8) to the data in Fig. 3.3 (b), and $\lambda_{m_\perp}$from the polarization, $\lambda_{m_\perp^{(1)}}$ from its dipole contribution $\lambda_{m_\perp^{(2)}}$ from the quadrupole contribution, shown in Fig. 3.4 via fits to Eq. (3.5).

3.3.3. Polarization profiles

We identify the membrane normal with the z-axis, $\perp = z$, and expand the perpendicular polarization density in terms of multipoles,

$$\begin{aligned} m_\perp(z) =& m_\perp^{(1)}(z) + m_\perp^{(2)}(z) + m_\perp^{(3)}(z) + \dots \\ \equiv& \frac{1}{A}\int \mathrm{d}x\mathrm{d}y \left[p_z(x,y,z) - \frac{1}{2}\frac{\mathrm{d}}{\mathrm{d}z} q_{zz}(x,y,z) + \frac{1}{6}\frac{\mathrm{d}^2}{\mathrm{d}z^2} o_{zzz}(x,y,z) + \dots \right], \end{aligned} \tag{3.22}$$

which comprises contributions to the laterally averaged perpendicular polarization $m_\perp^{(1)}$ from the dipole moment per volume $p_z = P_z/V$, $m_\perp^{(2)}$ from the quadrupole moment per volume $q_{zz} = Q_{zz}/V$, $m_\perp^{(3)}$ from the octupole moment per volume $o_{zzz} = O_{zzz}/V$, and contributions from all higher moments. We have also employed the lateral average $m_\perp(z) = 1/A \int \mathrm{d}x\mathrm{d}y\, m_\perp(x,y,z)$ with A the lateral area of the simulation box. For water, we calculate the dipole moment $P_i = \sum_l r_{il} q_l$ where the index l runs over the water hydrogens with charge q_l at position $\mathbf{r}_l$, measured with respect to the position of the oxygen atom of the considered water molecule, which is an arbitrarily chosen reference coordinate. Correspondingly, the quadrupole tensor can be defined as $Q_{ij} = \sum_l q_l r_{il} r_{jl}$ and the octupole tensor as $O_{ijk} = \sum_l q_l r_{il} r_{jl} r_{kl}$. To obtain the perpendicular component $m_\perp$ we set $i,j,k = z$. The bulk quadrupole term $Q_{\text{bulk}} = 1.411 \cdot 10^{-3}\,\mathrm{e\,nm}^2$, which depends on the arbitrarily chosen reference coordinate and has been determined independently [105, 129], is nonzero. However, order parameters describe the differences to bulk and we thus subtract Q_{bulk} whenever we discuss values of $q_\perp$ in the following.

We limit our analysis to the polarization profiles and their contributions up to the quadrupole moment as higher order terms cannot be evaluated sufficiently from our simulations due to statistical noise in the derivatives appearing in Eq. (3.22), see Section 3.5.5. In Figure 3.4 we show the polarization profiles for the three systems considered in this work at different separations d. All profiles agree excellently with the functional dependence

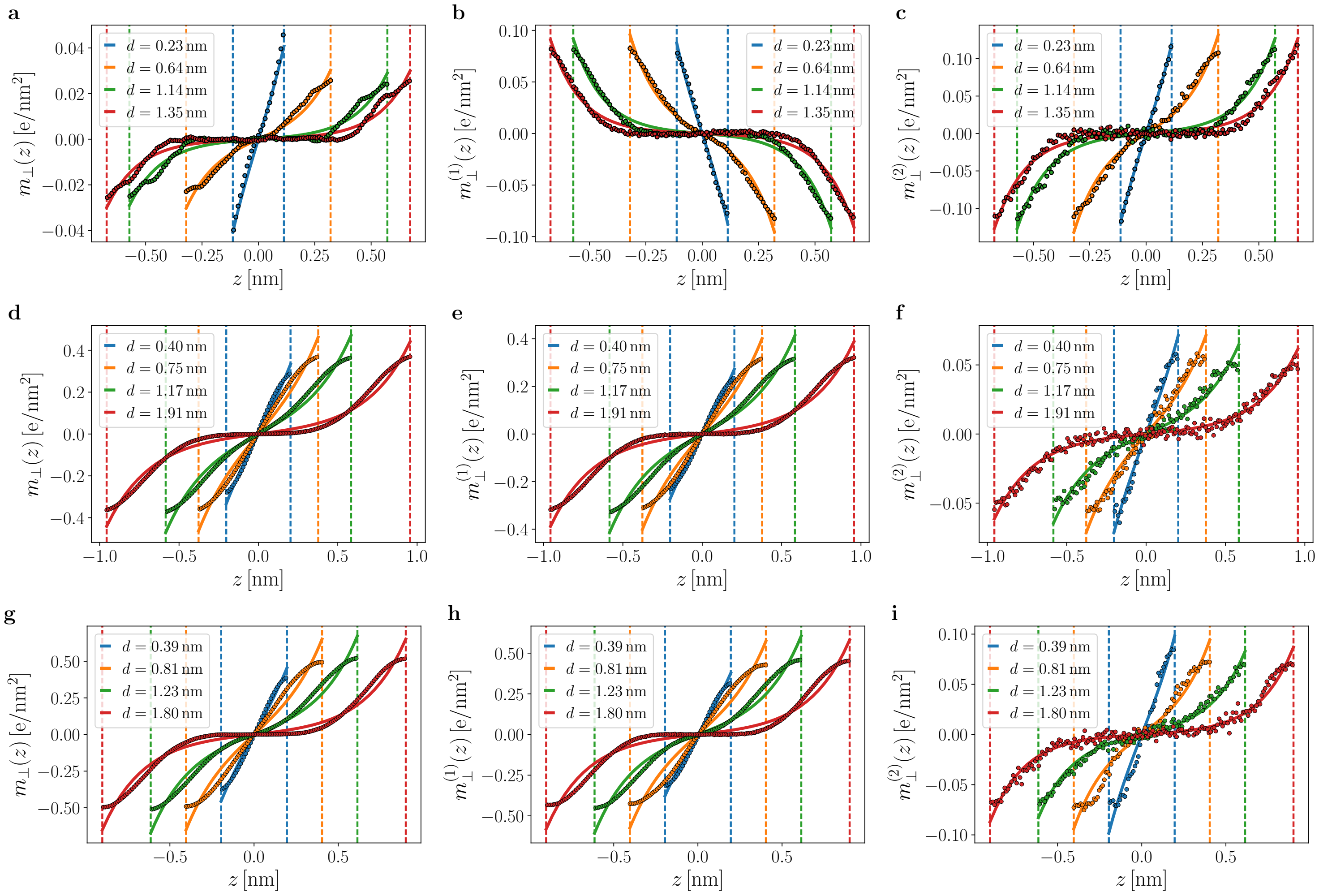

Figure 3.4.: **Polarization density profiles.** (a)-(c) Decanol bilayers, (d)-(e) DPPC in the disordered L_α phase and (g)-(h) DPPC in the ordered L_β phase. First column shows the polarization $m_\perp$, second column the dipolar contribution $m_\perp^{(1)}$ and third column the quadrupole contribution $m_\perp^{(2)}$. The dashed vertical lines indicate the surface position at $\pm d/2$, solid lines are fits according to Eq. (3.5) with the parameters λ summarized in Table 3.1 and the surface value $m_{\perp 0}$ shown in Fig. 3.6. The corresponding values of d are given in the legends.

expected from Eq. (3.5). Figures 3.4 (a)-(c) show the profiles for the Decanol bilayer system. Strikingly, one observes a near-cancellation of the dipole term in (b) with the quadrupole term in (c), leading to relatively small values of the polarization in (a) and which is dominated by the quadrupolar term. This picture is very different for the lipids shown in Figs. 3.4 (d)-(i), where the polarization $m_\perp$ and the dipole contribution $m_\perp^{(1)}$ are very similar. In this case one observes the quadrupole contribution in Figs. 3.4 (f) and (i) to contribute only about 10% to the polarization $m_\perp$.

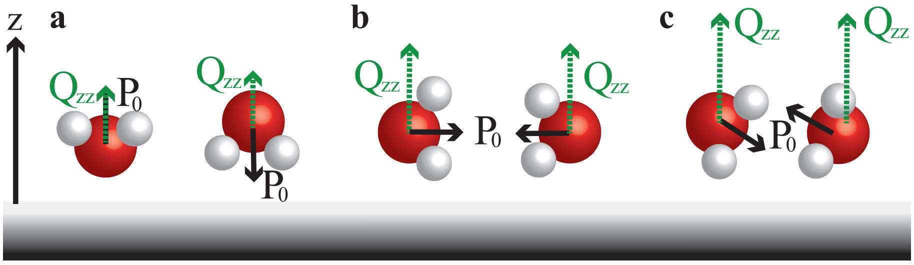

Figure 3.5.: **Illustration of the water orientation at an interface.** (a) Maximal dipole contribution P_0 in z-direction. In this case $P_0 \parallel Q_{zz}$. (b) The water dipole moment is perpendicular to the surface, thus $P_z = 0$, but the zz-component of the quadrupole Q_{zz} is larger than in (a). (c) Configurations with maximal quadrupole contribution Q_{zz} in z-direction. In this case the z-component of the dipole is $\approx 1/3 P_0$.

This qualitatively different behavior suggests a different water orientation at the interface, as illustrated in Fig. 3.5: If the perpendicular electric field due to the headgroups is very strong, the water molecules orient with their dipole moment parallel to the membrane normal (see Fig. 3.5 (a)). Using the SPC/E dipole moment $P_0 = 4.893 \cdot 10^{-2}\,\mathrm{e\,nm}$, full orientation corresponds to $m_\perp^{(1)} = P_0/v_\mathrm{w} = 1.61\,\mathrm{e/nm^2}$ and the zz-component quadrupole moment in this case is $Q_{zz} = 2.8 \cdot 10^{-3}\,\mathrm{e\,nm^2}$. Contrary, if lateral electric fields are (locally) larger than the perpendicular one, the water dipole preferably orients in-plane with the surface, Fig. 3.5 (b). Such a situation might arise due to the lipid charge distribution and the hydrogen bond network. An intermediate situation is shown in Fig. 3.5 (c), where the dipole moment in z-direction is about $1/3 P_0$, but the quadrupole moment is maximal with $Q_{zz} = 7 \cdot 10^{-3}\,\mathrm{e\,nm^2}$ as follows from geometric calculation using the HOH-angle of SPC/E water of 109.47°. Corresponding values for $q_\perp = Q_{zz}/v_\mathrm{w}$ are $0.23\,\mathrm{e/nm}$ for the orientation in Fig. 3.5 (c), and $q_\perp = 0.18\,\mathrm{e/nm}$ for (b), which can be compared to the profiles $q_\perp(z)$ shown in Section 3.5.7. Considering the surface values $m_\perp^{(1)}$ in Fig. 3.4 (e) and (h) the configuration shown on the right of Fig. 3.5 (c) well describes the dipole orientation at DPPC membranes as $m_\perp^{(1)}/3 \approx 0.54\,\mathrm{e/nm^2}$. For Decanol the values of the quadrupole contribution $m_\perp^{(2)}$ are very similar to the DPPC membranes, but the dipole contribution $m_\perp^{(1)}$ is smaller and has the opposite sign; whereas for the phospholipids the dipole orientation clearly overrules the quadrupole contribution, the opposite is the case for Decanol. This can only be explained by a linear combination of different configurations, some of which are exemplary shown in Fig. 3.5.

In Figure 3.6 we show the surface values $m_{\perp 0}$ for the three different systems. The polarization density for DPPC at the interface is well described by Eq. (3.6), indicated by solid lines in Fig. 3.6, revealing that the field h is the physically relevant boundary condition, as has been observed in prior studies [105]. The same observation applies for the contributions to the polarization from the dipole and quadrupole moments shown in Fig. 3.6 (b) and (c). For the Decanol system a more complex picture emerges, as at the surface the water dipoles point in the opposite direction compared to the DPPC lipid system, see Fig. 3.4 (b) and Fig. 3.6 (b). This is in line with the fact that the partial charge distribution of the simulation model employed for Decanol corresponds to a surface dipole which is pointing inwards the membrane; correspondingly, the dipole contribution $m_\perp^{(1)}$ for Decanol (green data in Fig. 3.6 (b)) is negative. In Figure 3.6 (c) one observes that for Decanol the quadrupole contribution is larger than for DPPC. However, the surface value of the polarization shown in Fig. 3.6 (a) for Decanol is small, as expected from the near-cancellation of the dipole and quadrupole contributions, see 3.5.5. At small distances the surface value for DPPC in Fig. 3.6 (a) deviates from the profile predicted by Eq. (3.6).

Via the fits to Eq. (3.6) presented in Fig. 3.6 we now have determined the prefactors h/a in Eq. (3.8), which are given for the polarization and its contributions in Table 3.2. We next turn to the analysis of the stiffness a, which is the only remaining free parameter, using Eq. (3.19). We have recently shown that the perpendicular polarization fluctuations in confinement differ drastically from bulk and in fact depend strongly on the confinement [156]. To estimate the free parameter according to Eq. (3.19), we compute $a = Ad_\mathrm{w}/(2C_\perp)$, where we have used the bulk water volume $V = Ad_\mathrm{w}$ for the normalization. Note that the integrals $C_\perp$ over $m_\perp$ and $C_\perp^{(1)}$ over $m_\perp^{(1)}$ are exactly equal,

$$
\begin{aligned}
M_\perp = A \int\limits_{-d/2}^{d/2} m_\perp(z) dz = A \int\limits_{-d/2}^{d/2} \frac{\partial}{\partial z} \left(z m_\perp(z) \right) dz \\
= A \left(z m(z) \Big|_{-d/2}^{d/2} + \int\limits_{-d/2}^{d/2} z \rho(z) \mathrm{d}z \right) = P_\perp = M_\perp^{(1)}, \quad (3.23)
\end{aligned}
$$

where the surface values at $\pm d/2$ exactly cancel and the second term is the definition of the dipole moment along the z-axis with ρ the charge density.

The modification of the perpendicular fluctuations is a collective effect of water in con-

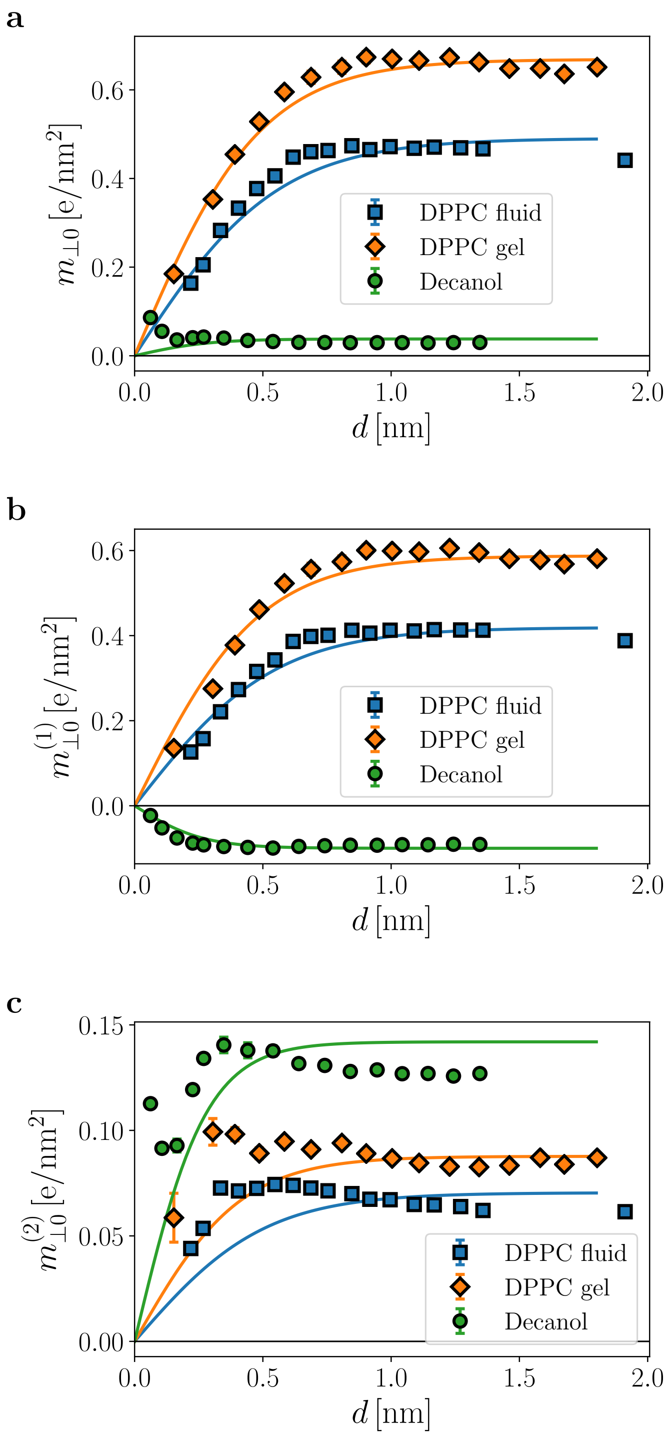

Figure 3.6.: **Polarization order parameter at the interface.** The values $m_{\perp 0}$ are obtained from the fits of the polarization profiles, Fig. 3.4 to Eq. (3.5). (a) Polarization $m_{\perp 0}$, (b) dipole contribution $m^{(1)}_{\perp 0}$ and (c) quadrupole contribution $m^{(1)}_{\perp 0}$. Solid lines denote fits of the amplitude h/a in Eq. (3.6) to the simulation data, with the corresponding correlation lengths λ taken from the fits in Fig. 3.4 (see Table 3.1).

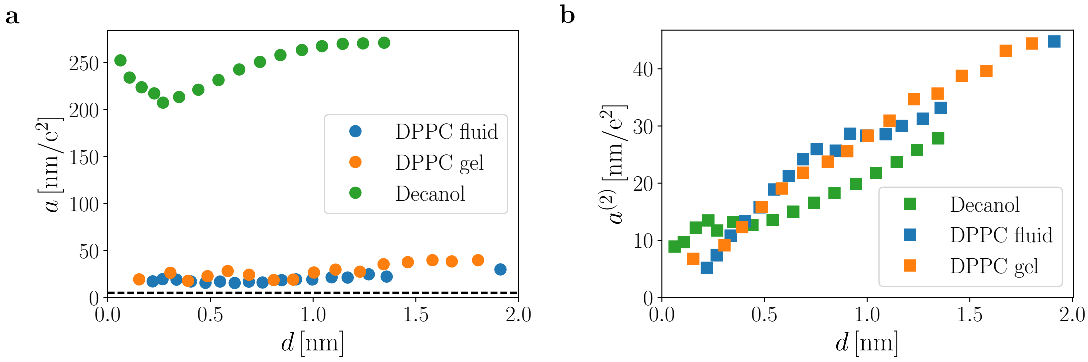

Figure 3.7.: **Free parameter for the pressure amplitude obtained from polarization fluctuations.** (a) Polarization fluctuations converted using Eq. (3.19) and the bulk water volume $V = Ad_\mathrm{w}$. The horizontal dashed line indicates the bulk value $a \approx 5\,\mathrm{nm/e^2}$. (b) Stiffness for the quadrupole contribution to the polarization from the surface value of the quadrupole density, Eq. (3.24).

	Decanol	DPPC L_α	DPPC L_β
h/a [e/nm]	0.005	0.136	0.165
$h^{(1)}/a^{(1)}$ [e/nm]	0.013	0.114	0.143
$h^{(2)}/a^{(2)}$ [e/nm]	0.020	0.018	0.018
a [nm/e^2]	212.5	19.5	28.2
$a^{(2)}$ [nm/e^2]	66.0	92.5	107.5

Table 3.2.: **Fitting parameters for the surface field and stiffness parameters.** The corresponding values have been obtained from the fits in Fig. 3.6 and from the distance-averaged values for a obtained from the data presented in Fig. 3.7.

finement and they do not converge to their bulk value even at the largest separations accessible in atomistic simulations of about 25 nm [156]. Figure 3.7 (a) shows the resulting values of a. The obtained distance-dependent values $a(d)$ from an analysis of the fluctuations in confinement are about four (for DPPC in the fluid L_α phase) up to fifty times larger (for Decanol) than in bulk, where $a \approx 5\,\mathrm{nm/e^2}$, obtained from the bulk dielectric constant via Eqs. (3.19) and (3.20) and indicated by the dashed black line in Fig. 3.7 (a). To obtain estimates for the indirect hydration pressure via Eq. (3.8) we take the mean value of a for the different separations, which are given in Table 3.2.

The stiffness $a^{(2)}$ for the quadrupole contribution follows from Eq. (3.19) as the surface value of the quadrupole density,

$$C_\perp^{(2)} = \left\langle \int \mathrm{d}\mathbf{r} \nabla q_\perp(\mathbf{r}) \int \mathrm{d}\mathbf{r}' \nabla q_\perp(\mathbf{r}') \right\rangle = 2A^2 q_{\perp\,0}^2, \tag{3.24}$$

	Decanol	DPPC L_α	DPPC L_β
$\Pi^\star_{\text{ind}}$ [kbar]	4	9	12
$\Pi^{\star\,m}_{\text{ind}}$ [kbar]	0.15	0.11	0.39
$\Pi^{\star\,m^{(1)}}_{\text{ind}}$ [kbar]	0.02	0.20	0.57
$\Pi^{\star\,m^{(2)}}_{\text{ind}}$ [kbar]	0.05	0.02	0.04

Table 3.3.: **Amplitudes of the indirect pressures.** The amplitudes $\Pi^\star_{\text{ind}}$ are obtained from the fits in Fig. 3.3 (b) and estimated values from analysis of the polarization density $\Pi^{\star\,m}_{\text{ind}}$ and its contributions from the dipole $\Pi^{\star\,m^{(1)}}_{\text{ind}}$ and the quadrupole $\Pi^{\star\,m^{(2)}}_{\text{ind}}$, for which the parameter a is averaged over the different separations.

where we have used Gauß' law which also directly cancels the expectation value $\left\langle \int \mathrm{d}\mathbf{r} \nabla q_\perp(\mathbf{r}) \right\rangle$ in Eq. (3.19) for symmetric order parameters. The corresponding values $a^{(2)}(d) = V/2C^{(2)}_\perp(d)$ are shown in Fig. 3.7 (c), where we again used the bulk water volume $V = Ad_w$ and the average over the separations is given in Table 3.2.

Combining the values (h/a) and a which are summarized in Table 3.2 with the decay lengths that follow from the polarization profiles, we can now estimate the amplitudes that the different terms of Eq. (3.22) contribute as

$$\Pi^\star_{\text{ind}} = \Pi_{\text{ind}}(d=0) = k_{\mathrm{B}} T a \left(\frac{h}{a}\right)^2 \frac{1}{\lambda^2} \tag{3.25}$$

and which we summarize in Table 3.3 together with the value obtained from fitting the simulation data in Fig. 3.3 (b). The striking difference in the dipole and quadrupole contributions between Decanol and DPPC also manifests in the pressure amplitudes: for Decanol the pressure is dominated by the quadrupole term $\Pi^{m^{(2)}}_{\text{ind}}$, with a nearly negligible contribution due to the dipole term $\Pi^{m^{(1)}}_{\text{ind}}$. The pressure due to the polarization Π^m_{ind} is slightly larger than the sum of the pressures due to the dipole and quadrupole terms. This is completely opposite for the DPPC systems, where the highest pressure is due to the dipole orientation, $\Pi^{m^{(1)}}_{\text{ind}}$, and the values $\Pi^{m^{(2)}}_{\text{ind}}$ are rather small. The pressures $\Pi^m_{\text{ind}} \neq \Pi^{m^{(1)}}_{\text{ind}} + \Pi^{m^{(1)}}_{\text{ind}}$ are non-additive, although the polarization is additive in Eq. (3.22)!

The elimination of all free parameters now allows to quantitatively compare the Landau–Ginzburg pressure in Eq. (3.8) with the indirect pressures Π_{ind} obtained from the simulations in Fig. 3.8. As observed in Table 3.3 our analysis reveals a multitude of contributions to the pressure. For the Decanol system (green data in Fig. 3.8) the polarization pressure Π^m_{ind} (dashed green line) is about five (at smallest separations) up to ten (at larger separations) percent of Π_{ind}. The pressures for the DPPC membranes are very similar in the liquid and gel phase and our analysis identifies the dipole contribution $\Pi^{m^{(1)}}_{\text{ind}}$ (dash-dotted blue and orange lines in Fig. 3.8) as largest pressure contribution, however for DPPC the

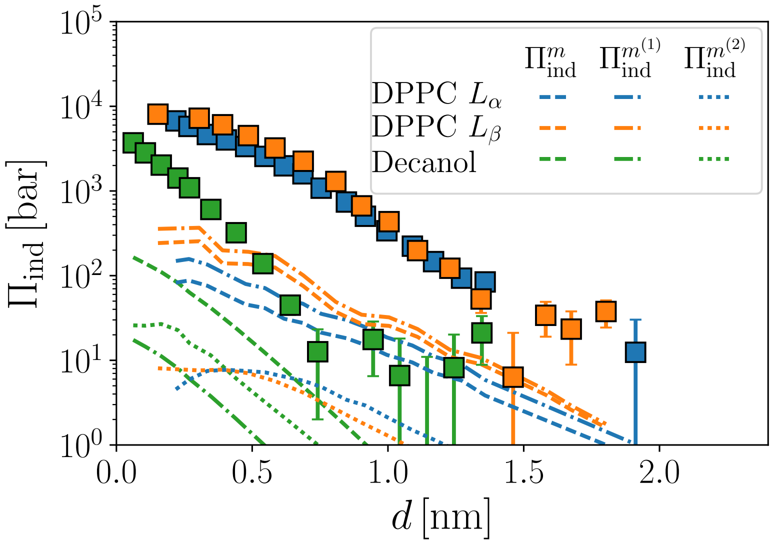

Figure 3.8.: **Indirect interaction pressures and Landau–Ginzburg prediction without free parameters.** Dashed lines show the pressure following from the polarization, Π^m_{ind}, dash-dotted lines the corresponding pressures if only the dipole term is considered, $\Pi^{m^{(1)}}_{\text{ind}}$, and dotted lines the pressure from the quadrupole term, $\Pi^{m^{(2)}}_{\text{ind}}$. Distance-dependent values for a and $a^{(2)}$ are directly taken from Fig. 3.7 (a) and (c).

polarization pressures Π^m_{ind} (dashed blue and orange lines) also are significant with about 50% of $\Pi^{m^{(1)}}_{\text{ind}}$. Contrary, the quadrupole polarization $\Pi^{m^{(2)}}_{\text{ind}}$, shown as dotted orange and blue lines in Fig. 3.8, is about an order of magnitude smaller. In total the different contributions from analysis of the polarization density in the Landau Ginzburg model account for about ten percent of the indirect pressure (data shown as squares in Fig. 3.8).

3.4. Conclusion

Relating the phenomenological parameter in the Landau–Ginzburg free energy to the order parameter fluctuations we have determined all free parameters of this model, which allows to quantitatively compare the pressures due to water polarization with the simulation data of the water-mediated, indirect pressures. We observe a striking difference between Decanol surfaces and DPPC bilayers in the pressure contributions due to different order parameters, which reveals that a single order parameter, such as the polarization or the components of a multipole expansion of the latter, is not sufficient to model the repulsive hydration force. We find that rather a multitude of the different contributions has to be considered.

The fact that the repulsion in the Marčelja–Radić model under the surface field boundary condition is only obtained for antisymmetric order parameters crucially limits the possible candidates. Further candidates are the antisymmetric terms of the water multipole itself, i.e., the octupole orientation, fifth moment, seventh moment and so on. However we find that already the octupole orientation contributes negligibly to the repulsion (shown in Section 3.5.7). Thus we conclude that the amplification of the repulsion is due to effects that are neglected in a mean-field analysis, like lateral correlations due to (local) parallel polarization of the headgroups. Further contributions could stem from the finite width of the surface coupling field [152, 159] and lateral inhomogeneities [150, 151], of which both essentially modify the prefactor of the pressure. However, insights to the molecular nature of the hydration force follow from the analysis of the dipolar and quadrupolar contributions, and reveal a significant influence of the surface chemistry via the local field and the tendency to form hydrogen bonds [149]; our results suggests that the water orientation indeed gives rise to a significant repulsive pressure between lipid membranes.

3.5. Supplemental material

3.5.1. Simulation details

All simulations are performed using the GROMACS package version 5.0 [126] for Decanol and version 4.6 [160] for DPPC with periodic boundary conditions and analyzed using the MDAnalysis package [127]. All simulations are performed with periodic boundary conditions and a time step of 2 fs. Lennard–Jones interactions are truncated at $r_\mathrm{c} = 0.9\,\mathrm{nm}$, for the electrostatic interactions the Particle Mesh Ewald method [128] is employed with a real-space cut-off $r_\mathrm{c} = 0.9\,\mathrm{nm}$.

Decanol bilayer

For the Decanol bilayer we simulate a slab between two planar surfaces consisting of $N_\mathrm{l} = 100$ polar Decanol $CH_3(CH_2)_9OH$ molecules filled with $N_\mathrm{w} = 170$ up to $1\,160$ SPC/E water molecules [91] in between. Force-field parameters are based on GROMOS53A6 [92], Decanol hydroxyl groups are represented in atomistic detail, CH_2 and CH_3 groups as united atoms. The repulsion between headgroup oxygens is increased to reduce intra-surface hydrogen bonding [125]. To avoid slow reorientation events, we restrain all Decanols on the second CH_2 group counting from the OH headgroup with force constants $k_x = k_y = 500\,\mathrm{kJ/(mol\,nm^2)}$ and $k_z = 10\,\mathrm{kJ/(mol\,nm^2)}$ and the terminal CH_3 group with $k_x = k_y = 5\,\mathrm{kJ/(mol\,nm^2)}$ on a centered rectangular lattice with a lateral area per headgroup of $A/N_\mathrm{l} = 0.234\,\mathrm{nm}^2$. This corresponds to the tensionless state in vacuum with a Decanol tilt angle of 30°. Simulations are performed in the $N_\mathrm{w}AL_zT$ ensemble at constant volume $V =$

AL_z and the number of water molecules N_w is adjusted via thermodynamic extrapolation to yield a constant chemical potential [98]. The extrapolation thus employs at least three sets of simulations at fixed L_z with different numbers N_w. We use 18 simulations along the free energy perturbation reaction coordinate to obtain the chemical potential $\mu(N_\mathrm{w})$ using the MBAR method [161]. Each individual trajectory has a length of 100 ns, thus the total sampling time per data point in the pressure–distance curve for Decanol is about 6 μs.

Simulation of DPPC in the gel and fluid phase

For DPPC simulations we use the Berger lipid force field [93, 162, 163] and the SPC/E water model [91]. The assisted freezing method [164] is used for the construction of fully hydrated membranes in the L_β (gel) phase at a temperature of $T = 270\,\mathrm{K}$, controlled by the v–rescale thermostat [165]. This fully hydrated membrane consists of 2×36 DPPC lipids hydrated by 40 water molecules per lipid. The structure is equilibrated at $T = 300\,\mathrm{K}$ and afterwards gradually dehydrated by one molecule per lipid and each time equilibrated for 5 ns down to a hydration level of 3 waters per lipid molecule. All equilibrations are performed in the $N\Pi_0T$ ensemble. To improve sampling, we use four different starting configurations, which are independently dehydrated five times with different random seeds, giving 20 different systems per hydration level. For production runs in the L_α fluid phase the temperature in the gel state is increased to 330 K, above the melting temperature of DPPC membranes in experiment and in simulations [166–169].

An anisotropic pressure coupling is employed using the Berendsen barostat [93] with a time constant of $\tau_P = 2\,\mathrm{ps}$. Each system is simulated for 5 ns, so the total simulation time is 100 ns per hydration level. In the osmotic ensemble, the pressure is set to $\Pi = 1\,\mathrm{bar}$ and the chemical potential μ is measured. From the 20 different systems per hydration level the error of the chemical potential and thus the osmotic pressure is estimated, for which we perform 18 simulations along the free energy perturbation reaction coordinate. Prior to the production run, fluid and gel membranes at all hydration levels are equilibrated for at least 5 ns and production runs are performed over another 5 ns, thus the total simulation time for the pressure–distance curves of DPPC exceeds 60 μs. The hydrostatic simulations, used to decompose the pressure into direct and indirect parts, employ the predicted osmotic pressure, and we explicitly verified that the resulting chemical potential equals the bulk water chemical potential.

3.5.2. Distance definition

Figure 3.9 shows a comparison of the effective distance d versus the water slab thickness d_w for the three systems considered. By definition of $d = d_\mathrm{s} - d_\mathrm{s}^0$ the intercept with the y-axis is zero, i.e., the first water layer per lipid does not increase the structural separation d_s. The inset of Fig. 3.9 shows d as a function of the number of waters per lipid molecule, $N_\mathrm{w}/N_\mathrm{l}$. The different slopes correspond to the area per lipid molecule via $N_\mathrm{w}/N_\mathrm{l} = Ad_\mathrm{w}/(v_\mathrm{w}N_\mathrm{l})$. Also in this case the intercept with the y-axis is zero by definition. Correspondingly, the first water layer upon hydration gets bound inside the bilayer and the water partial volume is smaller than in bulk, a behavior that is also found e.g. in glycolipid membranes [149].

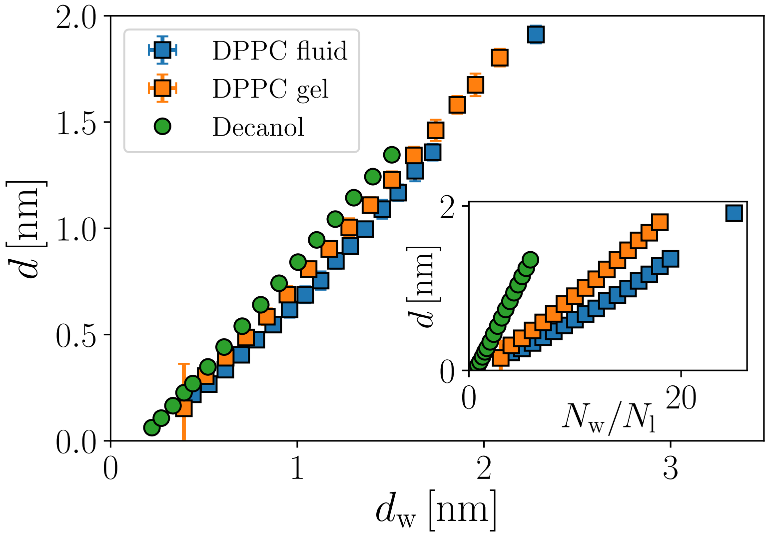

Figure 3.9.: **Structural separation** based on the oxygen (Decanol) and phosphorus distance (DPPC) as a function of the water slab thickness d_w. The inset shows d as a function of the number of waters per headgroup, $N_\mathrm{w}/N_\mathrm{l}$.

The corresponding area per surface molecule is shown in Fig. 3.10. Whereas for simulations of DPPC the lateral area adjusts such that the lateral pressure is 1 bar, which corresponds to the experimental situation in the osmotic stress ensemble [170], we fix the area in the simulations of Decanol independently of the hydration to $A/N_\mathrm{l} = 0.234\,\mathrm{nm}^2$, which corresponds to the tensionless state in vacuum. The change of the area per lipid of DPPC at different water slab thickness d_w is the origin of the nonlinear behavior observed for $d(d_\mathrm{w})$ in Fig. 3.9.

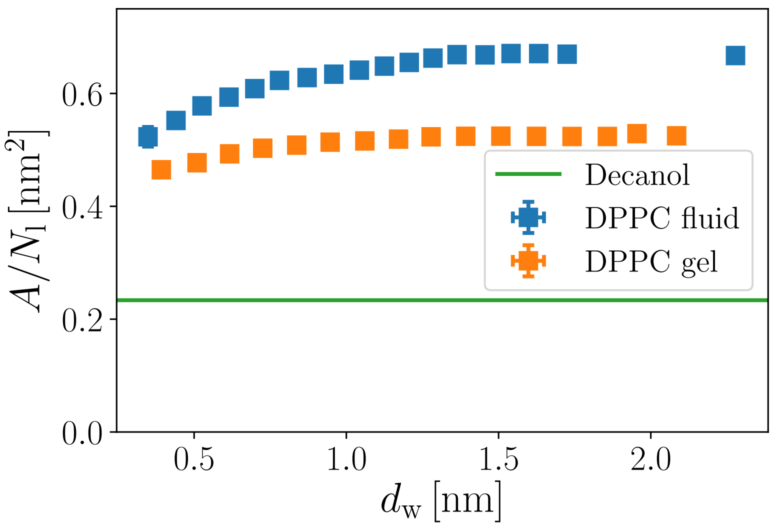

Figure 3.10.: **Area per lipid molecule.** For simulations of DPPC the lateral area adjusts such that the lateral pressure is 1 bar, whereas for the simulations of Decanol the area is fixed independent of the hydration.

3.5.3. Decomposition of the interaction pressure

As membrane–membrane interactions are not treated within a continuum model of the water orientation, in order to relate the interaction pressure to the Landau–Ginzburg model, we decompose the pressure into direct, membrane–membrane contributions and an indirect part, which is mediated by water. To this end we re-evaluate the simulation trajectories where the simulation box is expanded in z-direction such that on each side of the water slab, which is in the center of the box, there is only one leaflet of the membrane, see Fig. 3.11 (a). This way interactions with periodic images in z-direction are minimized as Lennard-Jones interactions are zero behind the cut-off r_c and the electrostatic attraction, which is mainly due to dipolar interactions, decays as d^{-4}. Note that pseudo-2D summation of the electrostatic forces [171] does not change this decomposition as we sum over the net neutral membrane leaflet. To measure the direct contributions, also the water slab is removed, thus only the opposing membrane leaflets, which interact with each other across the free space (Fig. 3.11 (b)), are left. The force acting on one of the leaflets divided by the area gives the direct contribution to the hydration pressure. In order to obtain the indirect contribution, one leaflet is removed instead of the water, and again the force acting on the remaining leaflet is measured (Fig. 3.11 (c)). The obtained total pressures Π_tot (circles in Fig. 3.3 (b)) agree perfectly with the interaction pressures obtained from the virial, revealing that the interaction with the periodic neighbors has a

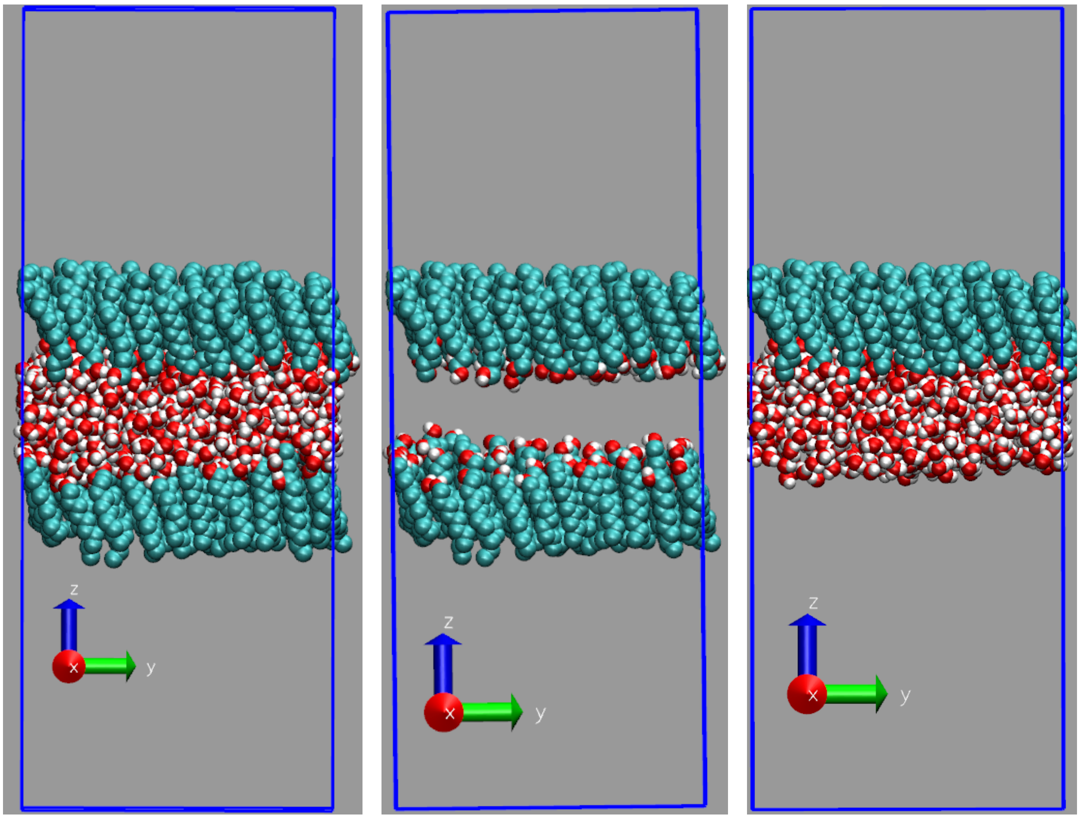

(a) (b) (c)

Figure 3.11.: **Simulation setup for pressure splitting.** (a) The total force acting on the upper membrane leaflet is measured in a box that is expanded such that periodic replica can be neglected. (b) For direct, membrane–membrane interactions the water is removed and the force on the upper leaflet is measured. (c) To obtain the forces of the water acting on the surface, the lower leaflet is removed.

negligible contribution to the hydration force and validating our method.

3.5.4. Landau expansion with generalized boundary conditions

We briefly summarize the Landau expansion of the free energy $\mathcal{F}$ in terms of an arbitrary scalar order parameter $\eta(z)$, for which we make use of the slab symmetry and define the laterally averaged order parameter as $\eta(z) = 1/A \int \mathrm{d}x\mathrm{d}y\, \eta(x,y,z)$. The derivation also holds for vectorial order parameters [153]. Bulk water is not structured, thus no odd terms appear in the expansion. Including surface fields h that couple linearly to η and g that couple quadratically [172], the free energy expansion up to the quadratic term is given as

$$\frac{\beta\mathcal{F}\left[\eta(\cdot)\right]}{A} = \int_{-d/2}^{d/2} \left[a\eta^2(z) + b\left(\nabla\eta(z)\right)^2\right] \mathrm{d}z + h_+\eta(\frac{d}{2}) + h_-\eta(-\frac{d}{2}) + g_+\eta^2(\frac{d}{2}) + g_-\eta^2(-\frac{d}{2}). \tag{3.26}$$

Performing the variation yields

$$\begin{aligned}\frac{\beta\delta\mathcal{F}[\eta(\cdot)]/A}{\delta\eta(\tilde{z})} = 2a\eta(\tilde{z}) - 2b\nabla^2\eta(\tilde{z}) + \delta(\frac{d}{2} - \tilde{z})\left[h_+ + 2b\nabla\eta(\frac{d}{2}) + 2g_+\nabla\eta(\frac{d}{2})\right] \\ + \delta(\frac{d}{2} + \tilde{z})\left[h_- - 2b\nabla(-\frac{d}{2}) + 2g_-\nabla\eta(-\frac{d}{2})\right].\end{aligned} \tag{3.27}$$

The antisymmetric solution, $h_+ = -h_- \equiv h$, of Eq. (3.27) is given by [153]

$$\eta(z) = -\frac{h}{2b}\frac{\sinh\left(z/\lambda\right)}{\cosh(d/2\lambda) + \chi\sinh\left(d/2\lambda\right)}, \tag{3.28}$$

where we have used $\lambda = (b/a)^{1/2}$ and $\chi = g\lambda/b = g(ab)^{-1/2}$. Thus, χ essentially is the ratio between the stiffness at the surface g and the (square root) of its value far away from the surface a times the parameter b determining the range of interaction. The free energy then follows from Eq. (3.26) as

$$\frac{\beta\mathcal{F}}{A} = \frac{h^2\lambda}{2b}\frac{1}{\chi + \coth(d/2\lambda)}. \tag{3.29}$$

For $\chi \to 0$, Eq. (3.5) is recovered and the surface value $\eta_0 = \pm\eta(\pm d/2)$ follows the field h,

$$\eta_0 = \frac{h}{2a\lambda}\tanh(d/2\lambda), \tag{3.30}$$

and the free energy simplifies to

$$\frac{\beta\mathcal{F}}{A} = \frac{h^2\lambda}{2b}\frac{1}{\coth(d/2\lambda)}, \tag{3.31}$$

which is the expression obtained by Cevc et al. [42]. We used this expression for our analysis in favor of Eq. (3.28) as one free parameter less is employed and the simulation results can be modeled excellently using Eq. (3.30). The resulting pressure is repulsive and follows from the derivative of Eq. (3.31),

$$\Pi_{\text{ind}} = -\frac{\partial}{\partial d}\frac{\beta\mathcal{F}}{A} = \frac{h^2}{4b}\frac{1}{\cosh^2(d/2\lambda)}, \tag{3.32}$$

where the subscript "ind" denotes the fact that the Landau–Ginzburg model does not account for direct membrane–membrane interactions.

In the opposite limit, $\chi \to \infty$, the surface stiffness g dominates and thus η_0 is expected to be independent of the confinement. Expanding Eq. (3.26) to leading order, this results in

$$\frac{\beta\mathcal{F}}{A} = -\frac{h^2\lambda}{2b\chi^2}\coth\left(\frac{d}{2\lambda}\right), \tag{3.33}$$

and the corresponding pressure follows as

$$\Pi_{\text{ind}} = -\frac{\partial}{\partial d}\frac{\beta F}{A} = -a\eta_0^2\frac{1}{\sinh^2(d/2\lambda)}, \tag{3.34}$$

which reveals attraction. Note that for $d \gg \lambda$ both expressions Eqs. (3.32) and (3.34) show an exponential decay,

$$\Pi_{\text{ind}}(d \gg \lambda) \approx \pm\Pi^{\star}_{\text{ind}}\mathrm{e}^{-d/\lambda}, \tag{3.35}$$

however, the behavior at small separations is very different [173]: Whereas for $\chi \to 0$ the pressure saturates, it diverges for the constant value of η_0 at $\chi \to \infty$.

Similarly, the solution for symmetric order parameters $h_+ = h_- \equiv h$ follows as

$$\eta(z) = -\frac{h}{2b}\frac{\cosh(z/\lambda)}{\cosh(d/2\lambda) + \chi\sinh(d/2\lambda)}, \tag{3.36}$$

with the free energy

$$\frac{\beta\mathcal{F}}{A} = -\frac{h^2\lambda}{2b}\frac{1}{\chi + \tanh(d/2\lambda)}. \tag{3.37}$$

In the limit $\chi \to 0$ the profile simplifies to

$$\eta(z) = \eta_0 \frac{\cosh(z/\lambda)}{\cosh(d/2\lambda)}, \tag{3.38}$$

where the surface value of the order parameter then is given by [173]

$$\eta_0 = \frac{h}{2a\lambda}\coth(d/2\lambda), \tag{3.39}$$

and the resulting interaction pressure,

$$\Pi_{\text{ind}} = -\frac{\partial}{\partial d}\frac{\beta\mathcal{F}}{A} = -\frac{h^2}{4b}\frac{1}{\sinh^2(d/2\lambda)}, \tag{3.40}$$

is attractive.

Performing the expansion as above in the limit $\chi \to \infty$, the free energy follows as

$$\frac{\beta\mathcal{F}}{A} = \frac{h^2\lambda}{2b\chi^2}\tanh\left(\frac{d}{2\lambda}\right), \tag{3.41}$$

thus in this case where $\eta(d) = \eta_0$ is constant, the pressure is repulsive,

$$\Pi_{\text{ind}} = -\frac{\partial}{\partial d}\frac{\beta\mathcal{F}}{A} = a\eta_0^2\frac{1}{\cosh^2(d/2\lambda)}. \tag{3.42}$$

3.5.5. Multipole moments of the polarization density and relation to the dipole orientation

In Figure 3.12 we exemplary show the contributions to the polarization density up to the octupole moment according to Eq. (3.22) for the Decanol bilayers at $d = 1.35\,\text{nm}$ and in Fig. 3.12 (b) for DPPC in the liquid state at $d = 1.7\,\text{nm}$. In both cases the octupole term (red line in Fig. 3.12 (a) and (b)) is zero within the numerical noise. Smoothing the data via a gliding window average before taking the derivative, shown in the inset of Fig. 3.12, does not yield profiles that agree well with the sinh-shape expected from the Landau–Ginzburg theory. As discussed in the main text, the quadrupole contribution for Decanol over-compensates the dipole term, giving rise to the different sign between $m_\perp^{(1)}$ and $m_\perp$. Contrary, for DPPC in Fig. 3.12 the quadrupole term adds up with the dipole term and contributes roughly 10% in this case.

When analyzing the water dipole orientation via the cosine with the membrane normal, the question of the influence of the water density naturally arises. To quantify this difference we plot in Fig. 3.12 (c) the dipolar polarization density profile $m^{(1)}(z)$. In our analysis this is computed as $m^{(1)}(z) = P_0\langle\rho(z)\cos\Theta(z)\rangle$, with $P_0 = 4.893\cdot 10^{-2}\,\text{e nm}$,

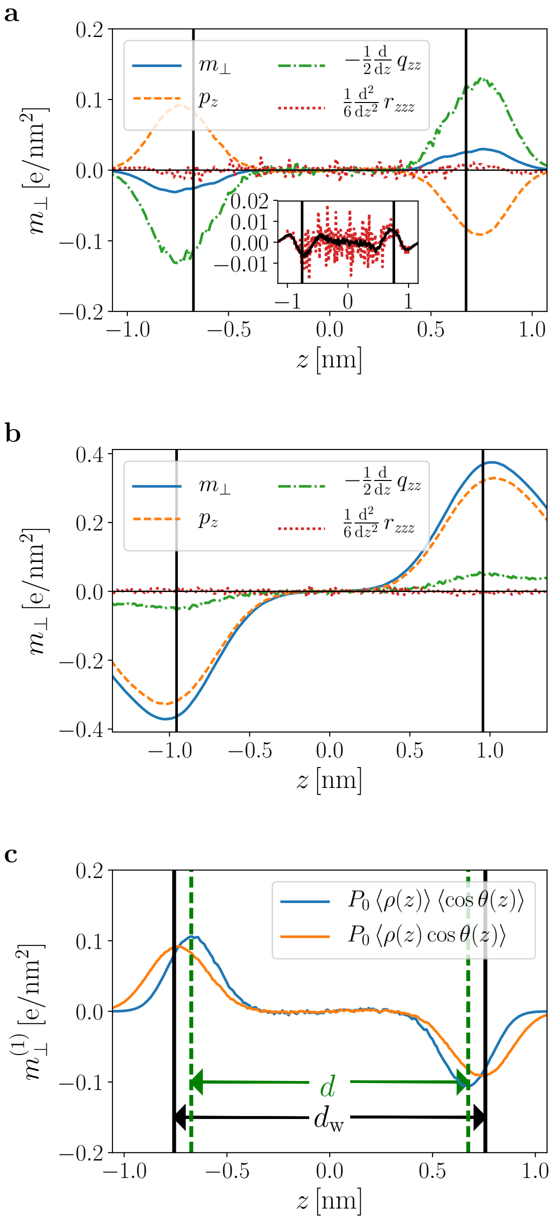

Figure 3.12.: **Multipole expansion of the polarization density.** (a) Polarization density of Decanol at $d_\mathrm{w} = 1.5\,\mathrm{nm}$. The total polarization (blue) is split into contributions stemming from dipoles (orange) and quadrupoles (green), whereas we find the octupole term (red) to be zero within numerical noise. Vertical black lines indicate the position of the Gibbs Dividing surface, equivalent to d_w. The inset shows the smoothed second derivative of the octupole moment. (b) Same as in (a) but for DPPC in the liquid state at $d_\mathrm{w} = 1.73\,\mathrm{nm}$. (c) Average polarization density and density weighted dipole orientation for Decanol at $d_\mathrm{w} = 1.5\,\mathrm{nm}$. The vertical black line denotes the position of the GDS, the dashed green line denotes the interface position using the structural distance d.

the dipole moment of SPC/E water. On the other hand, a density weighted orientation follows as $P_0 \langle \rho(z) \rangle \langle \cos\Theta(z) \rangle$. As observed from the data in Fig. 3.12, polarization and density are correlated, resulting in the different profiles for both averages. The product $P_0 \langle \rho(z) \rangle \langle \cos\Theta(z) \rangle$ (blue line in Fig. 3.12 (c)) has a maximum incidentally at the position of the surface defined by the structural distance, indicated as vertical dashed green line in Fig. 3.12 (c).

3.5.6. Bulk water polarization fluctuations

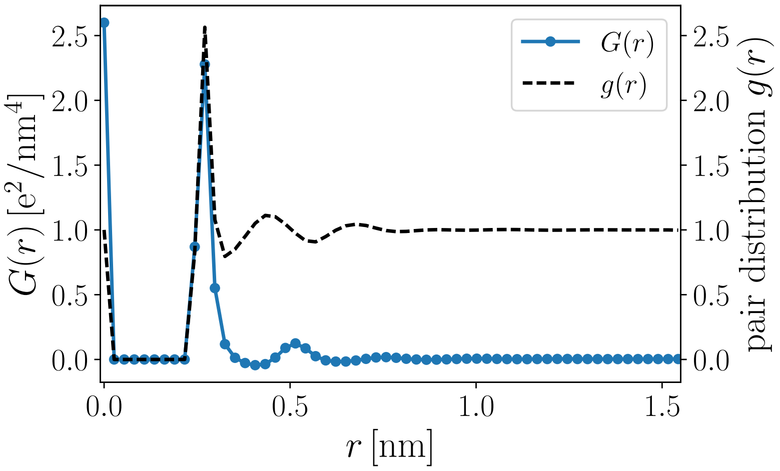

Figure 3.13.: **Correlation of the water dipole polarization.** Data in blue presents the scalar product Eq. (3.43), shown on the right side axis is the pair distribution function.

To exclude finite size effects we perform simulations of bulk water in cubic simulation boxes consisting of $N_\mathrm{w} = 1477, 4074$ and 17021 water molecules, corresponding to box lengths of $L = 3, 5$ and 8 nm at ambient pressure. In Fig. 3.13 we show the scalar product of the water dipole density,

$$G(r) = \left\langle \mathbf{m}^{(1)}(0) \cdot \mathbf{m}^{(1)}(r) \right\rangle \tag{3.43}$$

as blue symbols. For comparison we also include the pair distribution function $g(r) = 1/(4\pi r^2)\,\mathrm{d}N(r)/\mathrm{d}r$, where $N(r)$ is the number of water molecules in a sphere of radius r, measured with respect to the water oxygen atom, as black line in Fig. 3.13. Fits of the data to the expressions Eqs. (3.17) and (3.18) are subtle as water molecules have a finite size, thus the cut-off q_max has to be included. Additionally, the correlation decays quickly with separation r , thus making a numerical comparison challenging. Performing the integral as proposed by Eq. (3.19),

$$2\int \mathrm{d}r 4\pi r^2 G(r) = a^{-1}, \tag{3.44}$$

yields the parameter a, however comparison with Eq. (3.20) is subtle due to the combination of finite size effects and numerical artifacts shown in Fig. 3.14.

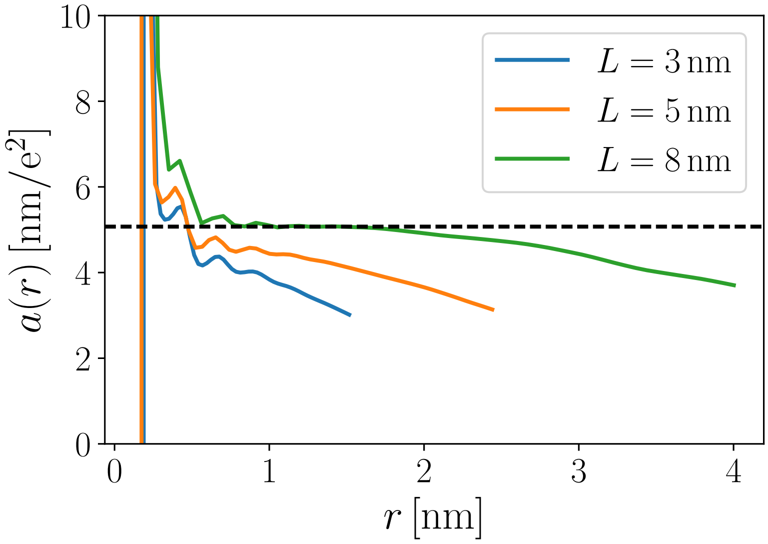

Figure 3.14.: **Running integral over the polarization fluctuations.** Simulation results for box sizes $L = 3\,\mathrm{nm}$, $L = 5\,\mathrm{nm}$ and $L = 8\,\mathrm{nm}$ are shown. The horizontal dashed line shows the bulk value obtained from the bulk dielectric permittivity via Eq. (3.20).

We show in Figure 3.14 the running integral Eq. (3.44), where the bulk value $a = 5.01\,\mathrm{nm/e^2}$, indicated by the dashed black line in Fig. 3.14, is obtained only for the largest box we simulated, $L = 8\,\mathrm{nm}$ (green line). The obtained values match the bulk value in this case between $1\,\mathrm{nm} < r < 2\,\mathrm{nm}$. The deviations at larger r might be due to numerical artifacts in the evaluation of $G(r)$, or due to finite size effects as we observe that $G(r)$ does not decay to zero.

3.5.7. Quadrupole and octupole moment as order parameters

The identification of the order parameter with the polarization density is not unique. However, the candidates for possible order parameters that are antisymmetric with respect to the symmetry plane is quite limited. Possible candidates are the odd terms appearing in the multipole expansion, Eq. (3.22). We therefore now discuss the next antisymmetric term after the dipole, namely the zzz-component of the octupole density, $o_\perp = \langle O_{zzz}(z)\rho(z)\rangle$.

The octupole moment of water is defined in the main text as $O_{zzz} = \sum_l q_l \Delta z_l^3$, where the sum is over the water hydrogens, with Δz being their distance to the corresponding oxygen. Figure 3.15 shows the profiles $o_\perp(z)$ for Decanol and DPPC in the liquid and gel phase, together with the fits to Eq. (3.5). The resulting values are $\lambda_o = 0.15\,\mathrm{nm}$ for Decanol and 0.30 and 0.28 nm for DPPC in the liquid and gel phase, respectively, which is close to the values observed in Table 3.1.

The surface values shown in Fig. 3.16 are also nicely described by the expression using a surface field boundary condition, Eq. (3.6). As discussed in the main text we obtain the ratio (h/a) from these fits and the remaining free parameter a from fluctuations of the octupole density, Eq. (3.19). Correspondingly, we can now predict the pressure due to the octupole orientation in a Landau–Ginzburg model, which is shown in Fig. 3.17. By all practical means the pressure due to octupole orientation is negligible and we expect also higher order terms not to contribute significantly.

Exemplary for symmetric order parameters we now discuss the water quadrupole orientation. In analogy to the main text and the analysis of the octupole density discussed above, we show the quadrupole density $q_\perp(z) = \langle (Q_{zz} - Q_{\mathrm{bulk}})(z)\rho(z)\rangle$ in Figure 3.18, where again we subtract the bulk value $Q_{\mathrm{bulk}} = 1.411 \cdot 10^{-3}\,\mathrm{e\,nm}^2$. The quadrupole density is symmetric with respect to the $z = 0$ plane as $Q_{zz} = \sum_l q_l \Delta z_l^2$. The profiles shown in Fig. 3.18 can excellently be fitted to the symmetric expression Eq. (3.38), where we already used the fact that also in this case the surface field is the relevant boundary condition.

The resulting surface value $q_{\perp 0}$ is shown in Fig. 3.19 and is well described by Eq. (3.39) up to a constant, thus confirming the surface field boundary condition. Again we obtain the last free parameter from the integrated fluctuations of the quadrupole density, Eq. (3.19), which allows to quantitatively evaluate the pressure due to the quadrupole orientation in Fig. 3.20 via Eq. (3.40). The attractive pressure is at least 2-3 orders of magnitude smaller than the repulsive contributions due to polarization that we identified in Fig. 3.8 of the main text. Following our observations for the octupole moment we expect that higher order terms also do not contribute significantly.

Although there exists a variety of symmetric order parameters, the most intuitive candidates such as the second Legendre polynomial of the water orientation or the water tetrahedrality also obey the surface field boundary condition [105] and thus lead to attraction; the amplitude remains to be determined in future studies.

3.5.8. Technical notes

Units

We measure all length scales in nanometers and all energies in units of the thermal energy $k_{\mathrm{B}}T$. The unit of the polarization density $m_\perp$ is $[m_\perp] = \mathrm{e/nm^2}$ and from Eq. (3.1) we then obtain $[a] = \mathrm{nm/e^2}$, $[b] = \mathrm{nm^3/e^2}$ and $[h] = 1/\mathrm{e}$. Finally, the pressure in Eq. (3.8) follows as $[\Pi] = \mathrm{k_BT/nm^3} (= 41.42\,\mathrm{bar}$ at 300 K).

Binning

We can use the water oxygen as position of the dipole (default choice in GROMACS) as well as e.g. the center of mass (COM) or the center of charge (COC), leading to only slight differences in the obtained profiles $m_\perp(z)$ inside the polar headgroup region. For consistency with the standard analysis in GROMACS we use the oxygen position in the present analysis. The different values at the surface $m_{\perp 0}$ obtained from the different binning methods would lead to pressures which are not more than 1.5-2 times different (nearly negligible in the log scale).

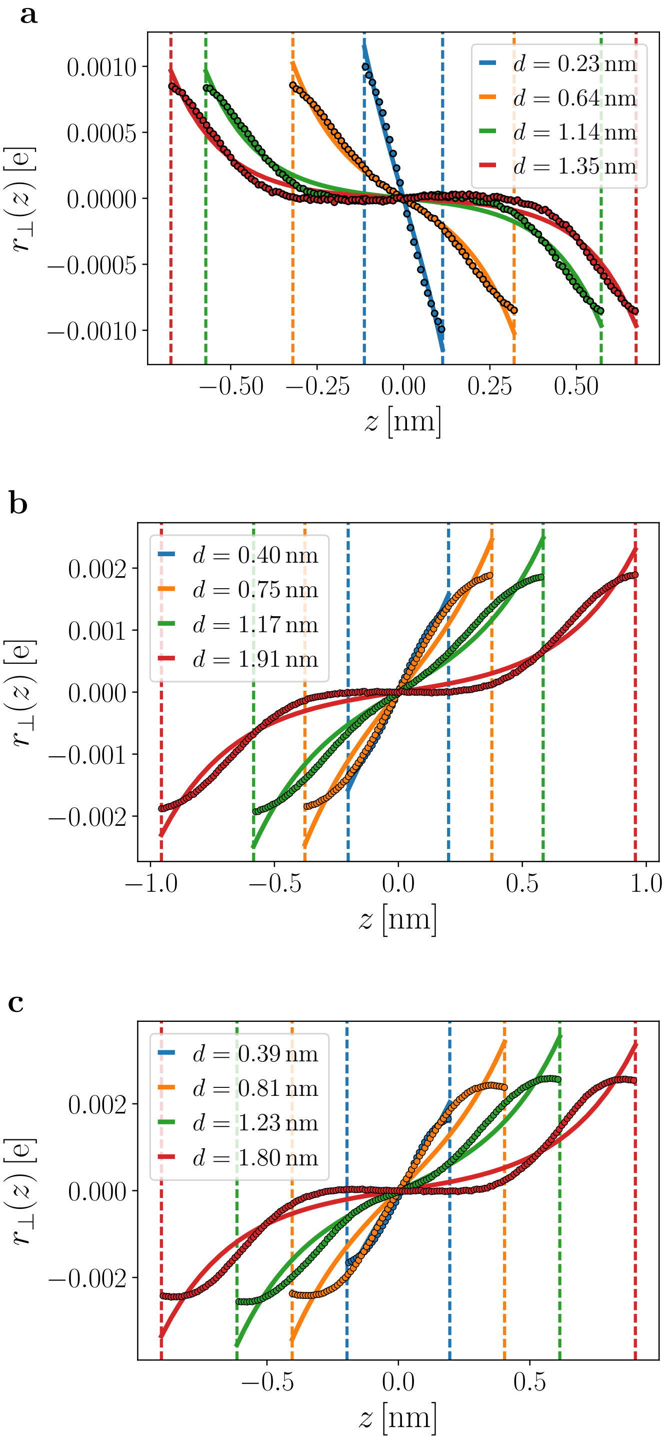

Figure 3.15.: **Octupole density profiles.** (a) Decanol, (b) DPPC in the liquid state, (c) DPPC in the gel phase.

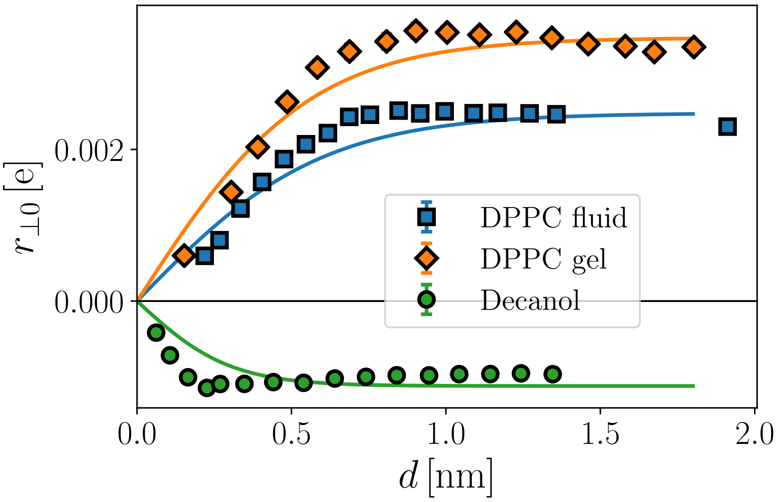

Figure 3.16.: **Octupole orientation at the surface.** for Decanol (green), DPPC in the liquid state (blue), DPPC in the gel phase (orange). Lines denote fits to Eq. (3.6).

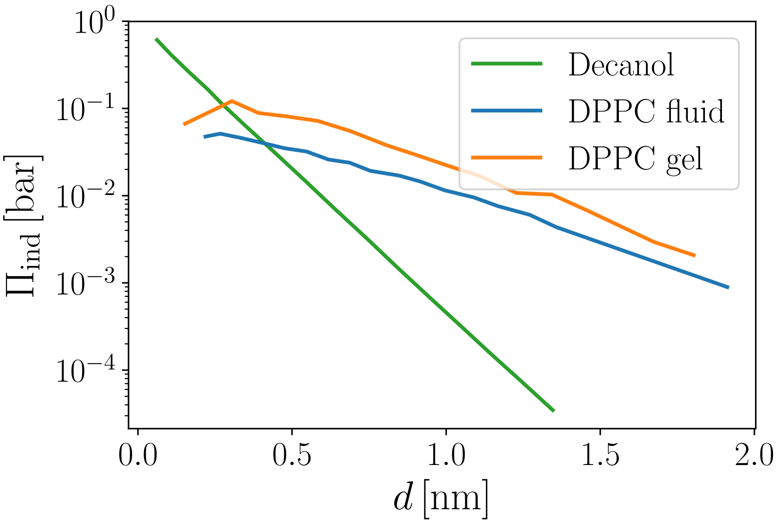

Figure 3.17.: **Landau–Ginzburg pressure due to water octupole orientation.** The distance-dependent prefactor a has been obtained from the fluctuations of the octupole density via Eq. (3.19).

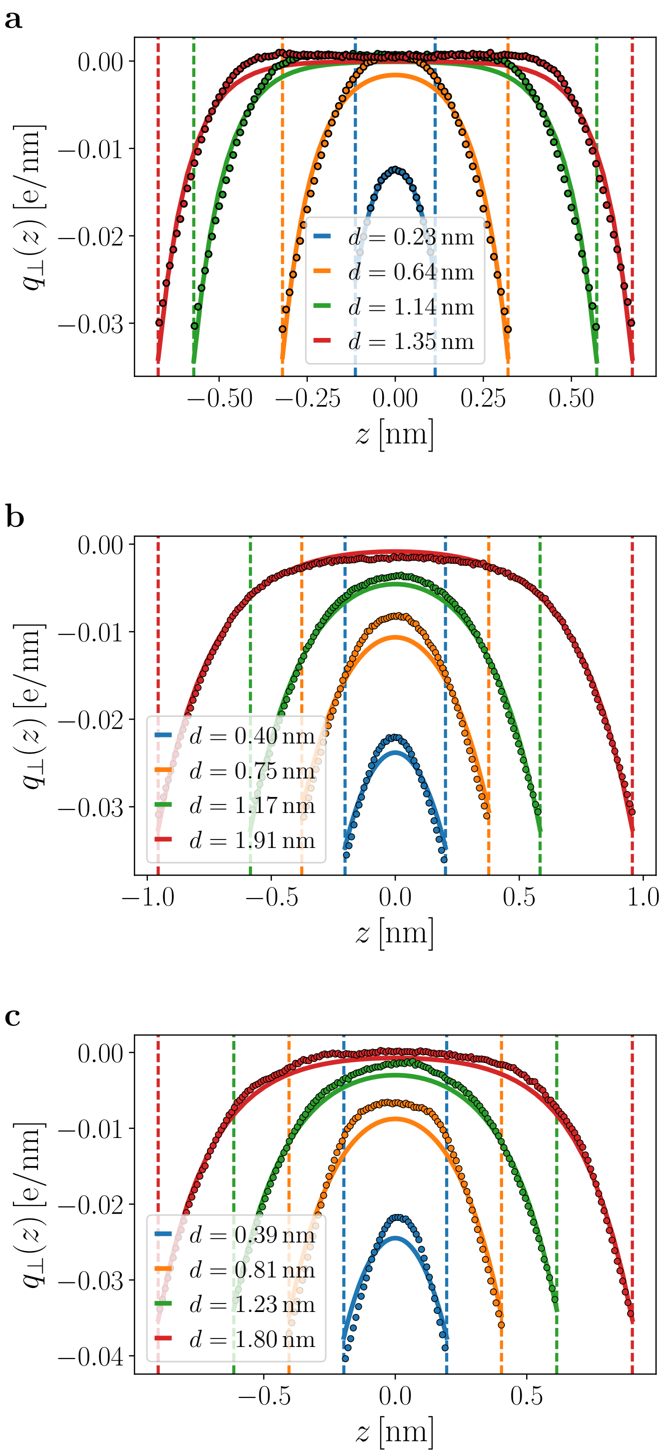

Figure 3.18.: **Quadrupole density profiles.** (a) Decanol, (b) DPPC in the liquid state, (c) DPPC in the gel phase.

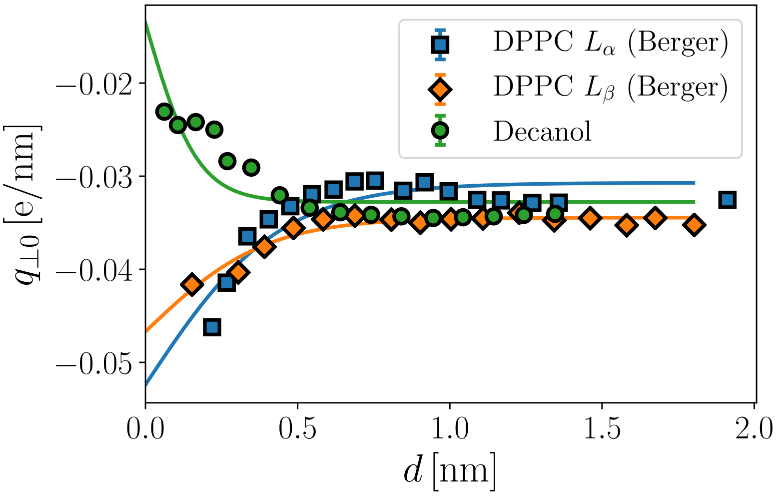

Figure 3.19.: **Quadrupole orientation at the surface**. for Decanol (green), DPPC in the liquid state (blue), DPPC in the gel phase (orange). Lines denote fits to Eq. (3.6).

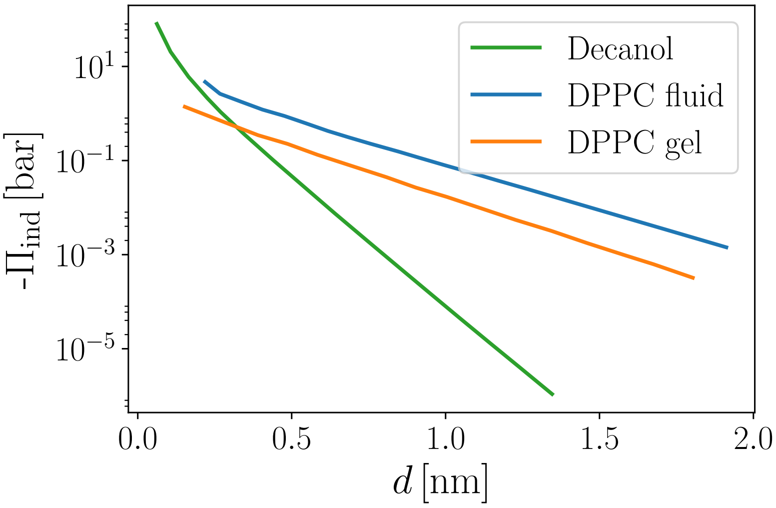

Figure 3.20.: **Negative Landau–Ginzburg pressure due to water quadrupole orientation.** The distance-dependent prefactor a has been obtained from the fluctuations of the quadrupole density via Eq. (3.19)

4. Counterions in aqueous planar confinement: Simulations and electrostatic continuum models

Bibliographic information: The content of this chapter is in preparation to be submitted to a peer-reviewed journal (Ref. [v]).

4.1. Introduction

Most biologically or industrial relevant surfaces become effectively charged in contact with water, where prominent examples range from charged phospholipids in cell membranes [59–61] over monolayers of ionic surfactants [5] to solid surfaces such as glass, silica and mica [47, 49, 50, 52]. The description of the interaction between charged surfaces across aqueous electrolyte solutions is one of the fundamental problems in colloid science. Within the *weak-coupling* limit, the ion distribution at charged interfaces results in the Poisson–Boltzmann (PB) theory [174] and has been analyzed more than 100 years ago [68, 69]. Within the validity of the PB theory, i.e., when the surface charge as well as the ion valency are low, correlations between the ions can be neglected and the resulting interaction pressure for similarly charged walls is always repulsive. On the other hand, if the correlations between ions dominate, similarly charged walls can attract within the *strong-coupling* (SC) regime [71, 175], i.e., in the case of high surface charge or high ion valency, in strong contrast to the mean-field prediction of the PB theory.

If the interaction between surfaces in aqueous solution is considered at nanometer separations, the atomistic structure of water needs to be considered explicitly. Correspondingly, the water–surface interaction, which can be quantified in terms of the contact angle, is crucial for the total interaction [176]. Soft hydrophilic surfaces, as used in our study, typically exhibit an exponentially decaying repulsive interaction across water [51, 53, 54, 86]. The hydration repulsion universally acts between sufficiently polar hydrated surfaces with a characteristic decay length of a fraction of a nanometer [47, 53, 86]. The interplay of repulsive hydration forces and attractive/repulsive electrostatic forces is also found experimentally in the swelling of lamellar systems [74, 177, 178] and line with simulations on a dielectric continuum level [179]. The additivity of hydration and electrostatic interactions has been proposed in experiments from analysis of diffraction data of charged and uncharged lipids [72], however, the interpretation of experimental results is subtle as fits to theory are ambiguous because neither the exact surface charge nor its location are known [73]. Simulations can be designed to sidestep these pitfalls, as surface charge and its location can straightforwardly be imposed. On a nanometer scale the atomistic structure of water needs to be considered explicitly [96] as dielectric effects at the surface and in confinement become important [44, 156].

Here we study a model system composed of Decanol ($CH_3(CH_2)_9OH$) bilayers on which we impose a smeared out partial charge density. To experimentally study double layer forces, self-assembled monolayers (SAMs) provide a well defined model system [180]. For example,, alkyl chains with different headgroups can be attached on a gold substrate serving as cathode, which allows simultaneous measurement of the double layer force using an AFM tip and the double layer capacitance via the tip serving as anode [180, 181]. Inspired by experimental setups, we use a realistic model surface consisting of Decanol molecules which are fixed on a centered rectangular lattice with an angle of 30°, similar to experiments on gold substrates. The corresponding simulation setup is well studied [125, 156, 176, 182] and we have investigated its dielectric properties in Chapter 2 and in Chapter 3 we have discussed the hydration interactions between such surfaces.

In this work, for the first time we study the interaction between charged surfaces in the presence of neutralizing counterions in water-explicit simulations. To facilitate analysis on a Poisson–Boltzmann level, we do not rely on an accurate chemical description of the surface, but instead artificially put a homogeneous negative partial charge δ on the headgroup atoms of the bilayers, see Fig. 4.1 (b). The electric field in the water slab due to the partial charges thus corresponds to the effect of the gold anode in experimental setups as explained above. Further, by smearing out a surface charge homogeneously over the surface we reduce effects that are due to a discrete charge distribution. The advantage of the explicit surface charge over an applied electric field is that the headgroup structure, which would orient in a field due to its dipole moment, is less affected. In our simulations we neutralize the system by model sodium ions. A promising way to obtain ion parameters for MD simulations is optimization with respect to experimentally accessible thermodynamic quantities such as the solvation free energy and activity coefficients [183], however the ion–surface interaction needs to be determined separately, e.g. via optimization of the surface tension. To avoid specific effects, we use the well established sodium parameters by Smith and Dang [184] for ion–water and ion–ion interactions, which reproduce experimental values for the solvation energy and activity coefficient quite well, and use a repulsive potential for the ion–surface interaction, such that for thick water films a density profile agrees well with the PB expression. The detailed choice of parameters is justified in Section 4.5.1.

By adjusting the water number N_w such that the water chemical potential equals its bulk value, $\mu = \mu_\mathrm{b}$, the interaction pressures can be compared for neutral and charged surfaces. Whereas for the lowest surface charge density the PB pressure is reproduced reasonably well, we observe deviations at higher surface charges that are not captured within the weak nor the strong coupling limits. Ionic density profiles are extracted from the simulations that deviate from the PB model due to the repulsive ion–surface interaction. Considering this, the agreement between the simulated density profiles and the weak and strong coupling expressions, where applicable, down to about 0.6 - 0.7 nm is plausible. This is in line with our analysis in Chapter 2, where a box model for the dielectric profiles shows that the effective water dielectric constant is bulk-like down to about 0.7 nm. Yet, this argument does not include dielectric interfacial effects [185], however, also the effective repulsive potential between ions and surface needs to be considered, as we discuss below.

4.2. Atomistic model

The atomistic simulation of two charged planar interfaces with explicit water is subtle due to two characteristic lengthscales which need to be considered:

i) The Bjerrum length $\ell_B = q^2e^2/(4\pi\varepsilon_0\varepsilon k_\mathrm{B}T)$:

   ℓ_B is the characteristic lengthscale at which the interaction between two ions of valency q equals the thermal energy $k_\mathrm{B}T$. ε_0 is the vacuum dielectric permittivity and ε the relative permittivity of water, for which we use the value of the SPC/E water model, $\varepsilon_\mathrm{bulk} = 70$ [156], and thus $\ell_B = 0.8\,\mathrm{nm}$, close to the experimental value $\varepsilon_\mathrm{bulk} = 80$ resulting in $\ell_B = 0.7\,\mathrm{nm}$.

ii) The Gouy–Chapman length $b = \frac{1}{2\pi\ell_B\sigma q}$:

   b measures the distance from the wall with surface charge density σ at which the potential energy of an isolated ion equals thermal energy $k_\mathrm{B}T$. At low surface charge, or equivalently at small separations $d \ll b$, the PB pressure essentially is due to the entropy of an ideal gas of counterions needed to neutralize the system.

iii) The coupling constant $\Xi = q^2\ell_B/b$:

   The ratio of the latter lengthscales determines the range of applicability of the PB equation. The PB theory is roughly valid for coupling parameters $\Xi < 1$ [175]. Correspondingly, for comparing the simulation results for monovalent counterions with the PB theory, small values $b < 1\,\mathrm{nm}$ are problematic. Note that this corresponds to surface charge densities $\sigma > 0.2\,\mathrm{nm}$, which is easily exceeded both in experiments and simulations.

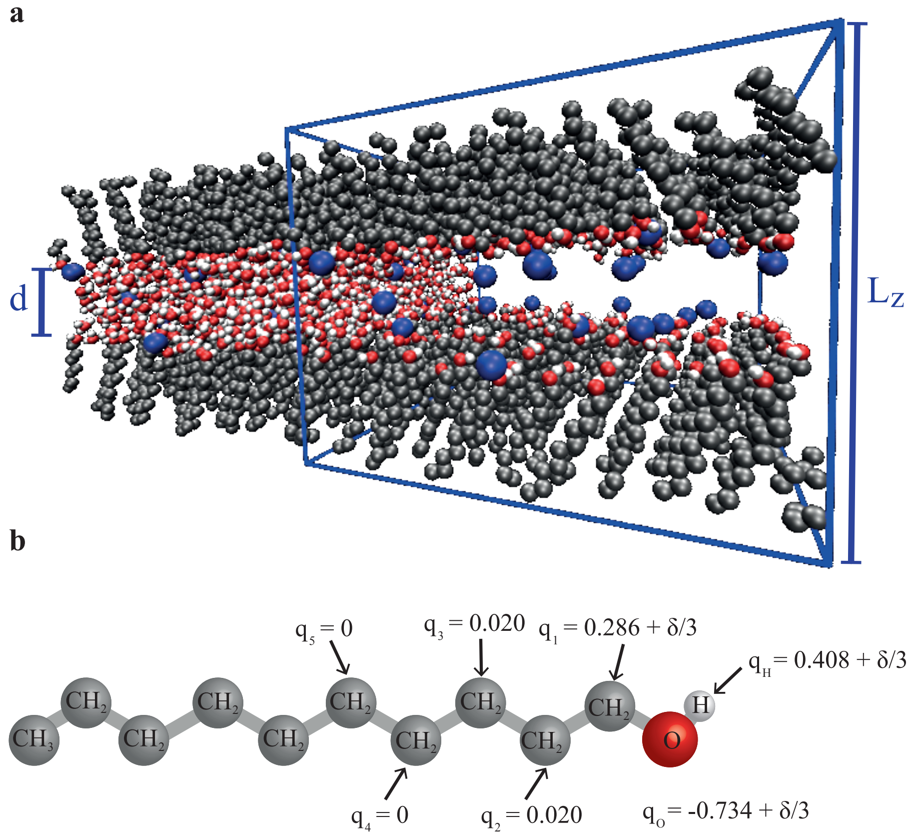

Figure 4.1.: **System setup:** (a) Simulation snapshot of the charged bilayer system with counter-ions. Water molecules are not shown in the central simulation box for clarity. (b) Atomistic model of Decanol with distribution of the partial charges on the polar headgroups (in units of elementary charges). To charge the surface a fractional charge δ is distributed over the headgroup.

Another issue worth mentioning is the finite number of counter-ions in the simulation box, leading to problematic sampling especially at low surface charge densities. Increasing the lateral area improves sampling but slows down the simulations. Our strategy therefore is as follows: First, we determine the pressure versus distance curve for the neutral but polar Decanol bilayers across water for two different lateral areas, namely $A_\mathrm{A} = 4.83 \times 4.83\,\mathrm{nm}^2$ and $A_\mathrm{B} = 6.77 \times 6.77\,\mathrm{nm}^2$. To obtain reasonable values for the interaction pressure in simulations, the water chemical potential μ must be controlled upon bringing the surfaces together. We thus perform simulations in the $N_\mathrm{w}AL_zT$ ensemble at constant temperature $T = 300\,\mathrm{K}$, where we adjust the water number N_w for a given box length L_z such that the chemical potential μ of water equals the value in bulk μ_b. Using the two different lateral box sizes we also make sure that our simulations are not subject to finite size effects. The extrapolation of the chemical potential employs at least three sets of simulations at fixed box height L_z with different water numbers numbers N_{w}. We use 18 simulations along the free energy perturbation reaction coordinate to obtain the chemical potential $\mu(N_{\mathrm{w}})$ using the MBAR method [161]. Each individual trajectory has a length of 100 ns, thus the total sampling time per data point in the pressure–distance curve for Decanol is about 6 μs.

4.2.1. Simulation details

In Figure 4.1 (a) we show a snapshot of a simulation system consisting of $N_{\mathrm{l}} = 10 \times 10$ Decanol molecules (referred to as system A). Force-field parameters are based on GROMOS53A6 [92] where the Decanol hydroxyl groups are represented in atomistic detail, CH_2 and CH_3 groups as united atoms. The repulsion between headgroup oxygens is increased to reduce intra-surface hydrogen bonding [125] and for water the SPC/E model is employed [91]. To avoid slow reorientation events, we restrain all Decanol molecules on the second CH_2 group counting from the OH headgroup with force constants $k_x = k_y = 500\,\mathrm{kJ/(mol\,nm^2)}$ and $k_z = 10\,\mathrm{kJ/(mol\,nm^2)}$ and the terminal CH_3 group with $k_x = k_y = 5\,\mathrm{kJ/(mol\,nm^2)}$ on a centered rectangular lattice with a lateral area per headgroup of $A/N_{\mathrm{l}} = 0.234\,\mathrm{nm}^2$. This corresponds to the tensionless state in vacuum of the uncharged surface with a Decanol tilt angle of 30°. To ensure an integer number of counterions and in order to exclude finite size effects some simulations are also performed at larger lateral area using $N_{\mathrm{l}} = 14 \times 14$ molecules (System B).

All simulations are performed using version 5.0 of the GROMACS simulation package [126] at $T = 300\,\mathrm{K}$ with periodic boundary conditions. Lennard–Jones (LJ) interactions are truncated at $r_{\mathrm{c}} = 0.9\,\mathrm{nm}$, for the electrostatic interactions the Particle Mesh Ewald method [128] is employed with a real-space cut-off $r_{\mathrm{c}} = 0.9\,\mathrm{nm}$. Figure 4.1 (b) shows the united atom representation of a Decanol and the corresponding charge distribution of the COH-headgroup. In order to charge the surfaces homogeneously we add a partial charge δ to the three COH headgroup atoms as indicated in Fig. 4.1 (b). Table 4.1 summarizes the simulation parameters for the systems considered in this study, where we use the bulk dielectric constant $\varepsilon_{\mathrm{bulk}} = 70$ of the SPC/E water model [156], which enters linearly in the Gouy–Chapman length b and inverse quadratically into the coupling parameter Ξ.

4.2.2. Location of the surface charge in continuum model

When comparing ion- and water-explicit simulations with a continuum model the question of where the surface charge is located naturally arises. The unambiguous thermodynamic surface position is given by the Gibbs Dividing Surface (GDS), which we define in analogy

	$A\,[\mathrm{nm}^2]$	$\sigma\,[\mathrm{e/nm}^2]$	q	N_ion	$b\,[\mathrm{nm}]$	Ξ	$\delta\,[\mathrm{e}]$
A0-0	4.83×4.83	0	0	0	-	0	0
B0-0	6.77×6.77	0	0	0	-	0	0
A1-1	4.83×4.83	-0.096	0.25	18	8.31	0.01	0.0225
A1-2	4.83×4.83	-0.096	0.5	9	4.15	0.05	0.0225
B1-3	6.77×6.77	-0.109	1.0	10	1.83	0.43	0.0255
A3-3	4.83×4.83	-0.385	1.0	18	0.52	1.53	0.09
A4-3	4.83×4.83	-0.770	1.0	36	0.25	3.06	0.18
A5-3	4.83×4.83	-1.541	1.0	72	0.06	6.13	0.36

Table 4.1.: **Simulation parameters for the neutral and charged surfaces.** A and B denotes the systems with different lateral areas. The corresponding values have been calculated using the SPC/E bulk dielectric constant $\varepsilon_\mathrm{bulk} = 70$.

to experiments [53] via the water layer thickness d_w using the bulk molecular water volume $v_\mathrm{w}^\mathrm{b} = 0.0304\,\mathrm{nm}^3$ and the number of water molecules N_w as $d_\mathrm{w} = N_\mathrm{w} v_\mathrm{w}^\mathrm{b}/A$. However, in a continuum-model of electrostatic interactions it is the location of the surface charge that enters. In analogy to our previous work [125] (also see Chapter 3), to compare with the continuum models we define the surface separation $d = d_\mathrm{s} - d_\mathrm{s}^0$ based on the structural separation d_s, which is defined as the mean distance between the oxygen atoms of the opposing layers for Decanol, illustrated in Fig. 4.2 (a). This definition of d_s is equal to the mean distance of the excess surface charge δ that we distribute on the headgroup atoms, see Fig. 4.2 (d). As at zero water content the surfaces are in contact, which in a continuum model corresponds to zero separation, we subtract the equilibrium separation at zero water content to obtain the effective surface separation $d = d_\mathrm{s} - d_\mathrm{s}^0$, see Fig. 4.2 (b).

In Figure 4.2 (c) we show the Decanol charge density profile (black line), which reveals a pronounced orientation of the headgroups with respect to the surface normal. Upon bringing the excess charge δ to the headgroup atoms, the resulting charge density profile is only slightly affected for low values $\delta = 0.03$ (blue line in Fig. 4.2 (c)), but becomes highly asymmetric for high surfaces charges $\delta = 0.18$, shown as red line in Fig. 4.2 (c). Figure 4.2 (d) shows the profiles of the excess charge δ for the $\delta = 0.03$ (blue line) and $\delta = 0.18$ (red line). The shape and position of the maxima follow the oxygen mass density profiles shown in Fig. 4.2 (a), as indicated by the dashed vertical lines, thus justifying the identification of d with the position of the charged wall in an electrostatic model.

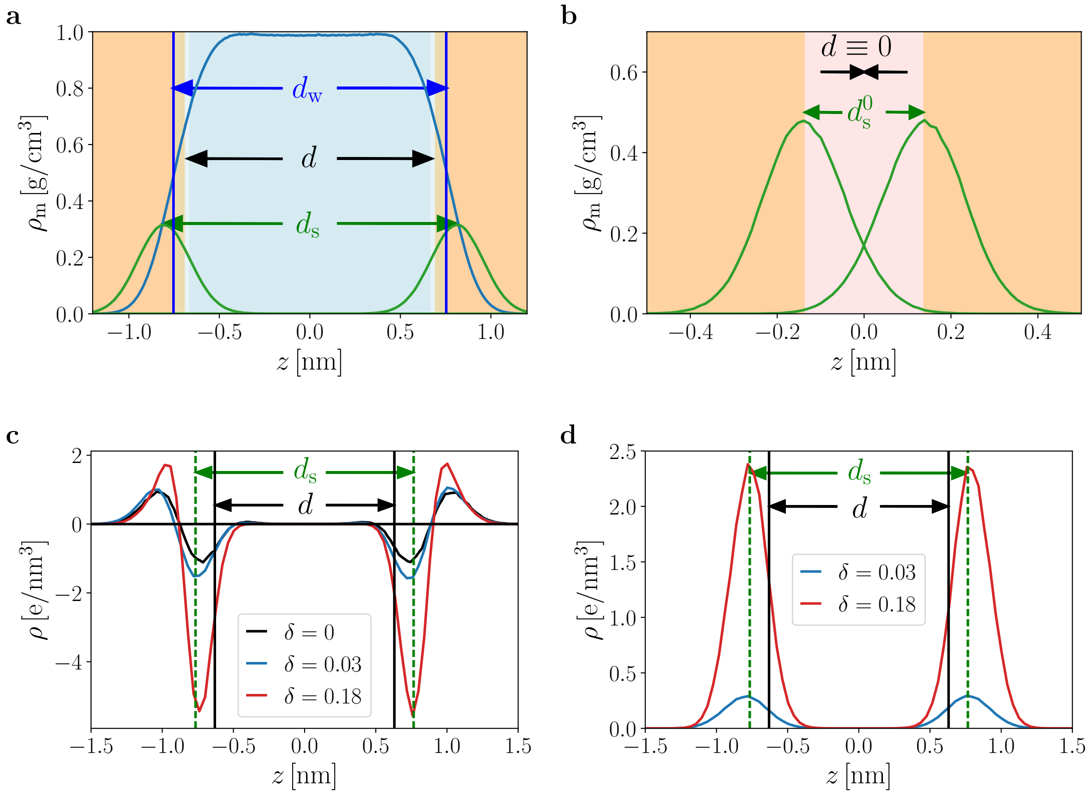

Figure 4.2.: **Location of the surface charge and definition of the separation d.** (a) Mass density ρ_m of water (blue line) and oxygen (green line) for the Decanol system at a water slab thickness $d_\mathrm{w} = 1.5\,\mathrm{nm}$. Horizontal blue lines indicate the Gibbs Dividing surface positions, which define d_w, the light blue shaded area denotes the distance d, which follows from the difference between the headgroup separation d_s and the value at zero water content $N_\mathrm{w} = 0$, shown in (b). (c) Decanol charge density of the neutral system (black line) and at low ($\delta = 0.03$, blue line) and high ($\delta = 0.18$, red line) surface charge. Solid vertical line indicates the surface position d, dashed green line the structural separation d_s. In (d) the excess charge distribution δ on the three headgroup atoms is shown.

4.3. Results

4.3.1. Neutral surfaces

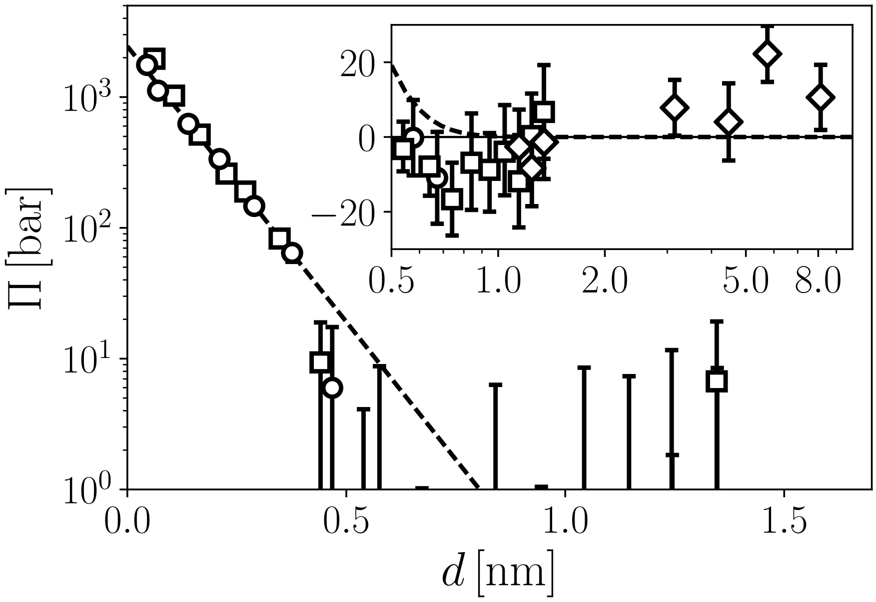

Figure 4.3.: **Interaction pressure of the neutral but polar Decanol surfaces.** Data is shown for lateral dimensions of 4.83 nm × 4.83 nm (squares, A0-0) and 6.77 nm × 6.77 nm (circles, B0-0). Diamonds denote simulations in the $N_\mathrm{w}A\Pi_0T$ ensemble at $\Pi_0 = 1\,\mathrm{bar}$, where we show the equivalent osmotic pressure, Eq. (4.2). The inset zooms into the large distance regime where the pressures are zero within numerical accuracy, the dashed line denotes an logarithmic fit of Eq. (4.1) to all positive simulation data yielding a decay length $\lambda = 0.10\,\mathrm{nm}$.

In Figure 4.3 we show the interaction pressure of the neutral but polar Decanol surfaces at bulk water chemical potential for the two lateral areas considered in this study, $A_\mathrm{A} = 4.83\,\mathrm{nm} \times 4.83\,\mathrm{nm}$ (shown as squares in Fig. 4.3) and $A_\mathrm{B} = 6.77\,\mathrm{nm} \times 6.77\,\mathrm{nm}$ (shown as circles in Fig. 4.3), corresponding to 10×10 and 14×14 Decanol molecules per monolayer. The repulsive pressure decays exponentially with increasing separation,

$$\Pi_\mathrm{hyd} = \Pi^\star \mathrm{e}^{-d/\lambda}, \tag{4.1}$$

with a characteristic length of $\lambda = 0.10\,\mathrm{nm}$ obtained from a logarithmic fit to all positive simulation data, shown as dashed line in Fig. 4.3. The subscript "hyd" indicates that we will refer to this as hydration pressure in the following. The extrapolated pressure at contact is $\Pi^\star \approx 2.5\,\mathrm{kbar}$. At distances larger than about 0.5 nm the interaction is zero within our measurement accuracy, as seen in the inset of Fig. 4.3. The simulation data suggest that there might be a slight minimum around 1 nm which can not be explained by vdW forces, see Section 4.5.2, and which deviates from the exponential behavior. As the obtained pressures for $d > 0.5\,\mathrm{nm}$ scatter around $0 \pm 20\,\mathrm{bar}$, which is in the order of the pressure resolution we can achieve, we do not discuss this further. In addition to these simulations, which are performed in the $N_\mathrm{w}AL_zT$ ensemble with the water number N_w determined such that the chemical potential of water equals bulk, $\mu = \mu_\mathrm{b}$, we include data at large separations from simulations using the $N_\mathrm{w}A\Pi_0T$ ensemble at normal pressures of $\Pi_0 = 1$ bar. In that case we measure the chemical potential $\mu(N_\mathrm{w})$ and analogous to experiments convert this to equivalent osmotic pressures,

$$\Pi(N_\mathrm{w}) = \Pi_0 + \frac{\mu_\mathrm{b} - \mu}{v_\mathrm{w}^\mathrm{b}}, \tag{4.2}$$

where $v_\mathrm{w}^\mathrm{b} = 0.0304\,\mathrm{nm}$ denotes the simulated molecular volume of water in bulk at 1 bar pressure. Equation (4.2) follows from the formally exact thermodynamic Gibbs–Duhem equation as shown in Appendix A.1. Note that for the simulations in the $N_\mathrm{w}AL_zT$ ensemble we subtract the internal stress that acts on the hydrated surface at large separations due to the positional constraints (as the restraint energy is included in the virial). This value has been determined by rerunning simulation trajectories at large d with the restraint potentials turned off, resulting in a pressure difference of $\Delta\Pi = +16\,\mathrm{bar}$, see Appendix A.4. For simulations in the $N_\mathrm{w}A\Pi_0T$ ensemble the barostat adjusts the box length correspondingly, such that the interaction pressure equals the one obtained from the virial. The obtained interaction pressures agree quantitatively, which justifies our method.

4.3.2. Ion density profiles

Having assessed the interaction of the neutral Decanol surfaces across water, which reveals an exponential repulsion that dominates at small separations, we now turn to the analysis of the charged surfaces with the corresponding amount of counterions added to neutralize the system, see Fig. 4.1.

In Figure 4.4 (a) we show the charge density profile at large separations $d = 4.09\,\mathrm{nm}$ for surface charge $\sigma = -0.11\,\mathrm{e/nm}^2$ and $d = 5.68\,\mathrm{nm}$ for the higher surface charges. In order to compare the data for different surface charges simultaneously in Fig. 4.4 (a), we rescale the densities according to $\tilde{\rho} = \rho/2\pi\ell_\mathrm{B}\sigma^2$. In the slab center, the density profiles agree well with the PB predictions, shown as dashed lines in Fig. 4.4 (a), for $\sigma < 0.7\,\mathrm{e/nm}^2$. Close to the interface the density drops compared to the PB prediction, which is due repulsive ion–surface interactions. For values $\sigma > 0.7\,\mathrm{e/nm}^2$, the profiles deviate significantly, which

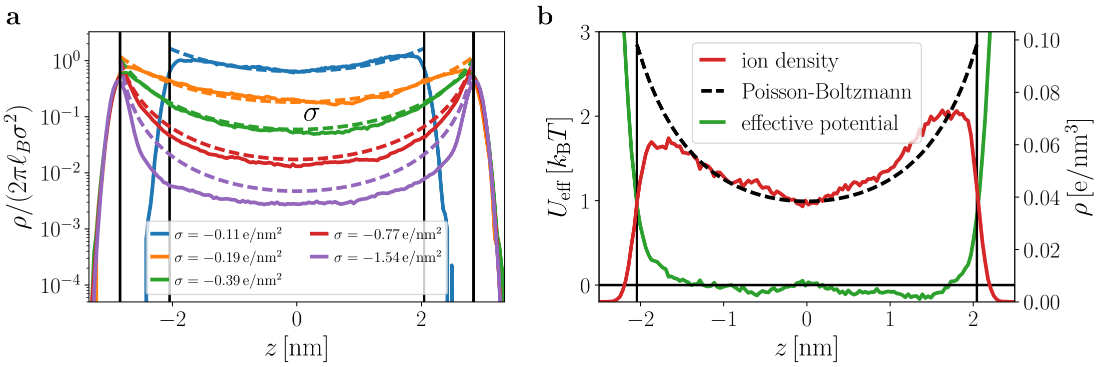

Figure 4.4.: **Ion densities at large separation.** (a) Rescaled ion densities $\tilde{\rho}$ for increasing surface charge density σ, indicated by the black arrow. Dashed lines show the expected density profile from PB theory, solid lines denote simulation results. Vertical black lines denote the surface separation, which is $d = 4.09\,\mathrm{nm}$ for $\sigma = -0.11\,\mathrm{e/nm^2}$ and $d = 5.68\,\mathrm{nm}$ for the other systems. (b) Ion density for $\sigma = -0.11\,\mathrm{e/nm^2}$ at $d = 4.09\,\mathrm{nm}$ (solid red line, right axis) and the corresponding PB density (dashed black line). Green line denotes the effective ion–surface potential according to Eq. (4.3) (left scale).

is expected as the corresponding coupling parameters $\Xi = 3$ (red line in Fig. 4.4 (a)) and $\Xi = 6$ (lilac line Fig. 4.4 (a)) are significantly larger than 1.

To quantify the the difference between the observed density ρ in the simulation and the PB density ρ_PB, we compute the effective potential U_eff according to

$$U_\mathrm{eff} = -\log\left(\frac{\rho}{\rho_\mathrm{PB}}\right). \tag{4.3}$$

Note that in order to predict ion profiles from a potential of mean force (PMF), one follows the opposite approach and incorporates the PMF into the PB equation [76, 186]. The additivity assumption on the surface potentials has significant influence on the resulting interaction at small separations (Ref. [x]), thus we analyze the lowest surface charge density $\sigma = -0.11\,\mathrm{e/nm^2}$ considered in this work at separation $d = 4.09\,\mathrm{nm}$ in Fig. 4.4 (b). The simulated density profile (red line in Fig. 4.4 (b), right scale) indicates that the employed simulation time of 100 ns is not sufficient to obtain converged density profiles. The effective potential can be converted into a box profile, which enables to solve the PB equation for counterions in a similar approach as in [76] and Ref. [x]. The use of box profiles has been proven to be successful for modeling interfacial capacitance effects including the dielectric profile [185]. This modeling approach is work in collaboration with Dr. Yuki Uematsu and shall be completed after submission of this thesis.

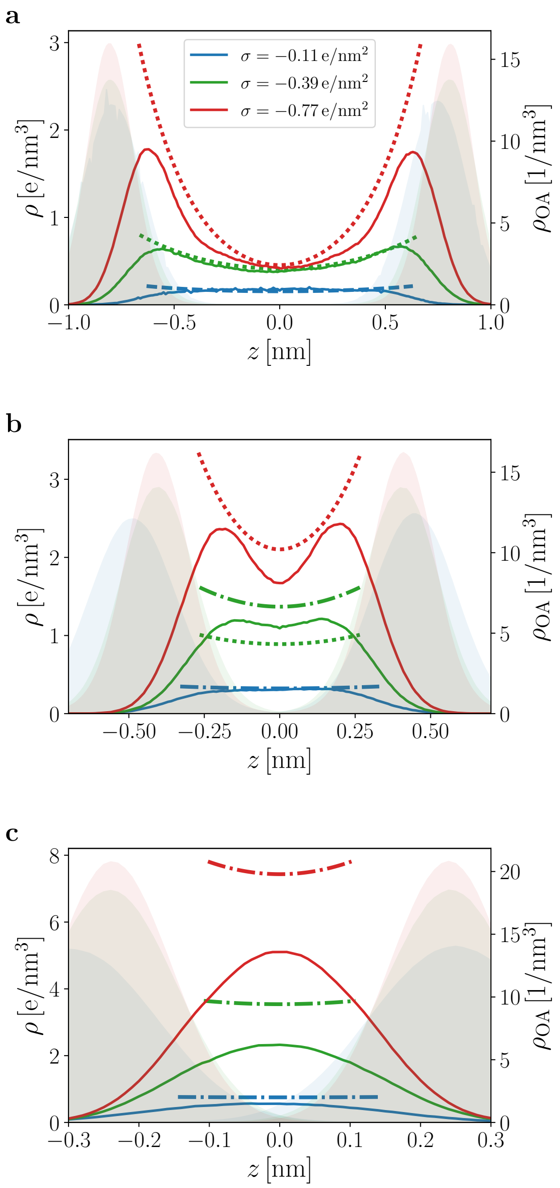

Figure 4.5.: **Ion and headgroup density profiles.** (a) Weak confinement $d \approx 1.5\,\mathrm{nm}$, (b) intermediate confinement $d \approx 0.8\,\mathrm{nm}$ and (c) strong confinement $d \approx 0.4\,\mathrm{nm}$. Colors decode the different surface charge densities, solid lines denote simulation results for the ion density. Shaded areas denote the density of the Decanol oxygen. Broken lines show the corresponding continuum predictions where applicable, see Table 4.2: PB Eq. (4.32) as dashed line in (a), the sum of two single charged plates in the SC limit Eq. (4.4) as dotted lines (a) and (b) and the SC expression up to next leading order in Ξ, Eq. (4.6), as dash-dotted lines.

To elaborate the effects of confinement, we show exemplary ion and headgroup density profiles for different surface charge densities in Fig. 4.5, including weak confinement ($d \approx 1.5\,\mathrm{nm}$, corresponding to $N_\mathrm{w}/N_\mathrm{l} \approx 6$ waters per Decanol) in Fig. 4.5 (a), at intermediate values ($d \approx 0.8\,\mathrm{nm}$, $N_\mathrm{w}/N_\mathrm{l} \approx 3$) in Fig. 4.5 (b), and in strong confinement ($d \approx 0.4\,\mathrm{nm}$, $N_\mathrm{w}/N_\mathrm{l} \approx 1.7$) in Fig. 4.5 (c). The weak coupling limit of the PB theory is expected to hold in the range $a_\perp < b < d$, where $a_\perp = b\sqrt{\Xi}$ denotes the lateral distance between the counter-ions [70]. For the three monovalent systems considered in this work, this only holds for B1-3 with $\sigma = -0.11\,\mathrm{e/nm^2}$ and $d > 1.8\,\mathrm{nm}$.

For $b < a_\perp < d$, neither the PB nor the SC descriptions hold. In a rough approach, the counterion layers decouple and the density profiles of each layer are well described by the exponential SC profiles for a single charged plate [70],

$$\tilde{\rho}_\mathrm{SC}(z) = \mathrm{e}^{(d/2-z)/b} + \mathrm{e}^{(z-d/2)/b}. \tag{4.4}$$

This approximation is included in Fig. 4.5 (a) and (b) as dotted line, as the validity of Eq. (4.4) corresponds to $d > 0.8\,\mathrm{nm}$ for $\sigma = -0.39\,\mathrm{e/nm^2}$ (A3-3) and $d > 0.6\,\mathrm{nm}$ for $\sigma = -0.77\,\mathrm{e/nm^2}$ (A4-3), respectively.

Within the strong coupling limit $\Xi \to \infty$ the density profile between the charged walls is constant and follows in reduced units $\tilde{\rho} = \rho/(2\pi\ell_\mathrm{B}\sigma^2)$ as

$$\tilde{\rho}_\mathrm{SC}(\tilde{z}) = \frac{2}{\tilde{d}}. \tag{4.5}$$

The leading correction to the SC limit follows from a virial expansion of the partition sum and can be approximated in closed form [70], such that the density profile follows as

$$\tilde{\rho}^{(1)}_\mathrm{SC}(\tilde{z}) = \frac{2}{\tilde{d}}\left[1 + \frac{1}{\Xi}\left(\tilde{z} - \frac{\tilde{d}}{2}\right)^2 - \frac{\tilde{d}^2}{12}\right] + \mathcal{O}(\Xi^{-2}), \tag{4.6}$$

where $\tilde{z} = z/b$ and $\tilde{d} = d/b$ denote the dimensionless position and distance, respectively. The corresponding density profiles from Eq. (4.6) are included in Fig. 4.5 (b) and (c) as dash-dotted lines. We have used the theoretical expression that we expect to describe the data at the given parameters best in Fig. 4.5, merely the system with $\sigma = -0.39\,\mathrm{e/nm^2}$ at $d \approx 0.8\,\mathrm{nm}$ is exactly in between the validity of Eq. (4.4) and Eq. (4.6). We thus include both expressions as dotted and dash-dotted green lines in Fig. 4.5.

For $1.52\,\mathrm{nm} < d < 1.83\,\mathrm{nm}$ at the lowest surface charge $\sigma = -0.11\,\mathrm{e/nm^2}$, the ions form a three-dimensional gas of counterions, in which case the Poisson–Boltzmann description is expected to work on leading level [70]. We therefore include the PB density profile in

	$a_\perp$ [nm]	b [nm]	
B1-3	1.52	1.83	PB for $d > 1.83\,\mathrm{nm}$ $1.52\,\mathrm{nm} < d < 1.83\,\mathrm{nm}$: counter-ion gas SC (two plates) for $d < 1.52\,\mathrm{nm}$
A3-3	0.81	0.52	SC (decoupled plates) for $d > 0.81\,\mathrm{nm}$ SC (two plates) for $d < 0.81\,\mathrm{nm}$
A4-3	0.57	0.26	SC (decoupled plates) for $d > 0.57\,\mathrm{nm}$ SC (two plates) for $d < 0.57\,\mathrm{nm}$

Table 4.2.: **Expected range of validity of the PB and SC expressions.**

this case as dashed line in Fig. 4.5 (a) . The expected range of validity of the strong and weak coupling limits is summarized in Table 4.2.

Considering the fact that the effect of a surface potential is not included in any of the models discussed here, the disagreement between the simulations and the calculated density profiles is plausible. At larger separations in Fig. 4.5 (a), the repulsion between the ions and the smeared out headgroups at the interfaces leads to deviations from the models. This effect of finite ion size becomes more pronounced at stronger confinement Fig. 4.5 (b), and leads to an inverted density profile at even smaller separations, Fig. 4.5 (c), which is dominated by the exclusion of ions from the headgroups. To strengthen this statement we show as shaded areas in Fig. 4.5 the headgroup oxygen number density ρ_{OA} (right scale). Whereas for $d \approx 1.5\,\mathrm{nm}$ the oxygen density profiles do not overlap in the slab center, the oxygen densities are finite at $z = 0$ for $d \approx 0.8\,\mathrm{nm}$ and show a strong overlap in strong confinement, $d \approx 0.4\,\mathrm{nm}$.

4.3.3. Interaction pressures

In Figure 4.6 we show the interaction pressures obtained from our water-explicit simulations at bulk water chemical potential. The pressure versus distance curve for the system with the smallest coupling parameter $\Xi = 0.43$ ($\sigma = -0.11\,\mathrm{e/nm^2}$) is show in Fig. 4.6 (a) and compared to the data for the interaction between the uncharged surface without ions, Fig. 4.3. We also include the sum of the hydration and PB pressures, $\Pi_{\mathrm{hyd}} + \Pi_{\mathrm{PB}}$ as solid lines in Fig. 4.6. For small separations, the simulation data for the charged and uncharged system are very similar and both show an exponential decay with approximately the same decay length. At separations $d \approx 0.5\,\mathrm{nm}$, the pressure between the uncharged surfaces is essentially zero (black data in Fig. 4.6), but the blue data in Fig. 4.6 (a) remains significantly positive even at large separation. Remarkably, the data in this case agrees quantitatively with the PB pressure (solid blue line in Fig. 4.6 (a)).

With increasing charge density, $\sigma = -0.39\,\mathrm{e/nm^2}$ ($\Xi = 1.53$, shown in green in Fig. 4.6

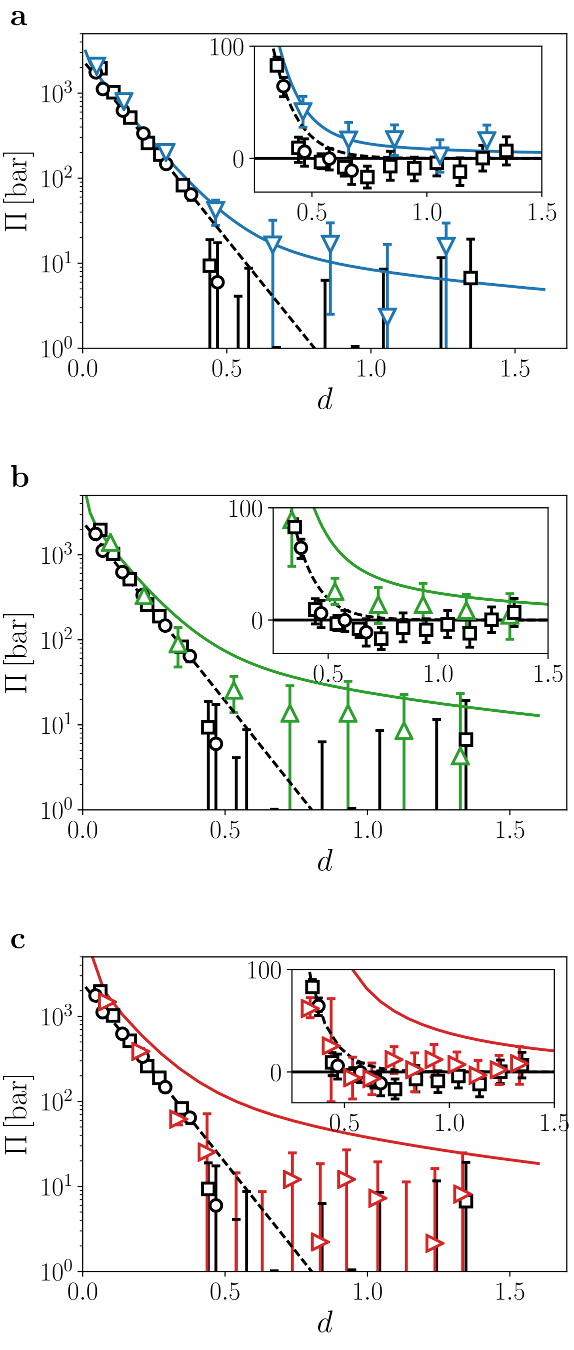

Figure 4.6.: **Interaction pressures between charged surfaces** (colored data). (a) Small coupling parameter $\Xi = 0.43$, corresponding to a surface charge density $\sigma = -0.11\,\mathrm{e/nm^2}$. (b) Intermediate coupling parameter $\Xi = 1.53$, corresponding to a surface charge density $\sigma = -0.385\,\mathrm{e/nm^2}$. (c) Results for $\Xi = 3.06$, corresponding to $\sigma = -0.77\,\mathrm{e/nm^2}$. Black data shows the pressure between the neutral surfaces, dashed line the exponential fit as in Fig. 4.3. Solid lines are sums of the exponential and the PB pressure. Insets show the data on a linear scale.

(b)), the short-range decay is basically indistinguishable from the neutral system (black data). The repulsion at large separations is similar to the lower surface charge density shown in Fig. 4.6 (a), but about a factor two less than expected from adding the exponential hydration and the PB pressure. This trend holds also for the system with the highest surface charge, $\sigma = -0.77\,\mathrm{e/nm^2}$ ($\Xi = 3.06$, red data in Fig. 4.6 (c)). In that case, the decay on short lengthscale is still perfectly on top of the neutral data, but at about $d = 0.6\,\mathrm{nm}$ a minimum in the pressure–distance curve appears. At large separations, the pressure again is about 10 bar, as also observed in Fig. 4.6 (a) and (b), and thus 2-3 times less than expected from PB theory.

Note that PB theory is not necessarily expected to work in these systems, as a number of effects come into play: The water structure at charged surfaces is known to be different from uncharged ones [187], the ion–surface repulsion is not considered, interfacial dielectric effects [129, 185] are not treated on this level and the dielectric constant in charged systems is unknown, just to name a few. Note that an analysis like in Chapter 2 can straightforwardly be conducted for the parallel component by subtracting the monopoles. However, the analysis of the perpendicular profile in a charged system, which is the relevant component for the surface interaction, is technically more involved as it follows in the static limit of the frequency-dependent dielectric permittivity, where ionic currents need to be correctly subtracted [188], and remains subject to future studies. For the neutral surface, the effective perpendicular dielectric constant decreases only for values $d < 0.5\,\mathrm{nm}$, thus deviations to PB can not be explained using this information, as we observe the pressure to be different from that expectation also at large separations. Last, the theoretical models assume counterions confined in a slab, where the walls are treated as semi-infinite half-spaces. Whereas this approximation might be good for certain experimental situations, there are other situations where this is definitely not the case, as for example in a stack of lipid bilayers also the interactions with neighboring slabs needs to be considered. This also goes beyond established methods to treat image charges in continuum models (see e.g. Refs. [189, 190]).

To conclude this section, we subtract the interaction Π_{neut} between the neutral surfaces from the ones charged systems in Fig. 4.7, considering also the apparent minimum in Fig. 4.3, which we fit by a third order polynomial. At the separations which we consider here, the simulated systems are at the edge of validity of the classical PB description, in between PB and SC, and within validity of SC (see Table 4.2 and the corresponding density profiles in Fig. 4.5). We thus employ also Monte Carlo simulations performed with the corresponding continuum model parameters in Table 4.1, and show the corresponding pressures as crosses in Fig. 4.7, see Section 4.5.4 for details on the MC simulations.

In the strong coupling limit, $\Xi \to \infty$, the pressure follows from the contact density in

Eq. (4.5),

$$\tilde{\Pi}_{\mathrm{SC}} = \frac{\Pi_{\mathrm{SC}}}{2\pi\ell_{\mathrm{B}}\sigma^2} = k_{\mathrm{B}}T\left[\frac{2}{\tilde{d}} - 1\right], \tag{4.7}$$

which actually differs by a constant 2/3 in reduced units from the asymptotic PB solution in the limit $d \ll b$, Eq. (4.36),

$$\tilde{\Pi}_{\mathrm{PB}} = \frac{\Pi_{\mathrm{PB}}}{2\pi\ell_B\sigma^2} = k_{\mathrm{B}}T\left[\frac{2}{\tilde{d}} - \frac{1}{3}\right]. \tag{4.8}$$

However, we observe that the density profiles in Fig. 4.5 are not constant, as expected in the SC limit, but rather can be approximated by the SC expression if the finite-coupling corrections are taken into account (dash-dotted lines in Fig. 4.5). Using a virial-expansion scheme, which is obtained as a series expansion in powers of $1/\Xi$ about the asymptotic SC solution $\Xi \to \infty$ [70], the pressure corresponding to Eq. (4.6) then follows as

$$\tilde{\Pi}^{(1)}_{\mathrm{SC}} = \frac{\Pi_{\mathrm{SC}}}{2\pi\ell_{\mathrm{B}}\sigma^2} = k_{\mathrm{B}}T\left[\frac{2}{\tilde{d}} - 1 + \frac{\tilde{d}}{3\Xi}\right] + \mathcal{O}(\Xi^{-2}). \tag{4.9}$$

The virial expansion is expected to break down when the second-leading contribution becomes of the same magnitude as the leading contribution to the density at the plate. Comparing the first two with the last term in Eq. (4.9) reveals that Eq. (4.9) should be roughly valid $\tilde{d} < 1/2(\sqrt{3}\sqrt{3\Xi^2 + 8\Xi} - 3\Xi)$, which yields $d < 2\,\mathrm{nm}$ for $\Xi = 0.43$, $d < 0.8\,\mathrm{nm}$ for $\Xi = 1.53$ and $d < 0.4\,\mathrm{nm}$ for $\Xi = 3.06$. We thus include the pressure Eq. (4.9) in the range of its validity in Fig. 4.7 as dash-dotted lines.

From Eq. (4.9) we can also estimate the range of validity of the SC theory by comparing the first and last terms with each other, which corresponds to the case when the second-leading order of the density at the plate becomes comparable to the leading order. Thus, the strong-coupling theory should be valid only for $\tilde{d} < \sqrt{6\Xi}$, which yields $d < 1.6\,\mathrm{nm}$, 3 nm and 4.3 nm for $\Xi = 0.43$, 1.53 and 3.06, respectively. The corresponding SC expressions Eq. (4.7) are included as dotted lines in Fig. 4.6.

For $\Xi = 0.43$, shown in Fig. 4.6 (a) the next-leading order of SC, Eq. (4.9), and the PB pressure, Eq. (4.34) both quantitatively agree with the results from MC simulations, included as crosses in Fig. 4.6 (a), as is expected in that case as $d < b$, where both limits are dominated by the entropy of an ideal gas of ions. The MD simulations in that case are subject to large statistical uncertainties and agree on separations $d > 0.5\,\mathrm{nm}$, but deviate significantly at smaller separations. In the case of $\Xi = 1.53$, shown in Fig. 4.6 (b), the PB pressures (shown as dotted lines) deviate already significantly from the MC

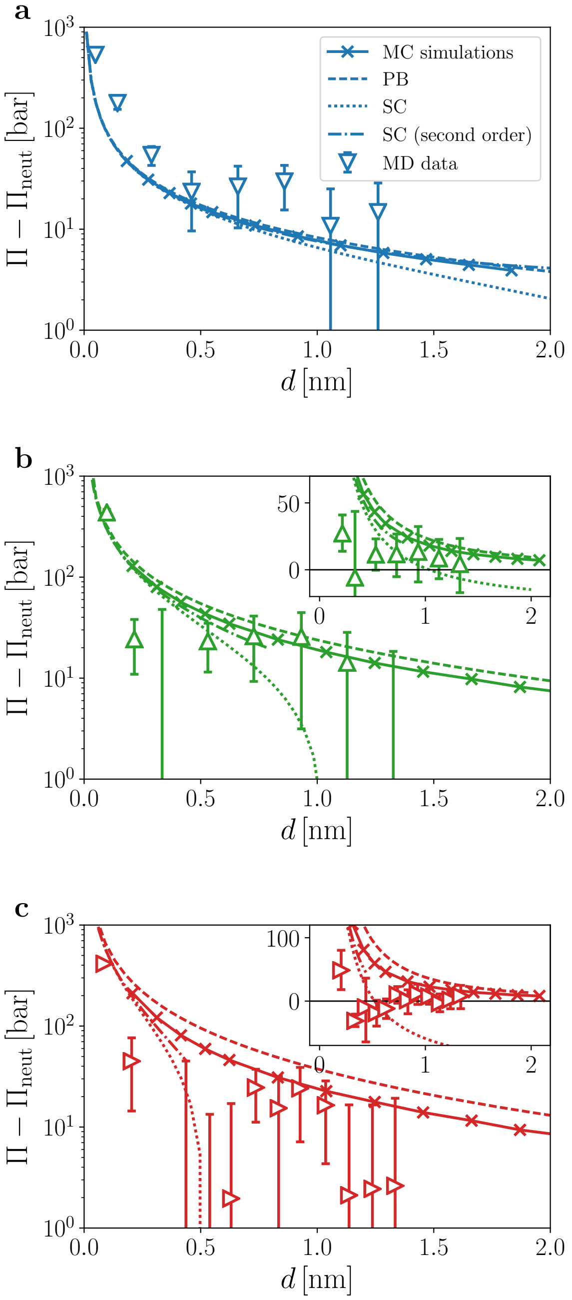

Figure 4.7.: **Excess pressures between charged surfaces compared to the uncharged system.** (a) Small coupling parameter $\Xi = 0.43$, corresponding to a surface charge density $\sigma = -0.11\,\mathrm{e/nm^2}$. (b) Intermediate coupling parameter $\Xi = 1.53$, corresponding to a surface charge density $\sigma = -0.385\,\mathrm{e/nm^2}$. The inset zooms into the region where SC yields negative pressures on a linear scale. (c) Results for $\Xi = 3.06$, corresponding to $\sigma = -0.77\,\mathrm{e/nm^2}$. Dashed lines denote the pressure from solution of the PB equation, Eq. (4.34), dotted lines show the SC pressure Eq. (4.7), and dash-dotted lines the next-leading correction to SC, Eq. (4.9). Crosses denote results from MC simulations.

simulations (shown as crosses). The MC pressures are right in between the PB expression Eq. (4.34) and the next-leading SC pressure, Eq. (4.9), shown as dash-dotted lines in Fig. 4.6. The inset of Fig. 4.6 (b) reveals that the SC expression Eq. (4.7), shown as dotted line, becomes negative at the expected SC equilibrium separation $\tilde{d} = 2$, which is at $d = 1\,\mathrm{nm}$ for $\Xi = 1.53$. The MD data in explicit water for $d > 0.5$ are between the weak and strong coupling expressions, and deviate significantly at smaller separations. Figure 4.6 (c) shows the results for $\Xi = 3.06$. In this case the pressures obtained from MC simulations (crosses in Fig. 4.6 (c)) deviate by nearly a factor 2 from the PB pressure (crosses vs dash-dotted line in Fig. 4.7 (c)). Strikingly, the pressure from the atomistic MD simulations shows a minimum at about 0.5 nm. The appearance of this minimum can not be explained within SC theory, shown as dotted line in Fig. 4.7 (c).

4.4. Discussion and Conclusion

In this work, using explicit water, we have shown show that the interaction between charged surfaces in aqueous solution can be analyzed via additive contributions stemming from the interaction between neutral surfaces (which is governed by the hydration in case of polar surfaces and at small separations) and a contribution due to the surface charge and the ions. In the case of low surface charge σ and for separations $d > 0.5\,\mathrm{nm}$, the interaction can be modeled by additive contributions from the hydration repulsion and the PB pressure, $\Pi = \Pi_{\mathrm{hyd}} + \Pi_{\mathrm{PB}}$. In that description, the dielectric constant is assumed to be homogeneous and equal to its bulk value $\varepsilon_{\mathrm{bulk}} = 70$ for SPC/E water independent of the confinement. For small charge densities the repulsive PB pressure is mainly due to the ion entropy and thus indeed independent of the solvent dielectric constant, see Eq. (4.36). To the best of our knowledge this is the first atomistic simulation with explicit water confirming the mean-field pressures!

We have shown that the ionic density profiles, if the surface repulsion is neglected, at larger separations, $d > 1\,\mathrm{nm}$ can be described by the Poisson–Boltzmann expressions for small surface charge, see Fig. 4.2 (a). In stronger confinement our simulation results suggest that the density profiles as can be modeled by taking into account the leading correction to SC already for the small coupling parameters $\Xi = 1.5$ and 3.

Ionic density profiles between homogeneously charged planar walls have been obtained in the presence of dielectric discontinuities, where corrections to the PB limit are found to be small for small values of the coupling parameter Ξ [190], but with increasing Ξ the image charge repulsion strongly pushes the ions into the slab center [189]. An opposing effect is, however, observed for discrete surface charges, in which case the ion density close to the surface is increased in absence of dielectric contrast. Including image charge effects results in a competition between dielectric repulsion from the surface and the adsorption due to discrete charges [191]. Within the Poisson–Boltzmann description of salt solutions, the tendency of the counter-ions to adsorb on the surface or be repelled can be incorporated via effective potentials. The resulting pressures then are attractive or repulsive, respectively [76, 192, 193]. In the SC regime the effect of charge discreteness sensitively depends on the surface charge pattern and can result in stable minima of the free energy, attraction or repulsion [194, 195]. Our results suggest that dielectric inhomogeneities, which we neglect in our analysis, are of minor importance. For atomistic modeled water also the image charge contributions of the water partial charges contribute, which around a solvated ion will give a compensating contribution.

Summarizing, we have established a method using simulations at controlled water chemical potential, which allow to analyze the hydration force and compare the interaction between uncharged and charged surfaces in the presence of neutralizing counterions. The combined effects become important at the nanometer separation. Thus the findings open a rich field of studies for the atomistic effects when aqueous electrolyte solutions are confined, which is the case both in biological as well as in industrial applications. From the atomistic analysis we find that continuum modeling is successful even at lengthscales where the water structure needs to be considered explicitly, yet our analysis leaves many points for future work, like dielectric effects in the charged systems, or the inclusion of repulsive ion–surface potentials within the PB framework in the case where only counterions are present.

4.5. Supplemental material

4.5.1. Ion force-field parameters

In Fig. 4.8 we show the cation density profiles for $\sigma = -0.109\,\mathrm{e/nm^2}$ (B1-3) (colored lines) and the PB density (dashed black line). The corresponding coupling parameter is $\Xi = 0.43$, thus PB is expected to be perfectly valid and the PB pressure at $d = 4.09\,\mathrm{nm}$ is less than 1.5 bar. The interaction between the neutral but polar surfaces is zero within numerical accuracy at such large separations, thus we perform the corresponding simulations in the $N_\mathrm{w}A\Pi_0T$ ensemble with a barostat ensuring that the normal pressure Π_0 is 1 bar. The simulations for evaluating the density profiles have a length of 100 ns each. We analyze the interaction parameters of the sodium ion with the Decanol oxygen and compare the obtained density profiles to PB in Fig. 4.8. The LJ potential is defined as

$$U_\mathrm{LJ}(r) = 4\epsilon\left[\left(\frac{\varsigma}{r}\right)^{12} - \left(\frac{\varsigma}{r}\right)^{6}\right] = \frac{C_{12}}{r^{12}} - \frac{C_6}{r^6}, \tag{4.10}$$

	$\varsigma^{(\mathrm{iw})}$ [Å]	$\epsilon^{(\mathrm{iw})}$ [kJ/mol]	$\varsigma^{(\mathrm{ii})}$ [Å]	$\epsilon^{(\mathrm{ii})}$ [kJ/mol]	$\varsigma^{(\mathrm{io})}$ [Å]	$\epsilon^{(\mathrm{io})}$ [kJ/mol]	$\varsigma^{(\mathrm{ic})}$ [Å]	$\epsilon^{(\mathrm{ic})}$ [kJ/mol]
GROMOS	2.86	0.20	2.58	0.06	2.76	0.23	3.23	0.16
Dang	2.88	0.52	2.58	0.42	-	-	-	-
Comb. rule	-	-	-	-	2.76	0.92	3.24	0.64

Table 4.3.: **Ion forcefield parameters.** Ion-water (iw) and ion-ion (ii) Lennard–Jones parameters for taken from GROMOS and from Dang et al., Ref. [184]. The interactions between the ions and the headgroup oxygen (io) and the carboxyl methylene group (ic) are taken from the GROMOS forcefield and by using the combination rule Eq. (4.11).

which has a minimum at $2^{1/6}\varsigma$. The headgroup hydrogen does not have any LJ interactions, thus the main contribution to the ion–surface interaction stems from the headgroup oxygen and the methylene groups, for which the corresponding parameters are listed in 4.3

For our analysis in the main text we use ion–ion and ion–water interactions taken from Ref. [184], however the ion–surface interactions need to be determined. A standard approach is using the combination rule

$$C_6^{(ij)} = \sqrt{C_6^{(i)} C_6^{(j)}} \qquad \text{and} \qquad C_{12}^{(ij)} = \sqrt{C_{12}^{(i)} C_{12}^{(j)}}, \tag{4.11}$$

for which the corresponding parameters are listed in the last row of Table 4.3.

The resulting density profile is shown as blue line in Fig. 4.8, yielding good agreement between the expected PB density profile and the simulation result. Using the GROMOS values for sodium, given in the first line of Table 4.3, results in the green density profile shown in Fig. 4.8, which within the statistical noise is indistinguishable from the profiles using the combination rule (shown in blue). However, combining the ion parameters from Dang et al., second line in Table 4.3, with the GROMOS values for the ion–surface interaction, first line in Table 4.3, leads to the density profiles shown as orange line in Fig. 4.8, where the ions adsorb strongly. Considering the similar values in Table 4.3, the reason for this adsorption remains unclear

In our main analysis, we use a purely repulsive ion–headgroup oxygen interaction, $C_6^{(\mathrm{io})} = 0$, and set $C_{12}^{(\mathrm{io})} = 2.5 \cdot 10^{-7}\,\mathrm{kJ/mol\,nm^{12}}$ (see Eq. (4.10)), with ion–methylene interactions taken from GROMOS (first line in Table 4.3). The resulting density profile is shown as red line in Fig. 4.8 and yields good agreement with the PB profile. Obviously great care has to be taken when adjusting the ion–surface interactions with respect to the correct combination rule, whereas then the obtained profiles for the ion parameters from Dang et al. [184] and GROMOS yield similar results. In order to minimize ion-specific effects that might appear in strong confinement or at higher surface charges, we take the combination of sodium-sodium and sodium-water parameters from Ref. [184] stick with

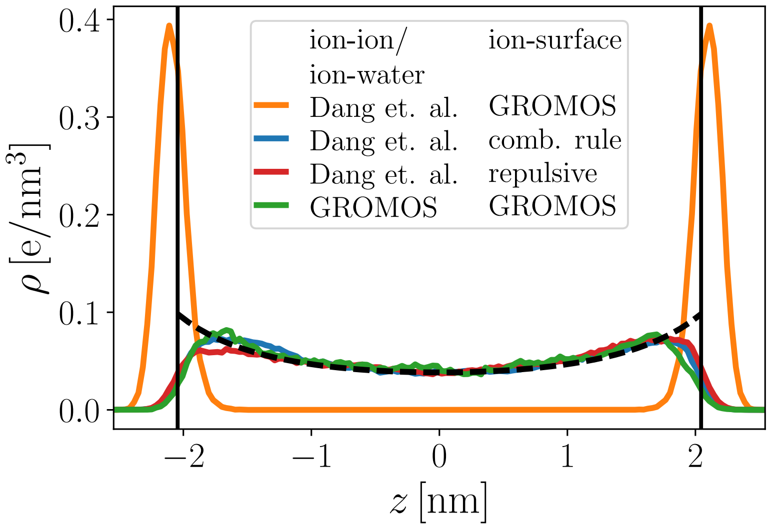

Figure 4.8.: **Ion density profiles for different ion–surface interactions.** Charge density for system B1-3 at $d = 4.09\,\mathrm{nm}$ and surface charge density $\sigma = -0.109\,\mathrm{e/nm^2}$ with different ion-surface interactions. Black dashed line shows the PB density profile, green the ion density obtained from the GROMOS forcefield. In yellow the combination of ion parameters by Dang et al. [184] and the GROMOS ion–surface parameters is shown, blue line shows the resulting profile using the geometric mean. The repulsive potential using $C_{12} = 2.5 \cdot 10^{-7}\,\mathrm{kJ/mol\,nm^{12}}$ and $C_6 = 0$ employed for further analysis is shown as red line.

repulsive ion–surface interaction (red line in Fig. 4.8) for our analysis.

4.5.2. Van der Waals Interaction

Here, we investigate whether the slight minimum apparent in Fig. 4.3 at separations of about 1 nm in the interaction of the neutral surfaces can be ascribed to van der Waals (vdW) interactions. In our model, all particles interact via 12–6 Lennard-Jones (LJ) potentials, which mimic the Pauli exclusion and dispersion attractions. Pairwise summation of all parts of the LJ interaction $u(r) = \mathrm{C}_{12}/r^{12} - \mathrm{C}_6/r^6$ leads to the vdW-like attraction between two interacting semi-infinite half-spaces with parameter C_6 and the repulsive term with C_{12} is a phenomenological model to mimic the Pauli principle; i.e.,

$$\Pi_{\mathrm{LJ}} = \frac{H_{12}}{45\pi d^9} - \frac{H_6}{6\pi d^3}, \tag{4.12}$$

where H_6 is the well-known Hamaker constant and H_{12} its counterpart for the repulsive interactions. From the known atomic densities in our simulations, they can be evaluated as [28]

$$H_\alpha = \pi^2 C_{\alpha,\mathrm{s}} n_\mathrm{s}^2 - 2\pi^2 C_{\alpha,\mathrm{sw}} n_\mathrm{s} n_\mathrm{w} + \pi^2 C_{\alpha,\mathrm{w}} n_\mathrm{w}^2, \tag{4.13}$$

where $\alpha = \{6, 12\}$ and $n_\mathrm{s} = 38\,\mathrm{nm}^{-3}$ and $n_\mathrm{w} = 33\,\mathrm{nm}^{-3}$ are the number densities of the Decanol carbon tails and bulk water, respectively. The LJ coefficients in our force fields are $C_{6,\mathrm{s}} = 7.47$, $C_{6,\mathrm{sw}} = 4.42$ and $C_{6,\mathrm{w}} = 2.62$ in units of $10^{-3}\,\mathrm{kJ\,mol^{-1}\,nm^6}$ for the attractive surface–surface, surface–water, and water–water atom interactions, respectively, and $C_{12,\mathrm{s}} = 3.40$, $C_{12,\mathrm{sw}} = 0.95$ and $C_{12,\mathrm{w}} = 0.26$ in units of $10^{-5}\,\mathrm{kJ\,mol^{-1}\,nm^{12}}$ for the corresponding repulsive interactions. This gives an estimate for the Hamaker constant for the Decanol surfaces across water of $H_6 \approx 10\,k_\mathrm{B}T$ and for the repulsive counterpart we obtain $H_{12} \approx 0.11\,k_\mathrm{B}T$.

However, the LJ interactions are cut off in our simulations at a radius of $r_\mathrm{c} = 0.9\,\mathrm{nm}$, the actual values for the dispersion attraction and Pauli repulsion are smaller. In the following, we derive the expression for the normal pressure between the surfaces, including a finite cutoff for the LJ interactions. Two infinitely small volume elements $\mathrm{d}V_1$ and $\mathrm{d}V_2$ of hydrocarbons in water interact with the energy of

$$\mathrm{d}W = \left(\frac{H_{12}}{\pi^2 s^{12}} - \frac{H_6}{\pi^2 s^6}\right), \tag{4.14}$$

where s is their distance. The force acting in the z direction is obtained as $F_z = (\mathrm{d}W/\mathrm{d}s) \times (h/s)$, where h is the projection of the distance s on the z axis. The interaction cutoff at distance r_c can be included via a Heaviside step function $\theta(r_\mathrm{c} - s)$, which is 1 for $s < r_\mathrm{c}$ and 0 otherwise. Thus, the LJ force in the z direction acting between the two volume elements reads

$$\mathrm{d}F_z = \left(\frac{12H_{12}}{\pi^2}\frac{h}{s^{14}} - \frac{6H_6}{\pi^2}\frac{h}{s^8}\right)\theta(r_\mathrm{c} - s)\,\mathrm{d}V_1\,\mathrm{d}V_2. \tag{4.15}$$

We now use cylindrical coordinates to integrate over the two half-spaces separated by a distance d with the volume elements $\mathrm{d}V_1 = 2\pi r_1 \mathrm{d}r_1 \mathrm{d}b_1$ and $\mathrm{d}V_2 = 2\pi r_2 \mathrm{d}r_2 \mathrm{d}b_2$. We can directly perform one integral, $\int 2\pi r_2 \mathrm{d}r_2 = A$ yielding the lateral area A. Using that b_1 and b_2 denote the distance from the two interfaces, we can express $h = d + b_1 + b_2$ and thus $s = \left(h^2 + r^2\right)^{1/2}$, such that from Eq. (4.15) the pressure follows as

$$\Pi_\mathrm{LJ} = \frac{F_z}{A} = \int_0^\infty \mathrm{d}b_1 \int_0^\infty \mathrm{d}b_2 \int_0^\infty \mathrm{d}r \frac{12hr}{\pi}\left(\frac{2H_{12}}{s^{14}} - \frac{H_6}{s^8}\right) \cdot \theta(r_\mathrm{c} - s), \tag{4.16}$$

which for $r_\mathrm{c} \to \infty$ recovers Eq. (4.12) and which we solve numerically for finite r_c.

Besides dispersion interactions, which are in our model implicitly included via LJ potentials, the permanent water dipoles additionally contribute to the zero-frequency (Keesom) part of the vdW interactions. These contributions are implicitly included in our simulations as well via the electrostatic dipole interactions. The corresponding Hamaker constant for a dielectric mismatch $\Delta = (\varepsilon_1 - \varepsilon_2) / (\varepsilon_1 + \varepsilon_2)$, where $\varepsilon_1 = 80$ is the (bulk) water dielectric constant and $\varepsilon_2 = 1$ inside the Decanol bilayers, is $H_0 \approx 3/4 k_\mathrm{B}T$ [87] and because there is no cutoff, it follows Eq. (4.12). Note that for a full analysis of the Lifshitz interactions the frequency-dependent dielectric permittivity in confinement is required, making such an analysis highly involved. However, estimates based on water hydrocarbon systems indicate that these corrections amount to a contribution $\lesssim 1\,k_\mathrm{B}T$ in the relevant distance regime, see e.g. Refs. [31, 196], in conjunction with experiments [7, 197].

The derived equations for the vdW pressure assume a continuum model of hard interacting walls. On the contrary, the surfaces in our simulations are flexible and the definition of the separation d needs to be accounted for. In our analysis we define $d = d_\mathrm{s} - d_\mathrm{s}^0$ as the oxygen separation minus the measured separation at zero water content. To compare the MD simulation results with the continuum model, we reduce the surface separation in Eqs. (4.12) and (4.16) by d_s^0, which ensures that the LJ repulsion does not diverge at $d_\mathrm{s} = 0$, but at $d = -d_\mathrm{s}^0$, corresponding to the case of overlapping densities of the Decanol oxygens.

Fig. 4.9 shows the simulation normal pressure for the neutral, polar Decanol surfaces across water together with the LJ interaction without cutoff Eq. (4.12) (dashed red line) and the corresponding pressure including the cutoff at $r_\mathrm{c} = 0.9\,\mathrm{nm}$ (solid blue line). Incidentally, the full LJ expression, red dashed line in Fig. 4.9 seems to describe the data reasonable well, however, the resulting attractive minimum is at too small separations and can not be balanced by an exponential, i.e., the minimum will always be at smaller separations than in the simulations. This becomes even more obvious when comparing the data with the LJ including the cutoff, which is zero for $d > r_\mathrm{c} - 2d_\mathrm{s}^0 = 0.7\,\mathrm{nm}$, the same separation at which the simulation data evidently get positive, see inset of Fig. 4.9. The dash-dotted yellow line in Fig. 4.9 represents the Keesom interactions, which are negligible in the scale of our simulations. We conclude that vdW interactions cannot explain a possible minimum of the interaction pressure around $d = 1\,\mathrm{nm}$.

4.5.3. Water uptake of the charged system

In Figure 4.10 (a) we show the number of waters per Decanol headgroup, $N_\mathrm{w}/N_\mathrm{s}$ vs. box length L_z for the uncharged surfaces and charge densities between $\sigma = -0.11$ and $-0.77\,\mathrm{e/nm}^2$. With increasing surface charge the system at bulk water chemical potential

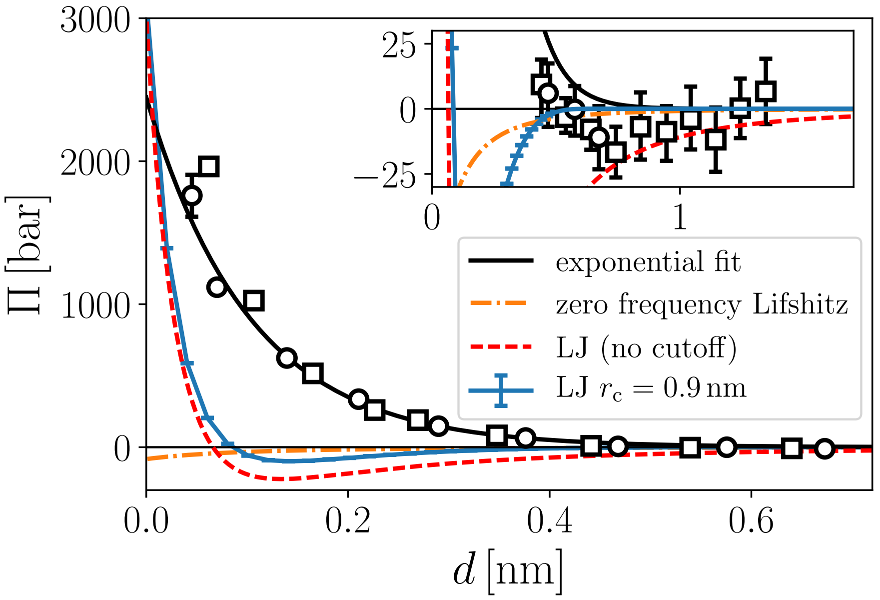

Figure 4.9.: **Comparison of the vdW contributions with the simulated pressure.** The total normal interaction pressure from MD simulations between the neutral surfaces is shown as black symbols, the different vdW contributions are shown by the different lines: for full-range LJ contribution (Eq. (4.12), red dashed line) and for cutoff LJ contribution (Eq. (4.16), blue solid line), both with $H_6 = 10k_\mathrm{B}T$ and $H_{12} = 0.11k_\mathrm{B}T$, and for the Keesom contribution from the water dipoles with $H_0 = 3/4k_\mathrm{B}T$ (orange dashed-dotted line).

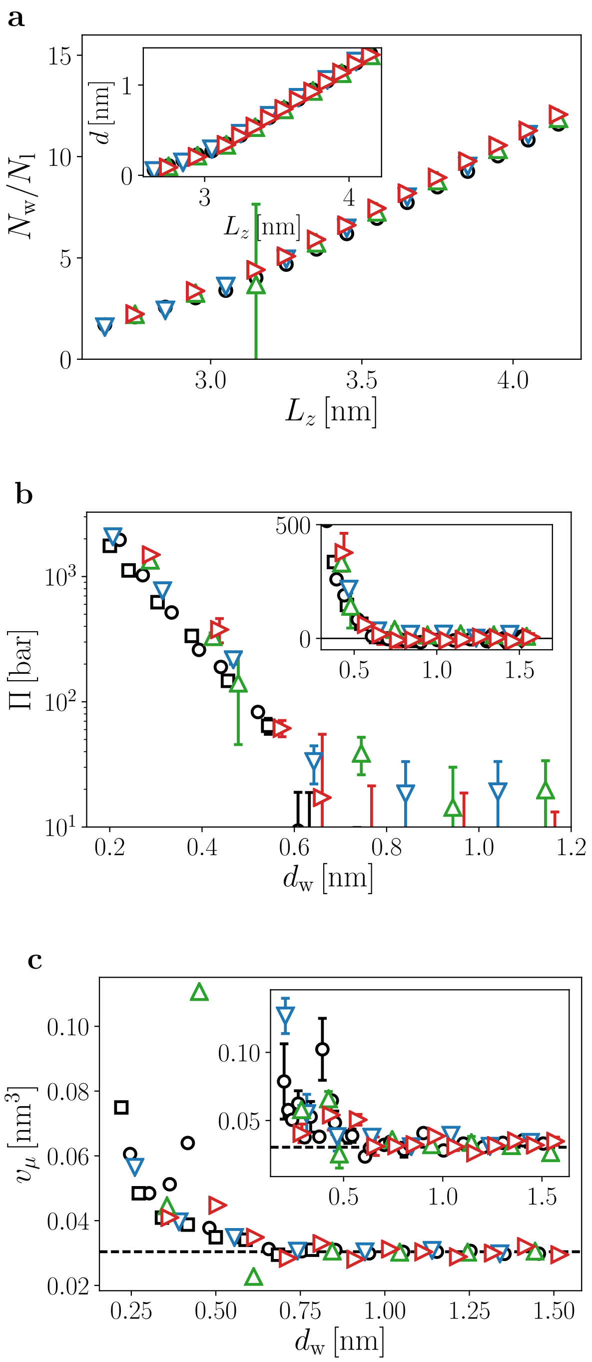

Figure 4.10.: **Water uptake in the charged system.** (a) Water number N_w per Decanol molecule as a function of the box length for different surface charge densities $\sigma = 0, -01.1, -0.39$ and $-0.77\,\mathrm{e/nm}^2$ (black, blue, green and red data, respectively). The inset shows the headgroup separation vs. box length. (b) Interaction pressure as a function of the water slab thickness d_w. Symbols refer to the same data as in (a). The inset shows the data on a linear scale. (c) Partial water volume v_μ at bulk water chemical potential.

takes up more water at the same box length. As is seen from the inset of Fig. 4.10 (a), which shows the surface separation d as defined in the main text, this additional water uptake can not be attributed to a compression of the surface as the data are nearly on top of each other.

The water partial volume follows from our simulations at controlled chemical potential μ in two ways: From the derivative of the box length with respect to the water number, (the lateral area A is constant in our simulations),

$$v_{\mathrm{w}} = \left(\frac{\partial L_z}{\partial N_{\mathrm{w}}} \right)_{A,\mu} A, \tag{4.17}$$

shown in Fig. 4.10 (c), or via the change of the chemical potential μ at different pressures Π (which we adjust via N_{w}),

$$v_{\mathrm{w}} = \left(\frac{\partial \mu}{\partial \Pi} \right)_{A,L_z}. \tag{4.18}$$

The resulting data from Eq. (4.18) is shown in the inset of Fig. 4.10 (c). The general observation from Fig. 4.10 (c) is that for separations $d_{\mathrm{w}} < 0.75\,\mathrm{nm}$ the water volume significantly increases, and is about twice its bulk value $v_\mu = 0.0304\,\mathrm{nm}^3$ (determined independently from bulk simulations) in strongest confinement. Although the data is subject to large numerical noise, it suggests that the water partial volume at higher charge densities and for monovalent counter-ions is slightly smaller than for water between the uncharged surfaces (black data in Fig. 4.10 (c)).

The corresponding pressure Π vs. water slab thickness d_{w} is shown in Fig. 4.10 (b). Whereas the short-range repulsion when plotted as a function of d in Fig. 4.6 for the different surface charges nearly perfectly converge onto the exponential hydration contribution, the result for d_{w} in Fig. 4.10 (b) shows a much stronger repulsion, which is results from a shift on the x-axis due to water uptake.

4.5.4. Monte Carlo simulations

We perform NVT Monte Carlo simulations of $N_{\mathrm{ion}} = 50$ point-like counterions in a box of lateral size L, which is determined by electro-neutrality, $L = \sqrt{N_{\mathrm{ion}}/(2\sigma)}$. The counterions are confined between two surfaces located at $z = 0$ and $z = d$. The electrostatic energy is obtained using a generalized efficient 3D Ewald summation method with correction for slab geometry [198]. In this method an empty layer which is 3 times larger than the wall separation [171] is considered in region $d < z < 3d$. After 1×10^6 MC steps for equilibration we save 1×10^6 uncorrelated configurations each 1000 MC steps for further

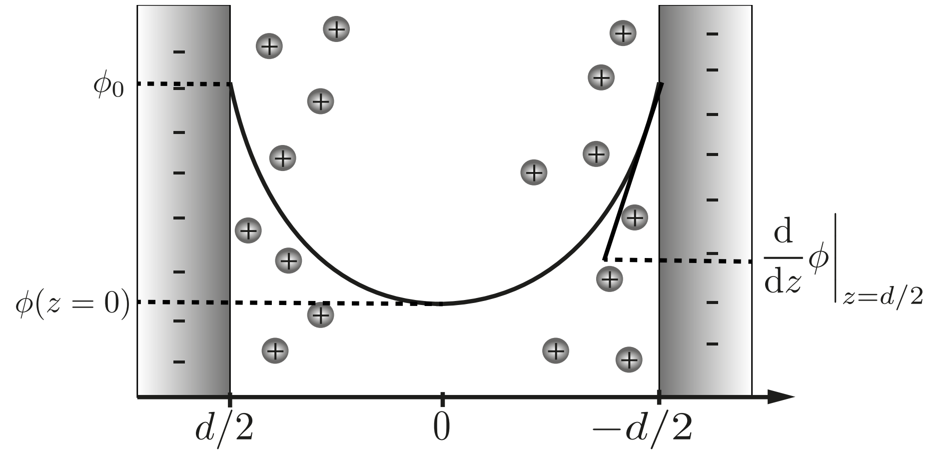

Figure 4.11.: **Sketch of the system of counterions confined between charged walls.** For modeling a solid surface at the head-group oxygen position is assumed which bears a surface charge density σ. For the solution of the PB equation we treat the slab as homogeneous dielectric medium without contrast to the semi-infinite walls.

analysis.

4.5.5. Nonlinear Poisson–Boltzmann equation for counterions

We consider the nonlinear Poisson–Boltzmann equation for two charged surfaces with neutralizing counterions, see Fig. 4.11. In SI-units the one-dimensional Poisson-Boltzmann equation reads as [87]

$$\varepsilon\varepsilon_0 \frac{\mathrm{d}^2\phi}{\mathrm{d}z^2} = -\rho = -q\mathrm{e}c_0 e^{-q\mathrm{e}\phi/k_\mathrm{B}T}, \tag{4.19}$$

with the counterion charge density ρ, q is the ion valency and c_0 is given by electro-neutrality. We make use of the symmetry and solve Eq. (4.19) for $z \in [0, d/2]$ with the boundary conditions

$$\left.\frac{\mathrm{d}\phi}{\mathrm{d}z}\right|_{z=0} = 0 \tag{4.20}$$

$$\text{and} \qquad \left.\frac{\mathrm{d}\phi}{\mathrm{d}z}\right|_{z=d/2} = \frac{\sigma}{\varepsilon\varepsilon_0} = -E(z)|_{z=d/2}\,. \tag{4.21}$$

In the following we assume the surfaces to bear a negative surface charge, $\sigma < 0$. From differentiating Eq. (4.19) one obtains

$$\begin{aligned}\frac{\mathrm{d}\rho}{\mathrm{d}z} &= q\mathrm{e}c_0\frac{\mathrm{d}}{\mathrm{d}z}e^{-q\mathrm{e}\phi/k_\mathrm{B}T} = -\frac{q\mathrm{e}c_0}{k_\mathrm{B}T}e^{-q\mathrm{e}\phi/k_\mathrm{B}T}\frac{\mathrm{d}\phi}{\mathrm{d}z}\\ &= \frac{\varepsilon\varepsilon_0}{k_\mathrm{B}T}\frac{\mathrm{d}\phi}{\mathrm{d}z}\left(\frac{\mathrm{d}^2\phi}{\mathrm{d}z^2}\right) = \frac{\varepsilon\varepsilon_0}{2k_\mathrm{B}T}\frac{\mathrm{d}}{\mathrm{d}z}\left(\frac{\mathrm{d}\phi}{\mathrm{d}z}\right)^2 \qquad (4.22)\end{aligned}$$

where in the last step chain rule was applied. We now choose an integration path from a reference point $z = 0$ to an arbitrary point in the system, $z = z_0$,

$$\int_0^{z_0}\frac{\mathrm{d}}{\mathrm{d}z}\left(\frac{\mathrm{d}\phi}{\mathrm{d}z}\right)^2\mathrm{d}z = \int_0^{z_0}\frac{2q\mathrm{e}c_0k_\mathrm{B}T}{\varepsilon\varepsilon_0}\frac{\mathrm{d}}{\mathrm{d}z}e^{-q\mathrm{e}\phi/k_\mathrm{B}T}\mathrm{d}z, \qquad (4.23)$$

and after performing the integral this yields the first derivative,

$$\frac{\mathrm{d}\phi}{\mathrm{d}z} = \pm\sqrt{\frac{2q^2\mathrm{e}^2c_0}{\varepsilon\varepsilon_0k_\mathrm{B}T}}\left(e^{q\mathrm{e}\phi/k_\mathrm{B}T}-1\right)^{1/2}, \qquad (4.24)$$

where we have eliminated the integration constant by choosing $\phi(z = 0) = 0$ without loss of generality and set $z_0 = z$ again. The sign of the root corresponds to taking the derivative at the left or the right boundary, see Fig. 4.11, and as here we consider $0 \leq z \leq d/2$ the positive root has to be taken. Integration in ϕ from 0 to ϕ_0 results in

$$\begin{aligned}\int_0^{\phi_0}\mathrm{d}\phi\frac{\mathrm{d}z}{\mathrm{d}\phi} &= \sqrt{\frac{2q\mathrm{e}c_0k_\mathrm{B}T}{\varepsilon\varepsilon_0}}\int_0^{\phi_0}\mathrm{d}\phi\left(e^{q\mathrm{e}\phi/k_\mathrm{B}T}-1\right)^{-1/2} \qquad (4.25)\\ \Leftrightarrow z &= \sqrt{\frac{\varepsilon\varepsilon_0}{2q\mathrm{e}c_0k_\mathrm{B}T}}\left(-\frac{2k_\mathrm{B}T}{q\mathrm{e}}\times\right.\\ &\qquad \left.\arctan\left[\left(e^{q\mathrm{e}\phi/k_\mathrm{B}T}-1\right)^{1/2}\right]\right). \qquad (4.26)\end{aligned}$$

Introducing the inverse length $\kappa^2 = 2\pi\ell_Bc^0$ with the Bjerrum length $\ell_\mathrm{B} = q^2e^2/4\pi\varepsilon\varepsilon_0k_\mathrm{B}T$, this simplifies to

$$z = -\frac{1}{\kappa}\arctan\left[\left(e^{q\mathrm{e}\phi/k_\mathrm{B}T}-1\right)^{1/2}\right], \qquad (4.27)$$

which can be inverted and solved for the electrostatic potential:

$$\begin{aligned}e^{-q\mathrm{e}\phi/k_\mathrm{B}T} &= \tan^2(\kappa z)+1 \qquad (4.28)\\ \Rightarrow \phi(z) &= 2\frac{k_\mathrm{B}T}{q\mathrm{e}}\ln\left(\cos(\kappa z)\right). \qquad (4.29)\end{aligned}$$

Applying the boundary condition from Eq, (4.21) gives

$$\frac{\sigma}{\varepsilon\varepsilon_0} = \left.\frac{\mathrm{d}\phi}{\mathrm{d}z}\right|_{z=d/2} = -\frac{2k_\mathrm{B}T}{q\mathrm{e}}\kappa\tan(\kappa d/2). \tag{4.30}$$

The solution for the electrostatic potential, Eq. (4.29), is then obtained from the solution of the transcendental equation [199]

$$\kappa\tan\left(\kappa d/2\right) = b^{-1}. \tag{4.31}$$

where we introduced the Gouy–Chapman length (using the definition that $\sigma < 0$), $b = -\mathrm{qe}/2\pi\ell_B\sigma$.

According to Eq. (4.29) the physical solution must fulfill $\cos\left(\kappa z\right) > 0$, i.e., $-\pi/2 < \kappa d/2 < \pi/2$ and considering the fact that lengths should be positive the solution is unique in the interval $0 < \kappa < \pi/d$. Correspondingly, the cation (as $\sigma < 0$) density is obtained from the Boltzmann equation as

$$\rho(z) = c_0 e^{-q\mathrm{e}\phi/k_\mathrm{B}T} = \frac{\kappa^2 b\sigma}{\cos^2(\kappa z)}. \tag{4.32}$$

The interaction pressure can now be obtained via the contact value theorem as the excess osmotic pressure at the midplane, where the field is zero according to Eq. (4.21) [200]

$$\Pi_\mathrm{PB} = k_\mathrm{B}Tc(z=0), \tag{4.33}$$

which considering the dependence of κ on d yields

$$\Pi_\mathrm{PB} = k_\mathrm{B}T\left[\kappa^2(d)b\sigma\right] = \frac{k_\mathrm{B}T}{2\pi\ell_B q}\kappa^2(d). \tag{4.34}$$

For the analysis of our simulations, we express all length-scales in nanometers, such that the prefactor of the latter expression reads as $k_\mathrm{B}T/\mathrm{nm}^3 = 41.42\,\mathrm{bar}$.

We will now discuss two limiting cases, which we obtain by multiplying Eq (4.31) with d. In the first limit, $d/b \ll 1$, the resulting interaction pressure is mainly entropic as ions get sucked into the slab, thus we refer to it as *ideal gas* regime. Expanding Eq (4.31) to third order [70] one obtains

$$\kappa^2 = \frac{2}{db} - \frac{1}{3b^2}. \tag{4.35}$$

The resulting pressure,

$$\Pi_{\mathrm{id}}/k_{\mathrm{B}}T \approx \frac{2\sigma}{qed} + \frac{2\pi\ell_B}{3e^2}\sigma^2, \tag{4.36}$$

consists of two terms, the first of which is the entropic pressure N/V due to the counterion confinement, the second term is due to electrostatic interactions between the charged plates. Note that if the expansion is performed to linear order only, the resulting pressure is simply N/V, thus the same as an ideal gas.

On the other hand, if $d/b \gg 1$, electrostatic interactions dominate in this so-called *Gouy–Chapman* regime and the tangens in Eq (4.31) gets maximal as its argument approaches $\pi/2$, thus here we obtain

$$\kappa = \pi/d. \tag{4.37}$$

Note that the Poisson–Boltzmann pressure is always repulsive and for $d \ll b$ it decays as d^{-1}, whereas at larger separations $d \gg b$ it goes like d^{-2},

$$\Pi_{\mathrm{GC}} \approx \frac{\pi}{2\ell_B q}\frac{1}{d^2}, \tag{4.38}$$

and is independent of the surface charge.

In Figure 4.12 we show the Poisson-Boltzmann interaction pressure using the solution of the transcendental equation (4.31) as well as the limiting cases. Clearly, the osmotic pressure dominates for small separations and as long as the interaction between the ions and the charged walls is small. In our simulations systems, however, we cover roughly values $0.1 < d/b < 10$, which makes the exact solution of the transcendental equation necessary.

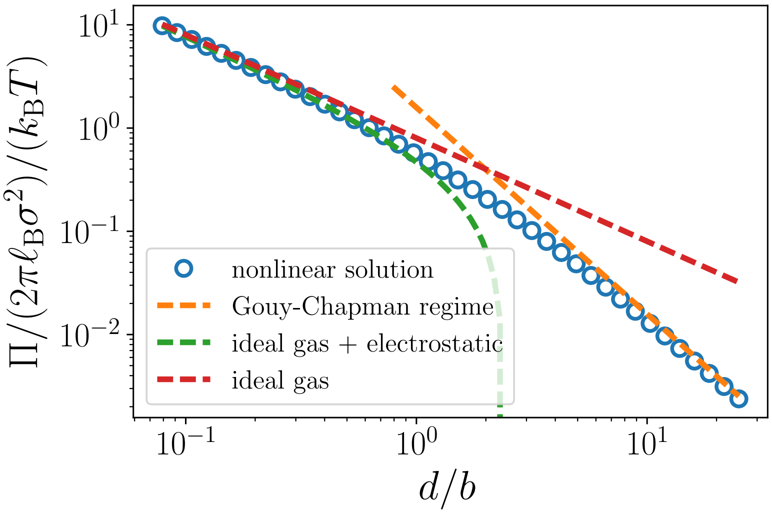

Figure 4.12.: **Electrostatic pressures in PB theory** obtained from the nonlinear PB equation Eq. (4.34) (empty symbols), from Gouy–Chapman approximation Eq. (4.38) (orange dashed line) and in the limit $d \ll b$ Eq. (4.36) (green dashed line). The red dashed line is only the osmotic contribution from Eq. (4.36).

5. Hydration friction in nano-confinement: from bulk via interfacial to dry friction

Bibliographic information: Parts of this chapter have previously been published. Reprinted with permission from Ref. [vi]. Copyright 2017 American Chemical Society.

Summary & Outlook

The water molecular details are of utmost importance for a in-depth understanding of the interaction between surfaces in the aqueous environment. This not only applies to biological systems, but also for many industrial applications. For example, physiological function and dysfunction is strongly related to the surface separation between membranes, and friction between solvated surfaces on the nano-scale appears in every-day life, where cartilage is a prominent example. The work presented in the preceding chapters aims at extracting information about the water atomistic details obtained from Molecular Dynamics (MD) simulations and incorporating them into complementing continuum models for the surface–surface interactions. It is important to stress that the fact that common continuum models fail on molecular lengthscales is not necessarily because the employed approaches become invalid, but rather because the material parameters, or say response functions, differ from the ones that are macroscopically accessible and can be measured in bulk-like systems. Rigorous modeling of all relevant degrees of freedom in computer simulations makes the relevant observables directly accessible and offers the possibility to test theoretical models to and gain new insight into the molecular details of experimental observations.

Before summarizing the results of this work, it is important to emphasize that - like in experimental setups - the use of the correct ensemble crucially matters in simulations. One typical way of experimentally determining the surface–surface interactions, is the method of osmotic stress, discussed in Chapter 1 and Appendix A, and the same approach can be employed in computer simulations. However, the precise knowledge of the water chemical potential is required, which numerically is still challenging. Controlling the water chemical potential, which we discuss in Appendix A, then allows to analyze the underlying interaction mechanisms. The constant chemical potential ensemble is implemented in MD simulations by adjusting either the water number, or the simulation volume. The corresponding computational methods and simulation setups were improved in the context of this work

Performing simulations of surface–surface interactions in explicit water at controlled water chemical potential, we extract the water dielectric response in planar confinement between soft, hydrophilic surfaces in Chapter 2. For a water slab thickness below 1 nm the dielectric response is highly asymmetric: while the component parallel to the interface slightly increases compared to bulk, the perpendicular one decreases drastically due to anti-correlated polarization of neighboring water molecules. The flexible polar headgroups contribute significantly to the dielectric profile and we present an effective dielectric tensorial box model suitable for coarse-grained electrostatic modeling.

We quantify the interaction pressures between membranes in terms of a Landau–Ginzburg theory, as proposed in the 1970s by Marčelja and Radić, in Chapter 3. The essential idea in this model is that the water contribution to the surface interaction is due to water ordering, however there are many possible choices for order parameters, some of which are attractive, some repulsive. We investigate an experimentally well studied model membrane system consisting of Dipalmitoylphosphatidylcholine (DPPC) bilayers in the ordered and disordered state and show that the relevant order parameters follow from the water polarization, for which we find quantitative agreement between the polarization profiles and the decay lengths of the indirect, water-mediated pressure. To study the effects of surface structure and chemistry more deeply, we also include a Decanol bilayer in our analysis. Using Gaussian field theory, the free parameter in the Landau model is determined from the order parameter fluctuation, which allows to quantitatively predict the pressures within the one-dimensional mean-field model. The water polarization constitutes about 10% of the indirect repulsion between the membranes and we find other order parameters to be negligible for the total repulsion. Considering that the shape of the indirect pressures as well as the order parameter profiles are well described by the expressions resulting from the Landau–Ginzburg model, we attribute the different prefactor to contributions stemming from lateral correlation effects and the extended surface polarity distribution

The electrostatic interactions between surfaces across an aqueous solution is of fundamental importance, as most biological or industrial surfaces become effectively charged in contact with water. We study the interplay of hydration and electrostatic forces (Chapter 4) by comparing a Decanol model system, where we artificially put surface charges on the headgroups, in the presence of counter-ions with the uncharged surface. Such a procedure is inspired by atomic force microscope (AFM) measurements of self-assembled monolayers with the same headgroup chemistry, which are attached to a gold cathode. Using the AFM tip as the anode, the interaction at different electric fields, similar to a variation of the surface charge in our setup, can then be studied. At separations $d > 0.5\,\mathrm{nm}$ the exponential hydration repulsion has decayed to zero and the simulations pressures at low charge density are consistent with solution of the Poisson–Boltzmann equation. With increasing surface charge density we observe a qualitative change in the pressure–distance curves, which is not captured within the classical continuum electrostatic models. The behavior at small separations $d < 0.5\,\mathrm{nm}$ is strongly influenced by repulsive ion–surface interactions, however the exponential repulsion dominates the total pressure in this regime. Our results reveal that the interaction can be thought of as a combination of hydration and electrostatic repulsion only at the lowest surface charges, which is important for the interpretation of experimental data.

Nanoscopic confinement also has dramatic effects on the viscous properties of water, which is relevant when hydrated surfaces in close contact are sheared against each other, for example in bio-lubrication applications. Experiments suggest an increased water viscosity, but interpretation of the experimental data is often difficult due to the fact that it remains unclear whether the linear regime with respect to the shear velocity is reached. Further, the mechanism of hydration layer friction is unclear. We study the shear friction between polar surfaces by extensive non-equilibrium molecular dynamics simulations in the linear-response regime at low shearing velocity, which is the relevant regime for typical biological applications. We show that an effective viscosity profile can be derived from momentum balance taking into account the fact that the local stress varies on lengthscales comparable to the variation of the local velocity, which enables the employment of the continuum expressions down to the molecular lengthscales. Decreasing the water film then reveals three distinct friction regimes, where in thick water slabs friction is governed by the bulk water viscosity. At separations of about a nanometer the highly viscous interfacial water layers dominate and increase the surface friction, while at the transition to the dry friction limit interfacial slip sets in. We finally construct a confinement-dependent friction model which accounts for the additive friction contributions from bulk-like water, interfacial water layers and interfacial slip and which is valid for arbitrary water film thickness.

In conclusion, we have established molecular simulations at controlled water chemical potential as a tool to extract microscopic information, which can be incorporated into standard continuum theoretical models. Non-local effects are correctly included in such models in terms of a suitably defined effective observable, as we have shown for the dielectric and viscous response functions. The interactions between surfaces in aqueous solution can then be analyzed step by step in terms of hydration, electrostatics, or frictional effects, where simulations allow us to study the contribution of each contribution separately. Thus this work contributes a significant step in understanding the interplay of different effects involved in surface–surface interactions across aqueous solutions.

Future work could be aimed at combining the interplay of ions in between charged surfaces and friction: Recent experiments show an extreme reduction of friction that is attributed to the hydration shells that surround charges in water [227]. We observe that the presence of surface charge and ions leads to an increase in the water slab width at a given load (Chapter 4). Simulations could lead to insights into the mechanism of the reduced friction that is observed in such systems and which is of high relevance in biologically lubricated systems. Further systems that could be analyzed using the employed simulation methods are charged surfactants and lipid systems, for which a multitude of experimental data is available. Controlling water chemical potentials is an elementary key in obtaining the surface–surface interactions in nano-confinement. A logical next step in this direction is to include salt at given chemical potential. In an ideal binary mixture the chemical potentials of water and salt are related via a Gibbs–Duhem relation, thus measuring the chemical potentials explicitly in bulk yields insights into the salt solution behavior. The interactions at controlled salt chemical potential then yield the possibility to study e.g. lipid systems in contact with a salt solution reservoir, which is the relevant physiological condition. A further point that builds upon the research conducted in this work include dielectric profiles in the presence of mobile ions. The parallel dielectric component can be obtained rather straightforwardly by subtracting the monopole contributions. However, for the perpendicular component the technical procedure is more involved as the static permittivity needs to be calculated from the frequency dependent dielectric response function, where the ionic currents need to be subtracted. For further progress in quantitative modeling of the hydration repulsion, lateral correlations might need to be taken into account, as proposed in Chapter 3. From atomistic simulations the lateral structure factor can be obtained and employed into the corresponding theoretical expressions. To conclude, this work constitutes a starting point for rich future work in different directions and the obtained molecular information will drastically improve quantitative modeling of experimental data.

A. Simulations at prescribed chemical potential

The computer simulation of interacting surfaces nowadays still is a challenging task, as the chemical potential of water needs to be considered explicitly [95–97]. In this appendix we first derive the equivalent osmotic pressure that is commonly used in experiments [53] and can also be evaluated in simulations once the water chemical potential is known. The precise measurement of a water chemical potential is numerically very demanding due to the molecular interactions that need to be considered and which we discuss in Appendix A.3. Simulations at controlled chemical potential can then be performed using the thermodynamic extrapolation method (TEM) [98], where either the box size L_z or the water number N_w can be adjusted. Finally, we discuss the pressure contribution due to internal stress, which needs to be considered when performing simulations with molecular restraints.

A.1. The Gibbs–Duhem relation for equivalent osmotic pressures

The Gibbs–Duhem equation for bulk water, $N_\mathrm{w}\,\mathrm{d}\mu = -S\mathrm{d}T + V\mathrm{d}\Pi$, evaluated at constant temperature yields

$$\left(\frac{\partial \mu}{\partial \Pi}\right)_T = \frac{V}{N_\mathrm{w}} = v_\mathrm{w}(\Pi). \tag{A.1}$$

From Eq. (A.1) the chemical potential difference between a bulk water reservoir at chemical potential μ_b and pressure Π_0 and water confined between two surfaces at interaction pressure Π follows as

$$\Delta\mu = \mu - \mu_\mathrm{b} = \int_{\Pi}^{\Pi_0} v_\mathrm{w}(\Pi')\,\mathrm{d}\Pi'. \tag{A.2}$$

In osmotic stress experiments, as well as in the corresponding simulations, the pressure is fixed by atmospheric conditions Π_0. Using that water is incompressible up to several kilobars [98] allows to define an equivalent osmotic pressure using the bulk water volume v_w^0 as

$$\Delta\Pi = \Pi - \Pi_0 = -\frac{\Delta\mu}{v_\mathrm{w}^0}. \tag{A.3}$$

While the bulk water volume can be measured directly in simulations, the accurate determination of chemical potentials is more involved and discussed in the next section.

A.2. Measurement of the chemical potential

In order to measure the chemical potential of water, μ, with an accuracy as high as $\delta\mu \approx 0.02\,k_\mathrm{B}T$, which, using Eq. (A.3) and the bulk water molecular volume $v_\mathrm{w}^0 = 0.0304\,\mathrm{nm}^3$, corresponds to a pressure resolution of $\delta\Pi \approx 10\,\mathrm{bar}$ at $T = 300\,\mathrm{K}$, we decompose μ into three contributions,

$$\mu(z) = k_BT \log \rho(z) + \mu_\mathrm{LJ}(z) + \mu_\mathrm{C}(z). \tag{A.4}$$

The first term is the ideal gas contribution, where $\rho(z)$ is the water mass density at position z. The other two terms correspond to the excess Lennard-Jones (LJ) and Coulomb contributions, respectively. In thermodynamic equilibrium, the total chemical potential μ is independent of the position z, therefore it can be evaluated at an arbitrary position, which we chose in the center of the water slab between the surfaces.

A SPC/E water molecule consists of a single LJ interaction site only, therefore it is convenient to evaluate μ_LJ via the Widom Test Particle Insertion method (TPI) [228]. Most simulation packages provide corresponding routines to perform these insertions conveniently, or can be easily adapted [229]. Including the water partial charges, however, leads to drastic convergence problems, see Ref. [xiii]. The density can directly be obtained from the trajectory and is basically free of statistical errors for sufficient sampling. Confidence intervals $\delta\mu_\mathrm{LJ}$ are determined from the trajectory using bayesian estimators for the standard error [230]. For the three Coulomb interaction sites of a water molecule we evaluate the free energy difference between a neutral water molecule without any partial charges and a fully charged water molecule using a modified Hamiltonian approach [89, 90]. The electrostatic chemical potential μ_C is then estimated using the MBAR method [161], yielding results consistent with thermodynamic integration, but contrary to this method, where reliable error estimates are hard to obtain, it naturally provides the lowest variance estimator. To obtain estimates for μ_C with an accuracy in the order of $0.01k_\mathrm{B}T$ we perform 18 simulations at different values of the coulomb coupling parameter λ, in steps of 0.075 for $0 \leq \lambda \leq 0.45$ and then in steps of 0.05 for $0.45 \leq \lambda \leq 1$. Each λ-value is typically sampled for 100 ns, thus including the TPI the total sampling time per data point accumulates to about $2\,\mu$s.

A.3. Adjustment of the chemical potential in simulations

A.3.1. Adjustment of the particle number

We ajdust the chemical potential μ in our simulations at fixed box volume $V = AL_z$ via changing the number of water molecules N_w. At fixed temperature T, lateral area A and box height L_z and upon change of N_w, the normal pressure Π and the chemical potential μ vary as

$$\mathrm{d}\Pi = \left(\frac{\partial \Pi}{\partial N_\mathrm{w}}\right)_{A,L_z} \mathrm{d}N_\mathrm{w} \quad \text{and} \quad \mathrm{d}\mu = \left(\frac{\partial \mu}{\partial N_\mathrm{w}}\right)_{A,L_z} \mathrm{d}N_\mathrm{w}, \tag{A.5}$$

where we dropped the temperature dependence. Eliminating $\mathrm{d}N_\mathrm{w}$ from the latter relations yields

$$d\Pi = \left(\frac{\partial \Pi}{\partial N_\mathrm{w}}\right)_{A,L_z} \left(\frac{\partial N_\mathrm{w}}{\partial \mu}\right)_{A,L_z} \mathrm{d}\mu = \left(\frac{\partial \Pi}{\partial \mu}\right)_{A,L_z} \mathrm{d}\mu \tag{A.6}$$

revealing a relationship between the change of the normal pressure and the change in the chemical potential. The proportionality factor is the inverse partial water volume v_w,

$$\left(\frac{\partial \Pi}{\partial \mu}\right)_{A,L_z} \equiv v_\mathrm{w}^{-1}. \tag{A.7}$$

The partial water volume at given box length L_z can correspondingly be determined from the slope $\partial\mu/\partial\Pi$ at a fixed height of the simulation box L_z by varying the water number N_w. An alternative way to evaluate v_w can be derived from a Maxwell relation considering the total differential of the grand-canonical potential Ω at fixed A and T,

$$\mathrm{d}\Omega = -\Pi A \mathrm{d}L_z - N_\mathrm{w}\mathrm{d}\mu. \tag{A.8}$$

We obtain

$$\frac{\partial^2 \Omega}{\partial L_z \partial \mu} = \left(-\frac{\partial \Pi}{\partial \mu}\right)_{L_z} A, \tag{A.9}$$

where we used that the lateral area A is constant. Alternatively, we can write

$$\frac{\partial^2 \Omega}{\partial \mu \partial L_z} = \left(-\frac{\partial N_\mathrm{w}}{\partial L_z}\right)_{\mu}. \tag{A.10}$$

From Eqs. (A.9), (A.10) and (A.7) we thus obtain

$$v_\mathrm{w} = \left(\frac{\partial L_z}{\partial N_\mathrm{w}}\right)_{A,\mu} A, \tag{A.11}$$

which we evaluate from the simulation data for a given value of L_z by varying N_w and interpolation. Figure A.1 compares the partial water volume obtained from Eqs. (A.7) and (A.11). The values of v_w for $d_\mathrm{w} > 0.5\,\mathrm{nm}$ agree nicely among each other and also with the SPC/E bulk value $v_\mathrm{w}^0 = V/N_\mathrm{w} = 0.0304\,\mathrm{nm}^3$, which has been determined independently from bulk water simulations. At smaller separations the partial water volume v_w increases significantly and satisfactory agreement is obtained for the both methods, Eqs. (A.7) and (A.11).

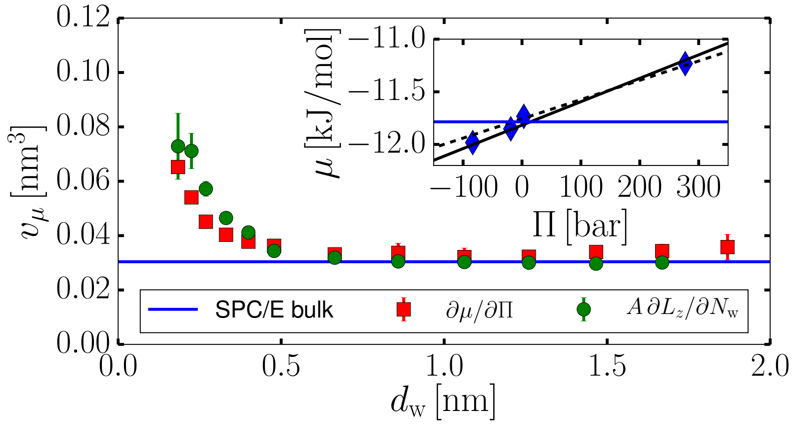

Figure A.1.: **Partial water volume.** The partial volumes are determined via Eq. (A.7) (red squares) and Eq. (A.11) (green circles), respectively. The inset shows exemplary data at $d_\mathrm{w} = 1.47\,\mathrm{nm}$ and the fit used for determination of the water partial volume via Eq. (A.7) (solid line). The dashed line indicates the slope according to the bulk water partial volume, the horizontal blue line in the inset shows the corresponding bulk chemical potential.

As follows from Eq. (A.7), the pressure $\Pi(\mu_0)$ at the desired chemical potential μ_0 can be evaluated from the measured $\Pi(\mu)$ and μ via linear extrapolation,

$$\Pi(\mu_0) = \Pi(\mu) + \frac{\mu_0 - \mu}{v_\mathrm{w}}, \tag{A.12}$$

which is equivalent to direct extrapolation of the pressure $\Pi(N_\mathrm{w})$ as a function of the water number N_w, where N_w is extrapolated itself such that $\mu = \mu_\mathrm{b}$.

In general, the value v_w is not a priori known, therefore, in order to evaluate the interaction pressure at given surface separation from Eq. (A.12), at least two simulations with different N_w at fixed L_z have to be performed. The inset of Fig. A.1 shows an example for μ as a function of the pressure Π at $d_\mathrm{w} = 1.47\,\mathrm{nm}$. In our simulation protocol, for production runs the number of water molecules $N_\mathrm{w}(\mu_0)$ at bulk chemical potential is obtained by linear extrapolation from the measured chemical potentials.

A.3.2. Adjustment of the box volume

It is also possible to adjust the chemical potential by changing the volume AL_z of the simulation box and leaving the number of water molecules unchanged, which is often quicker than adjusting N_w. However, when positional restraints are present in the simulations, as in the case for Decanol in this work, care has to be taken in order to correctly scale the reference coordinates: For the positional restraints as employed in Chapter 5, there is no unique way of scaling the restraint positions without imposing an additional internal stress. In Sections 2.6.2 and 4.3.1 we compare both approaches for the Decanol surfaces and find numerical equivalence.

When the lateral area A is kept fixed and only the length in normal direction L_z is changed, the dependent quantities are

$$\mathrm{d}\Pi = \left(\frac{\partial \Pi}{\partial L_z}\right)_{A,N_\mathrm{w}} \mathrm{d}L_z \quad \text{and} \quad \mathrm{d}\mu = \left(\frac{\partial \mu}{\partial L_z}\right)_{A,N_\mathrm{w}} \mathrm{d}L_z \tag{A.13}$$

Eliminating L_z from both relations this yields

$$\begin{aligned} d\mu &= \left(\frac{\partial \mu}{\partial L_z}\right)_{A,N_\mathrm{w}} \left(\frac{\partial L_z}{\partial \Pi}\right)_{A,N_\mathrm{w}} \mathrm{d}\Pi & \text{(A.14)} \\ &= \left(\frac{\partial \mu}{\partial \Pi}\right)_{A,N_\mathrm{w}} \mathrm{d}\Pi = v_\mathrm{w}\mathrm{d}\Pi, & \text{(A.15)} \end{aligned}$$

In this case we obtain a relationship between the changes in Π and μ, but this time the proportionality factor is the partial water volume at given pressure Π, and if the reservoir is at atmospheric conditions Π_0 Eq. (A.3) is recovered,

$$\left(\frac{\partial \mu}{\partial \Pi}\right)_{A,N_\mathrm{w}} = \left(\frac{\partial L_z}{\partial N_\mathrm{w}}\right)_{A,\Pi_0} \equiv v_\mathrm{w}^0. \tag{A.16}$$

The water volume at constant pressure is technically simple to evaluate from MD simulations and at ambient pressure $\Pi_0 = 1\,\mathrm{bar}$ is $v_\mathrm{w}^0 = 0.0304\,\mathrm{nm}$ in bulk. The interaction pressure can thus be extrapolated linearly as

$$\Pi(\mu_0) = \Pi_0 + \frac{\mu_0 - \mu}{v_\mathrm{w}^0}. \tag{A.17}$$

This procedure is computationally advantageous since the water volume v_w^0 is constant for all separations and does not need to be determined separately.

A.4. Interaction pressure with internal stress due to restraints

When imposing position restraints to molecules as done in our simulations, we impose an internal stress. In order to see this more clearly, we consider the Hamiltonian in which we introduce a harmonic position restraint acting on particle i at reference position z_0,

$$\mathcal{H} = \sum_i \left(\frac{\mathbf{q}_i^2}{2m} + V_i(\mathbf{r}_1, \ldots, \mathbf{r}_N) + \frac{1}{2} k (z_i - z_0)^2 \right), \tag{A.18}$$

where $\mathbf{r}_i$ and $\mathbf{q}_i$ are the position and momentum of particle i, respectively. The virial is computed from the simulation trajectory according to

$$\overleftrightarrow{\xi} = - \sum_{i<j}^{N} \frac{1}{2} \mathbf{r}_{ij} \otimes \mathbf{F}_{ij}, \tag{A.19}$$

where $\mathbf{F}_{ij}$ denotes the force acting between particles i and j at distance $\mathbf{r}_{ij}$. The pressure in z-direction follows from

$$\Pi = \left\langle \frac{2}{3V} \left(E_{\mathrm{kin},z} - \xi_{zz} \right) \right\rangle, \tag{A.20}$$

where $E_{\mathrm{kin},z} = \sum_i m v_{i,z}^2 / 2$ is the kinetic energy in z-direction. If the restrained particle i has no further interactions with other particles, the corresponding contribution of the restraint potential to the pressure follows from Eqs. (A.18) to (A.20) and using $F_{i0} = -k(z_i - z_0)$ and $r_{i0} = (z_i - z_0)$ as $-k\left(z_i - z_0\right)^2/2$. This allows us to compute the expectation value of the pressure due to the restraint using the equipartition theorem $\frac{1}{2} k_B T = \left\langle \frac{1}{2} k \left(z_i - z_0\right)^2 \right\rangle$ as

$$\Delta\Pi = -\frac{k_\mathrm{B} T}{3V}. \tag{A.21}$$

At 300 K in a typical simulation box of $(5\,\mathrm{nm})^3$ this corresponds to a contribution of about 0.1 bar per restraint in one direction. The expected pressure shift due to the positional restraints for the Decanol system as employed in Chapters 2 to 4, where one restraint per molecule acts in z-direction, thus is $\Delta\Pi \approx -20\,\mathrm{bar}$. In our simulation setup employed in Chapter 5, where stronger restraints are necessary to stabilize the system under shear, we impose 4 restraints per Decanol in z-direction. Accordingly for 200 molecules this predicts a pressure contribution of $\Delta\Pi \approx -80\,\text{bar}$ in the ideal limit.

However, the result in Eq. (A.21) only holds if the particle i is decoupled from all other particles. Due to intramolecular interactions and the influence of neighboring molecules, we expect deviations from this situation. Therefore we perform reruns of the trajectories with restraints present, where now we turn off the restraining potential to determine $\Delta\Pi$. At large separations, where the surfaces do not interact, the difference in the pressure corresponds to the contribution of the restraint potentials. Figure A.2 shows the corresponding pressure shift, which for large separations follows as $\Delta\Pi = +16 \pm 1\,\text{bar}$ for the system used in Chapters 2 to 4, shown as green line in Fig. A.2. For the setup employed in Chapter 5 we obtain $\Delta\Pi = -74 \pm 2\,\text{bar}$, shown as solid red line, and which is in good agreement with our simple estimate in Eq. (A.21). In all reported pressures Π we subtract the constant pressure at large separations, $\Delta\Pi$, which is shown to be due to the combination of the virial pressure calculation with constraint potentials.

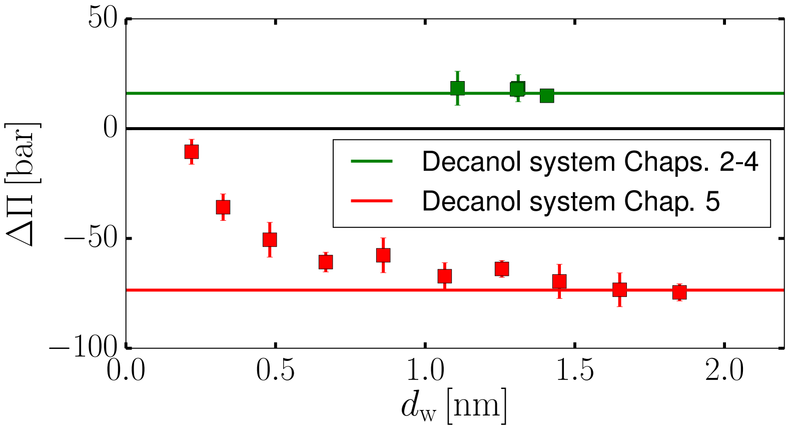

Figure A.2.: **Pressure shift due to internal stress caused by restraints.** Data shows the pressure difference between simulations with restraints and reruns of the same trajectories but with restraints turned off. The solid line denotes the pressure shift at large separations.

List of Figures

List of Tables

List of Publications

The present thesis is based on the following manuscripts, which have been published or are in preparation for publication in peer-reviewed journals:

[i] Alexander Schlaich, Ernst W. Knapp and Roland. R. Netz, “Water Dielectric Effects in Planar Confinement,” *Phys. Rev. Lett.*, vol. 117, no. 4, p. 48001, **2016**. DOI: 10.1103/PhysRevLett.117.048001

[ii] Matej Kanduč, Alexander Schlaich, Emanuel Schneck, and Roland R. Netz, “Hydration repulsion between membranes and polar surfaces: Simulation approaches versus continuum theories,” *Advances in Colloid and Interface Science*, vol. 208, pp. 142–152, **2014**. DOI: 10.1016/j.cis.2014.02.001

[iii] Alexander Schlaich, Bartosz Kowalik, Matej Kanduč, Emanuel Schneck, and Roland R. Netz, “Physical mechanisms of the interaction between lipid membranes in the aqueous environment,” *Physica A: Statistical Mechanics and its Applications*, vol. 418, pp. 105–125, **2015**. DOI:10.1016/j.physa.2014.06.088

[iv] Alexander Schlaich, Jan O. Daldrop, Bartosz Kowalik, Matej Kanduč, Emanuel Schneck, and Roland R. Netz, ”Landau Ginzburg theory for membrane interactions”, *in preparation.*

[v] Alexander Schlaich and Roland R. Netz, ”Non-additivity of hydration and electrostatic forces due to ion-specificity”, *in preparation.*

[vi] Alexander Schlaich, Julian Kappler, and Roland R. Netz, ”Hydration friction in nano-confinement:from bulk via interfacial to dry friction”, *Nano Letters*, vol. 17, no. 10, pp 5969–5976, **2017**. DOI: 10.1021/acs.nanolett.7b02000

Publications not discussed within this thesis

[vii] Bartosz Kowalik, Alexander Schlaich, Matej Kanduč, Emanuel Schneck, and Roland R. Netz, ”Hydration Repulsion Difference Between Ordered and Disordered Membranes Due to Cancellation of Membrane-Membrane and Water-Mediated Interactions”, *J. Phys. Chem. Lett.* 8, 2869–2874, **2017**. DOI:10.1021/acs.jpclett.7b00977

[viii] Matej Kanduč, Alexander Schlaich, Alex H. de Vries, Juliette Jouhet, Eric Maréchal, Bruno Demé, Roland R. Netz, and Emanuel Schneck, “Tight cohesion between glycolipid membranes results from balanced water–headgroup interactions,” *Nature Communications*, vol. 8, p. 14899, **2017**. DOI: 10.1038/ncomms14899

[ix] Matej Kanduč, Alexander Schlaich, Emanuel Schneck, and Roland R. Netz, “Water-Mediated Interactions between Hydrophilic and Hydrophobic Surfaces,” *Langmuir*, vol. 32, no. 35, pp. 8767–8782, **2016**. DOI: 10.1021/acs.langmuir.6b01727

Manuscripts in preparation

[x] Bernhard Irsigler, Alexander Schlaich, Anirudh Gupta, and Roland R. Netz ”Effective Interactions between Charged Surfaces in the Presence of Ion-Specific Surface Adsorption: Poisson-Boltzmann Theory and the Influence of Additivity”.

[xi] Philip Loche, Cihan Ayaz, Alexander Schlaich, and Roland R. Netz, ”Giant dielectric axial response in aqueous water channels”.

[xii] Julius C. F. Schulz, Alexander Schlaich, Matthias Heyden, Roland R. Netz, and Julian Kappler, ”Non-Newtonian behavior of water at high frequencies”.

Book chapters

[xiii] Alexander Schlaich, Bartosz Kowalik, Matej Kanduč, Emanuel Schneck, and Roland R. Netz, “Simulation Techniques for Solvation-Induced Surface-Interactions at Prescribed Water Chemical Potential,” in *Computational Trends in Solvation and Transport in Liquids*, vol. 28, Godehard Sutmann, Johannes Grotendorst, Gerhard Gompper, and Dominik Marx, Eds. Jülich: Forschungszentrum Jülich GmbH, **2015**, pp. 155–185.

[xiv] Matej Kanduč, Alexander Schlaich, Emanuel Schneck, and Roland R. Netz, “Interactions between biological membranes: Theoretical concepts,” in *Soft Interfaces*, Lydéric Bocquet, David Quéré, Thomas A. Witten, and Leticia F. Cugliandolo, Eds. Oxford: Oxford University Press, **2012**.

Bibliography

[1] P. Ball, "Water is an active matrix of life for cell and molecular biology," *Proceedings of the National Academy of Sciences*, p. 201703781, **2017**. DOI: 10.1073/pnas.1703781114

[2] M. Nosonovsky and B. Bhushan, "Green tribology: principles, research areas and challenges," *Philosophical Transactions of the Royal Society of London A: Mathematical, Physical and Engineering Sciences*, vol. 368, no. 1929, pp. 4677–4694, **2010**. DOI: 10.1098/rsta.2010.0200

[3] B. E. Viani, P. F. Low, and C. B. Roth, "Direct measurement of the relation between interlayer force and interlayer distance in the swelling of montmorillonite," *Journal of Colloid and Interface Science*, vol. 96, no. 1, pp. 229–244, **1983**. DOI: 10.1016/0021-9797(83)90025-5

[4] J. S. Clunie, J. F. Goodman, and P. C. Symons, "Solvation Forces in Soap Films," *Nature*, vol. 216, no. 5121, pp. 1203–1204, **1967**. DOI: 10.1038/2161203a0

[5] E. Smulders, W. von Rybinski, E. Sung, W. Rähse, J. Steber, F. Wiebel, and A. Nordskog, "Laundry Detergents," in *Ullmann's Encyclopedia of Industrial Chemistry.* Wiley-VCH Verlag GmbH & Co. KGaA, 2000, dOI: 10.1002/14356007.a08_315.pub2.

[6] D. M. Leneveu, R. P. Rand, and V. A. Parsegian, "Measurement of forces between lecithin bilayers," *, Published online: 19 February 1976; | doi:10.1038/259601a0*, vol. 259, no. 5544, pp. 601–603, **1976**. DOI: 10.1038/259601a0

[7] L. Lis, M. McAlister, N. Fuller, R. Rand, and V. Parsegian, "Interactions between neutral phospholipid bilayer membranes." *Biophysical journal*, vol. 37, no. 3, p. 657, **1982**.

[8] D. E. Green and A. Tzagoloff, "Role of lipids in the structure and function of biological membranes," *Journal of Lipid Research*, vol. 7, no. 5, pp. 587–602, **1966**.

[9] J. T. Duniec, J. N. Israelachvili, B. W. Ninham, R. M. Pashley, and S. W. Thorne, "An ion-exchange model for thylakoid stacking in chloroplasts," *FEBS Letters*, vol. 129, no. 2, pp. 193–196, **1981**. DOI: 10.1016/0014-5793(81)80163-9

[10] F. S. Cohen, M. H. Akabas, and A. Finkelstein, “Osmotic swelling of phospholipid vesicles causes them to fuse with a planar phospholipid bilayer membrane,” *Science*, vol. 217, no. 4558, pp. 458–460, **1982**.

[11] A. Finkelstein, J. Zimmerberg, and F. S. Cohen, “Osmotic swelling of vesicles: its role in the fusion of vesicles with planar phospholipid bilayer membranes and its possible role in exocytosis.” *Annual review of physiology*, vol. 48, pp. 163–174, **1986**. DOI: 10.1146/annurev.ph.48.030186.001115

[12] J. T. G. Overbeek, “Colloid stability in aqueous and non-aqueous media. Introductory paper,” *Discussions of the Faraday Society*, vol. 42, no. 0, pp. 7–13, **1966**. DOI: 10.1039/DF9664200007

[13] M. M. Teeter, “Water-Protein Interactions: Theory and Experiment,” *Annual Review of Biophysics and Biophysical Chemistry*, vol. 20, no. 1, pp. 577–600, **1991**. DOI: 10.1146/annurev.bb.20.060191.003045

[14] D. J. Selkoe, “Folding proteins in fatal ways,” *Nature*, vol. 426, no. 6968, pp. 900–904, **2003**. DOI: 10.1038/nature02264

[15] G. S. Roth, J. A. Joseph, and R. Preston Mason, “Membrane alterations as causes of impaired signal transduction in Alzheimer’s disease and aging,” *Trends in Neurosciences*, vol. 18, no. 5, pp. 203–206, **1995**. DOI: 10.1016/0166-2236(95)93902-A

[16] D. T. Woodley, R. A. Briggaman, E. J. O’Keefe, A. O. Inman, L. L. Queen, and W. R. Gammon, “Identification of the Skin Basement-Membrane Autoantigen in Epidermolysis Bullosa Acquisita,” *New England Journal of Medicine*, vol. 310, no. 16, pp. 1007–1013, **1984**. DOI: 10.1056/NEJM198404193101602

[17] G. van Meer, D. R. Voelker, and G. W. Feigenson, “Membrane lipids: where they are and how they behave,” *Nature Reviews Molecular Cell Biology*, vol. 9, no. 2, pp. 112–124, **2008**. DOI: 10.1038/nrm2330

[18] H. Wang and G. A. Ateshian, “The normal stress effect and equilibrium friction coefficient of articular cartilage under steady frictional shear,” *Journal of Biomechanics*, vol. 30, no. 8, pp. 771–776, **1997**. DOI: 10.1016/S0021-9290(97)00031-6

[19] N. Y. C. Lin, B. M. Guy, M. Hermes, C. Ness, J. Sun, W. C. K. Poon, and I. Cohen, “Hydrodynamic and Contact Contributions to Continuous Shear Thickening in Colloidal Suspensions,” *Physical Review Letters*, vol. 115, no. 22, p. 228304, **2015**. DOI: 10.1103/PhysRevLett.115.228304

[20] B. W. Ninham, “Long-range vs. short-range forces. The present state of play,” *The Journal of Physical Chemistry*, vol. 84, no. 12, pp. 1423–1430, **1980**. DOI: 10.1021/j100449a001

[21] B. Derjaguin, “Untersuchungen über die Reibung und Adhäsion, IV,” *Kolloid-Zeitschrift*, vol. 69, no. 2, pp. 155–164, **1934**. DOI: 10.1007/BF01433225

[22] L. Landau, “Zur Theorie der phasenumwandlungen II,” *Phys. Z. Sowjetunion*, vol. 11, pp. 26–35, **1937**.

[23] E. J. W. Verwey, J. T. G. Overbeek, and K. Van Nes, *Theory of the stability of lyophobic colloids: the interaction of sol particles having an electric double layer.* Elsevier New York, 1948.

[24] D. Grasso, K. Subramaniam, M. Butkus, K. Strevett, and J. Bergendahl, “A review of non-DLVO interactions in environmental colloidal systems,” *Reviews in Environmental Science and Biotechnology*, vol. 1, no. 1, pp. 17–38, **2002**. DOI: 10.1023/A:1015146710500

[25] B. W. Ninham, “On progress in forces since the DLVO theory,” *Advances in Colloid and Interface Science*, vol. 83, no. 1–3, pp. 1–17, **1999**. DOI: 10.1016/S0001-8686(99)00008-1

[26] H. Casimir, “On the attraction between two perfectly conducting plates,” in *Proc. K. Ned. Akad. Wet*, vol. 51, 1948, p. 793.

[27] J. F. Mahanty and B. W. Ninham, *Dispersion Forces.* London-New York-San Francisco: Academic Press, 1976, vol. 81.

[28] V. A. Parsegian, *Van der Waals Forces: A Handbook for Biologists, Chemists, Engineers, and Physicists.* Cambridge University Press, 2005.

[29] R. H. French, V. A. Parsegian, R. Podgornik, R. F. Rajter, A. Jagota, J. Luo, D. Asthagiri, M. K. Chaudhury, Y.-m. Chiang, S. Granick, S. Kalinin, M. Kardar, R. Kjellander, D. C. Langreth, J. Lewis, S. Lustig, D. Wesolowski, J. S. Wettlaufer, W.-Y. Ching, M. Finnis, F. Houlihan, O. A. von Lilienfeld, C. J. van Oss, and T. Zemb, “Long range interactions in nanoscale science,” *Reviews of Modern Physics*, vol. 82, no. 2, pp. 1887–1944, **2010**.

[30] H. C. Hamaker, “The London—van der Waals attraction between spherical particles,” *Physica*, vol. 4, no. 10, pp. 1058–1072, **1937**. DOI: 10.1016/S0031-8914(37)80203-7

[31] R. Podgornik, R. H. French, and V. A. Parsegian, "Nonadditivity in van der Waals interactions within multilayers," *The Journal of Chemical Physics*, vol. 124, no. 4, p. 044709, **2006**. DOI: 10.1063/1.2150825

[32] W. Helfrich, "Steric Interaction of Fluid Membranes in Multilayer Systems," *Zeitschrift für Naturforschung A*, vol. 33, no. 3, pp. 305–315, **1978**. DOI: 10.1515/zna-1978-0308

[33] L. Peliti and S. Leibler, "Effects of Thermal Fluctuations on Systems with Small Surface Tension," *Physical Review Letters*, vol. 54, no. 15, pp. 1690–1693, **1985**. DOI: 10.1103/PhysRevLett.54.1690

[34] R. Lipowsky, "The conformation of membranes," *Nature*, vol. 349, no. 6309, pp. 475–481, **1991**. DOI: 10.1038/349475a0

[35] R. R. Netz and R. Lipowsky, "Stacks of Fluid Membranes under Pressure and Tension," *Europhysics Letters (EPL)*, vol. 29, no. 4, pp. 345–350, **1995**. DOI: 10.1209/0295-5075/29/4/013

[36] J. N. Israelachvili and H. Wennerström, "Role of hydration and water structure in biological and colloidal interactions," *Nature*, vol. 379, no. 6562, pp. 219–225, **1996**. DOI: 10.1038/379219a0

[37] H. Wennerström and E. Sparr, "Thermodynamics of membrane lipid hydration," *Pure and Applied Chemistry*, vol. 75, no. 7, pp. 905–912, **2009**. DOI: 10.1351/pac200375070905

[38] J. N. Israelachvili and H. Wennerström, "Hydration or steric forces between amphiphilic surfaces?" *Langmuir*, vol. 6, no. 4, pp. 873–876, **1990**. DOI: 10.1021/la00094a028

[39] J. N. Israelachvili and H. Wennerström, "Entropic forces between amphiphilic surfaces in liquids," *The Journal of Physical Chemistry*, vol. 96, no. 2, pp. 520–531, **1992**. DOI: 10.1021/j100181a007

[40] V. A. Parsegian and R. P. Rand, "Interaction in Membrane Assemblies," *Handbook of Biological Physics*, vol. 1, pp. 643–690, **1995**. DOI: 10.1016/S1383-8121(06)80006-0

[41] S. Marčelja and N. Radić, "Repulsion of interfaces due to boundary water," *Chemical Physics Letters*, vol. 42, no. 1, pp. 129–130, **1976**. DOI: 10.1016/0009-2614(76)80567-2

[42] G. Cevc, R. Podgornik, and B. Žekš, "The free energy,enthalpy and entropy of hydration of phospholipid bilayer membranes and their difference on the interfacial separation," *Chemical Physics Letters*, vol. 91, no. 3, pp. 193–196, **1982**. DOI: 10.1016/0009-2614(82)83639-7

[43] P. A. Bopp, A. A. Kornyshev, and G. Sutmann, "Static Nonlocal Dielectric Function of Liquid Water," *Physical Review Letters*, vol. 76, no. 8, pp. 1280–1283, **1996**. DOI: 10.1103/PhysRevLett.76.1280

[44] D. J. Bonthuis, S. Gekle, and R. R. Netz, "Dielectric Profile of Interfacial Water and its Effect on Double-Layer Capacitance," *Physical Review Letters*, vol. 107, no. 16, p. 166102, **2011**. DOI: 10.1103/PhysRevLett.107.166102

[45] D. J. Bonthuis and R. R. Netz, "Unraveling the Combined Effects of Dielectric and Viscosity Profiles on Surface Capacitance, Electro-Osmotic Mobility, and Electric Surface Conductivity," *Langmuir*, vol. 28, no. 46, pp. 16 049–16 059, **2012**. DOI: 10.1021/la3020089

[46] Y. Uematsu, R. R. Netz, and D. J. Bonthuis, "Power-law electrokinetic behavior as a direct probe of effective surface viscosity," *Chemical Physics Letters*, vol. 670, pp. 11–15, **2016**.

[47] R. M. Pashley, "DLVO and hydration forces between mica surfaces in Li+, Na+, K+, and Cs+ electrolyte solutions: A correlation of double-layer and hydration forces with surface cation exchange properties," *Journal of Colloid and Interface Science*, vol. 83, no. 2, pp. 531–546, **1981**. DOI: 10.1016/0021-9797(81)90348-9

[48] J. N. Israelachvili, "Solvation forces and liquid structure, as probed by direct force measurements," *Accounts of Chemical Research*, vol. 20, no. 11, pp. 415–421, **1987**. DOI: 10.1021/ar00143a005

[49] R. G. Horn, D. T. Smith, and W. Haller, "Surface forces and viscosity of water measured between silica sheets," *Chemical Physics Letters*, vol. 162, no. 4, pp. 404–408, **1989**. DOI: 10.1016/0009-2614(89)87066-6

[50] R. Pashley, "Hydration forces between mica surfaces in aqueous electrolyte solutions," *Journal of Colloid and Interface Science*, vol. 80, no. 1, pp. 153–162, **1981**. DOI: 10.1016/0021-9797(81)90171-5

[51] J. N. Israelachvili and R. M. Pashley, "Molecular layering of water at surfaces and origin of repulsive hydration forces," *Nature*, vol. 306, no. 5940, pp. 249–250, **1983**. DOI: 10.1038/306249a0

[52] J. N. Israelachvili and G. Adams, "Measurement of forces between two mica surfaces in aqueous electrolyte solutions in the range 0–100 nm," *Journal of the Chemical Society, Faraday Transactions 1: Physical Chemistry in Condensed Phases*, vol. 74, pp. 975–1001, **1978**.

[53] V. Parsegian, N. Fuller, and R. Rand, "Measured work of deformation and repulsion of lecithin bilayers," *Proceedings of the National Academy of Sciences*, vol. 76, no. 6, pp. 2750–2754, **1979**.

[54] R. Rand and V. Parsegian, "Hydration forces between phospholipid bilayers," *Biochimica et biophysica acta*, vol. 988, no. 3, pp. 351–376, **1989**.

[55] D. Marsh, "Water adsorption isotherms and hydration forces for lysolipids and diacyl phospholipids," *Biophysical Journal*, vol. 55, no. 6, pp. 1093–1100, **1989**. DOI: 10.1016/S0006-3495(89)82906-6

[56] C. Stanley and D. C. Rau, "Evidence for water structuring forces between surfaces," *Current Opinion in Colloid & Interface Science*, vol. 16, no. 6, pp. 551–556, **2011**. DOI: 10.1016/j.cocis.2011.04.010

[57] I. Langmuir, "The Role of Attractive and Repulsive Forces in the Formation of Tactoids, Thixotropic Gels, Protein Crystals and Coacervates," *The Journal of Chemical Physics*, vol. 6, no. 12, pp. 873–896, **1938**. DOI: 10.1063/1.1750183

[58] V. Parsegian and T. Zemb, "Hydration forces: Observations, explanations, expectations, questions," *Current Opinion in Colloid & Interface Science*, vol. 16, no. 6, pp. 618–624, **2011**. DOI: 10.1016/j.cocis.2011.06.010

[59] S. Suetsugu, S. Kurisu, and T. Takenawa, "Dynamic Shaping of Cellular Membranes by Phospholipids and Membrane-Deforming Proteins," *Physiological Reviews*, vol. 94, no. 4, pp. 1219–1248, **2014**. DOI: 10.1152/physrev.00040.2013

[60] P. A. Leventis and S. Grinstein, "The Distribution and Function of Phosphatidylserine in Cellular Membranes," *Annual Review of Biophysics*, vol. 39, no. 1, pp. 407–427, **2010**. DOI: 10.1146/annurev.biophys.093008.131234

[61] G. Di Paolo and P. De Camilli, "Phosphoinositides in cell regulation and membrane dynamics," *Nature*, vol. 443, no. 7112, pp. 651–657, **2006**. DOI: 10.1038/nature05185

[62] O. Stern, "Zur Theorie Der Elektrolytischen Doppelschicht," *Zeitschrift für Elektrochemie und angewandte physikalische Chemie*, vol. 30, no. 21-22, pp. 508–516, **1924**. DOI: 10.1002/bbpc.192400182

[63] J. Lyklema and M. Minor, "On surface conduction and its role in electrokinetics," *Colloids and Surfaces A: Physicochemical and Engineering Aspects*, vol. 140, no. 1–3, pp. 33–41, **1998**. DOI: 10.1016/S0927-7757(97)00266-5

[64] L. Herrmann, A. Johner, and P. Kékicheff, "Interactions between Charged Lamellae in Aqueous Solution," *Physical Review Letters*, vol. 113, no. 26, p. 268302, **2014**. DOI: 10.1103/PhysRevLett.113.268302

[65] A. Abrashkin, D. Andelman, and H. Orland, "Dipolar Poisson-Boltzmann Equation: Ions and Dipoles Close to Charge Interfaces," *Physical Review Letters*, vol. 99, no. 7, p. 077801, **2007**. DOI: 10.1103/PhysRevLett.99.077801

[66] S. Buyukdagli, M. Manghi, and J. Palmeri, "Variational approach for electrolyte solutions: From dielectric interfaces to charged nanopores," *Physical Review E*, vol. 81, no. 4, p. 041601, **2010**. DOI: 10.1103/PhysRevE.81.041601

[67] V. Jadhao, F. J. Solis, and M. O. de la Cruz, "Simulation of Charged Systems in Heterogeneous Dielectric Media via a True Energy Functional," *Physical Review Letters*, vol. 109, no. 22, p. 223905, **2012**. DOI: 10.1103/PhysRevLett.109.223905

[68] G. Gouy, "Constitution of the electric charge at the surface of an electrolyte," *J. phys*, vol. 9, no. 4, pp. 457–467, **1910**.

[69] D. L. Chapman, "A contribution to the theory of electrocapillarity," *The London, Edinburgh, and Dublin Philosophical Magazine and Journal of Science*, vol. 25, no. 148, p. 475, **1913**. DOI: 10.1080/14786440408634187

[70] R. R. Netz, "Electrostatistics of counter-ions at and between planar charged walls: From Poisson-Boltzmann to the strong-coupling theory," *The European Physical Journal E*, vol. 5, no. 1, pp. 557–574, **2001**. DOI: 10.1007/s101890170039

[71] A. G. Moreira and R. R. Netz, "Binding of Similarly Charged Plates with Counterions Only," *Physical Review Letters*, vol. 87, no. 7, p. 078301, **2001**. DOI: 10.1103/PhysRevLett.87.078301

[72] T. J. McIntosh, A. D. Magid, and S. A. Simon, "Interactions between charged, uncharged, and zwitterionic bilayers containing phosphatidylglycerol." *Biophysical Journal*, vol. 57, no. 6, pp. 1187–1197, **1990**.

[73] V. A. Parsegian, R. P. Rand, and N. L. Fuller, "Direct osmotic stress measurements of hydration and electrostatic double-layer forces between bilayers of double-chained

ammonium acetate surfactants," *The Journal of Physical Chemistry*, vol. 95, no. 12, pp. 4777–4782, **1991**. DOI: 10.1021/j100165a034

[74] M. Dubois, T. Zemb, N. Fuller, R. P. Rand, and V. A. Parsegian, "Equation of state of a charged bilayer system: Measure of the entropy of the lamellar–lamellar transition in DDABr," *The Journal of Chemical Physics*, vol. 108, no. 18, pp. 7855–7869, **1998**. DOI: 10.1063/1.476505

[75] M. Dubois, M. Schönhoff, A. Meister, L. Belloni, T. Zemb, and H. Möhwald, "Equation of state of colloids coated by polyelectrolyte multilayers," *Physical Review E*, vol. 74, no. 5, p. 051402, **2006**. DOI: 10.1103/PhysRevE.74.051402

[76] N. Schwierz and R. R. Netz, "Effective Interaction between Two Ion-Adsorbing Plates: Hofmeister Series and Salting-In/Salting-Out Phase Diagrams from a Global Mean-Field Analysis," *Langmuir*, vol. 28, no. 8, pp. 3881–3886, **2012**. DOI: 10.1021/la204060k

[77] M. Urbakh and E. Meyer, "Nanotribology: The renaissance of friction," *Nature Materials*, vol. 9, no. 1, pp. 8–10, **2010**. DOI: 10.1038/nmat2599

[78] D. Y. C. Chan and R. G. Horn, "The drainage of thin liquid films between solid surfaces," *The Journal of Chemical Physics*, vol. 83, no. 10, pp. 5311–5324, **1985**. DOI: 10.1063/1.449693

[79] J. N. Israelachvili, "Measurement of the viscosity of liquids in very thin films," *Journal of Colloid and Interface Science*, vol. 110, no. 1, pp. 263–271, **1986**. DOI: 10.1016/0021-9797(86)90376-0

[80] U. Raviv, P. Laurat, and J. Klein, "Fluidity of water confined to subnanometre films," *Nature*, vol. 413, no. 6851, pp. 51–54, **2001**. DOI: 10.1038/35092523

[81] D. Ortiz-Young, H.-C. Chiu, S. Kim, K. Voïtchovsky, and E. Riedo, "The interplay between apparent viscosity and wettability in nanoconfined water," *Nature Communications*, vol. 4, p. 2482, **2013**. DOI: 10.1038/ncomms3482

[82] Y. Zhu and S. Granick, "Viscosity of Interfacial Water," *Physical Review Letters*, vol. 87, no. 9, p. 096104, **2001**. DOI: 10.1103/PhysRevLett.87.096104

[83] M. Antognozzi, A. D. L. Humphris, and M. J. Miles, "Observation of molecular layering in a confined water film and study of the layers viscoelastic properties," *Applied Physics Letters*, vol. 78, no. 3, pp. 300–302, **2001**. DOI: 10.1063/1.1339997

[84] B. Pittenger, S. C. Fain, M. J. Cochran, J. M. K. Donev, B. E. Robertson, A. Szuchmacher, and R. M. Overney, "Premelting at ice-solid interfaces studied via velocity-dependent indentation with force microscope tips," *Physical Review B*, vol. 63, no. 13, p. 134102, **2001**. DOI: 10.1103/PhysRevB.63.134102

[85] H. I. Kim, J. G. Kushmerick, J. E. Houston, and B. C. Bunker, "Viscous "Interphase" Water Adjacent to Oligo(ethylene glycol)-Terminated Monolayers," *Langmuir*, vol. 19, no. 22, pp. 9271–9275, **2003**. DOI: 10.1021/la034585x

[86] J. Marra and J. N. Israelachvili, "Direct measurements of forces between phosphatidylcholine and phosphatidylethanolamine bilayers in aqueous electrolyte solutions," *Biochemistry*, vol. 24, no. 17, pp. 4608–4618, **1985**. DOI: 10.1021/bi00338a020

[87] J. N. Israelachvili, *Intermolecular and Surface Forces.* London: Academic, 1992.

[88] T. J. McIntosh, A. D. Magid, and S. A. Simon, "Steric repulsion between phosphatidylcholine bilayers," *Biochemistry*, vol. 26, no. 23, pp. 7325–7332, **1987**. DOI: 10.1021/bi00397a020

[89] D. Frenkel and B. Smit, *Understanding Molecular Simulation: From Algorithms to Applications.* Academic Press, 2001.

[90] M. P. Allen and D. J. Tildesley, *Computer Simulation of Liquids.* Oxford University Press, 1989.

[91] H. J. C. Berendsen, J. R. Grigera, and T. P. Straatsma, "The missing term in effective pair potentials," *The Journal of Physical Chemistry*, vol. 91, no. 24, pp. 6269–6271, **1987**. DOI: 10.1021/j100308a038

[92] C. Oostenbrink, A. Villa, A. E. Mark, and W. F. Van Gunsteren, "A biomolecular force field based on the free enthalpy of hydration and solvation: The GROMOS force-field parameter sets 53A5 and 53A6," *Journal of Computational Chemistry*, vol. 25, no. 13, pp. 1656–1676, **2004**. DOI: 10.1002/jcc.20090

[93] O. Berger, O. Edholm, and F. Jähnig, "Molecular dynamics simulations of a fluid bilayer of dipalmitoylphosphatidylcholine at full hydration, constant pressure, and constant temperature," *Biophysical Journal*, vol. 72, no. 5, pp. 2002–2013, **1997**. DOI: 10.1016/S0006-3495(97)78845-3

[94] B. Kowalik, A. Schlaich, M. Kanduč, E. Schneck, and R. R. Netz, "Hydration Repulsion Difference between Ordered and Disordered Membranes Due to Cancellation of

Membrane–Membrane and Water-Mediated Interactions," *The Journal of Physical Chemistry Letters*, pp. 2869–2874, **2017**. DOI: 10.1021/acs.jpclett.7b00977

[95] C. Eun and M. L. Berkowitz, "Origin of the Hydration Force: Water-Mediated Interaction between Two Hydrophilic Plates," *The Journal of Physical Chemistry B*, vol. 113, no. 40, pp. 13 222–13 228, **2009**. DOI: 10.1021/jp901747s

[96] E. Schneck and R. R. Netz, "From simple surface models to lipid membranes: Universal aspects of the hydration interaction from solvent-explicit simulations," *Current Opinion in Colloid & Interface Science*, vol. 16, no. 6, pp. 607–611, **2011**. DOI: 10.1016/j.cocis.2011.04.007

[97] T. Hayashi, A. J. Pertsin, and M. Grunze, "Grand canonical Monte Carlo simulation of hydration forces between nonorienting and orienting structureless walls," *The Journal of Chemical Physics*, vol. 117, no. 13, pp. 6271–6280, **2002**. DOI: doi:10.1063/1.1504436

[98] E. Schneck, F. Sedlmeier, and R. R. Netz, "Hydration repulsion between biomembranes results from an interplay of dehydration and depolarization," *Proceedings of the National Academy of Sciences*, vol. 109, no. 36, pp. 14 405–14 409, **2012**. DOI: 10.1073/pnas.1205811109

[99] Q. Du, E. Freysz, and Y. R. Shen, "Vibrational spectra of water molecules at quartz/water interfaces," *Physical Review Letters*, vol. 72, no. 2, pp. 238–241, **1994**. DOI: 10.1103/PhysRevLett.72.238

[100] P. W. Snyder, M. R. Lockett, D. T. Moustakas, and G. M. Whitesides, "Is it the shape of the cavity, or the shape of the water in the cavity?" *The European Physical Journal Special Topics*, vol. 223, no. 5, pp. 853–891, **2013**. DOI: 10.1140/epjst/e2013-01818-y

[101] U. Raviv and J. Klein, "Fluidity of Bound Hydration Layers," *Science*, vol. 297, no. 5586, pp. 1540–1543, **2002**. DOI: 10.1126/science.1074481

[102] S. Leikin, V. A. Parsegian, D. C. Rau, and R. P. Rand, "Hydration Forces," *Annual Review of Physical Chemistry*, vol. 44, no. 1, pp. 369–395, **1993**. DOI: 10.1146/annurev.pc.44.100193.002101

[103] A. Pertsin, D. Platonov, and M. Grunze, "Origin of Short-Range Repulsion between Hydrated Phospholipid Bilayers: A Computer Simulation Study," *Langmuir*, vol. 23, no. 3, pp. 1388–1393, **2007**. DOI: 10.1021/la0622929

[104] N. Shenogina, R. Godawat, P. Keblinski, and S. Garde, "How Wetting and Adhesion Affect Thermal Conductance of a Range of Hydrophobic to Hydrophilic Aqueous Interfaces," *Physical Review Letters*, vol. 102, no. 15, p. 156101, **2009**. DOI: 10.1103/PhysRevLett.102.156101

[105] M. Kanduč, A. Schlaich, E. Schneck, and R. R. Netz, "Hydration repulsion between membranes and polar surfaces: Simulation approaches versus continuum theories," *Advances in Colloid and Interface Science*, vol. 208, pp. 142–152, **2014**. DOI: 10.1016/j.cis.2014.02.001

[106] S. McLaughlin, "The Electrostatic Properties of Membranes," *Annual Review of Biophysics and Biophysical Chemistry*, vol. 18, no. 1, pp. 113–136, **1989**. DOI: 10.1146/annurev.bb.18.060189.000553

[107] D. F. Evans and H. Wennerström, *The Colloidal Domain: Where Physics, Chemistry, Biology, and Technology Meet.* Wiley, 1999.

[108] R. F. Loring and S. Mukamel, "Molecular theory of solvation and dielectric response in polar fluids," *The Journal of Chemical Physics*, vol. 87, no. 2, pp. 1272–1283, **1987**. DOI: 10.1063/1.453311

[109] K. M. Dyer, J. S. Perkyns, G. Stell, and B. M. Pettitt, "Site-renormalised molecular fluid theory: on the utility of a two-site model of water," *Molecular Physics*, vol. 107, no. 4-6, pp. 423–431, **2009**. DOI: 10.1080/00268970902845313

[110] A. Levy, D. Andelman, and H. Orland, "Dielectric Constant of Ionic Solutions: A Field-Theory Approach," *Physical Review Letters*, vol. 108, no. 22, p. 227801, **2012**. DOI: 10.1103/PhysRevLett.108.227801

[111] V. Ballenegger and J.-P. Hansen, "Dielectric permittivity profiles of confined polar fluids," *The Journal of Chemical Physics*, vol. 122, no. 11, p. 114711, **2005**. DOI: 10.1063/1.1845431

[112] A. C. Maggs and R. Everaers, "Simulating Nanoscale Dielectric Response," *Physical Review Letters*, vol. 96, no. 23, p. 230603, **2006**. DOI: 10.1103/PhysRevLett.96.230603

[113] S. Buyukdagli and R. Blossey, "Dipolar correlations in structured solvents under nanoconfinement," *The Journal of Chemical Physics*, vol. 140, no. 23, p. 234903, **2014**. DOI: 10.1063/1.4881604

[114] S. Senapati and A. Chandra, “Dielectric Constant of Water Confined in a Nanocavity,” *The Journal of Physical Chemistry B*, vol. 105, no. 22, pp. 5106–5109, **2001**. DOI: 10.1021/jp011058i

[115] J. Faraudo and F. Bresme, “Anomalous Dielectric Behavior of Water in Ionic Newton Black Films,” *Physical Review Letters*, vol. 92, no. 23, p. 236102, **2004**. DOI: 10.1103/PhysRevLett.92.236102

[116] A. Ghoufi, A. Szymczyk, R. Renou, and M. Ding, “Calculation of local dielectric permittivity of confined liquids from spatial dipolar correlations,” *EPL (Europhysics Letters)*, vol. 99, no. 3, p. 37008, **2012**. DOI: 10.1209/0295-5075/99/37008

[117] V. A. Froltsov and S. H. L. Klapp, “Dielectric response of polar liquids in narrow slit pores,” *The Journal of Chemical Physics*, vol. 126, no. 11, p. 114703, **2007**. DOI: 10.1063/1.2566913

[118] S. Gekle and A. Arnold, “Comment on “Anomalous Dielectric Behavior of Nanoconfined Electrolytic Solutions”,” *Physical Review Letters*, vol. 111, no. 8, p. 089801, **2013**. DOI: 10.1103/PhysRevLett.111.089801

[119] H. Zhu, A. Ghoufi, A. Szymczyk, B. Balannec, and D. Morineau, “Reply: Anomalous Dielectric Behavior of Nanoconfined Electrolytic Solutions,” *Physical Review Letters*, vol. 111, no. 8, p. 089802, **2013**. DOI: 10.1103/PhysRevLett.111.089802

[120] M. González-Melchor, E. Mayoral, M. E. Velázquez, and J. Alejandre, “Electrostatic interactions in dissipative particle dynamics using the Ewald sums,” *The Journal of Chemical Physics*, vol. 125, no. 22, p. 224107, **2006**. DOI: 10.1063/1.2400223

[121] A. Moshfegh and A. Jabbarzadeh, “Fully explicit dissipative particle dynamics simulation of electroosmotic flow in nanochannels,” *Microfluidics and Nanofluidics*, vol. 20, no. 4, pp. 1–17, **2016**. DOI: 10.1007/s10404-016-1733-2

[122] H. A. Stern and S. E. Feller, “Calculation of the dielectric permittivity profile for a nonuniform system: Application to a lipid bilayer simulation,” *The Journal of Chemical Physics*, vol. 118, no. 7, pp. 3401–3412, **2003**. DOI: 10.1063/1.1537244

[123] M. Neumann, “Dipole moment fluctuation formulas in computer simulations of polar systems,” *Molecular Physics*, vol. 50, no. 4, pp. 841–858, **1983**. DOI: 10.1080/00268978300102721

[124] M. Rami Reddy and M. Berkowitz, “The dielectric constant of SPC/E water,” *Chemical Physics Letters*, vol. 155, no. 2, pp. 173–176, **1989**. DOI: 10.1016/0009-2614(89)85344-8

[125] M. Kanduč, E. Schneck, and R. R. Netz, “Attraction between hydrated hydrophilic surfaces,” *Chemical Physics Letters*, vol. 610–611, pp. 375–380, **2014**. DOI: 10.1016/j.cplett.2014.07.046

[126] M. J. Abraham, T. Murtola, R. Schulz, S. Páll, J. C. Smith, B. Hess, and E. Lindahl, “GROMACS: High performance molecular simulations through multi-level parallelism from laptops to supercomputers,” *SoftwareX*, vol. 1–2, pp. 19–25, **2015**. DOI: 10.1016/j.softx.2015.06.001

[127] N. Michaud-Agrawal, E. J. Denning, T. B. Woolf, and O. Beckstein, “MDAnalysis: A toolkit for the analysis of molecular dynamics simulations,” *Journal of Computational Chemistry*, vol. 32, no. 10, pp. 2319–2327, **2011**. DOI: 10.1002/jcc.21787

[128] U. Essmann, L. Perera, M. L. Berkowitz, T. Darden, H. Lee, and L. G. Pedersen, “A smooth particle mesh Ewald method,” *The Journal of Chemical Physics*, vol. 103, no. 19, pp. 8577–8593, **1995**. DOI: 10.1063/1.470117

[129] D. J. Bonthuis, S. Gekle, and R. R. Netz, “Profile of the Static Permittivity Tensor of Water at Interfaces: Consequences for Capacitance, Hydration Interaction and Ion Adsorption,” *Langmuir*, vol. 28, no. 20, pp. 7679–7694, **2012**. DOI: 10.1021/la2051564

[130] C. D. Lorenz, J. M. D. Lane, M. Chandross, M. J. Stevens, and G. S. Grest, “Molecular Dynamics Simulations of Water Confined between Matched Pairs of Hydrophobic and Hydrophilic Self-Assembled Monolayers,” *Langmuir*, vol. 25, no. 8, pp. 4535–4542, **2009**. DOI: 10.1021/la803940b

[131] L. Ramin and A. Jabbarzadeh, “Effect of Water on Structural and Frictional Properties of Self Assembled Monolayers,” *Langmuir*, vol. 29, no. 44, pp. 13 367–13 378, **2013**. DOI: 10.1021/la403321a

[132] O. Gereben and L. Pusztai, “On the accurate calculation of the dielectric constant from molecular dynamics simulations: The case of SPC/E and SWM4-DP water,” *Chemical Physics Letters*, vol. 507, no. 1–3, pp. 80–83, **2011**. DOI: 10.1016/j.cplett.2011.02.064

[133] J. B. Hasted, *Aqueous dielectrics.* Chapman and Hall, 1973.

[134] H. J. C. Berendsen, J. P. M. Postma, W. F. v. Gunsteren, A. DiNola, and J. R. Haak, “Molecular dynamics with coupling to an external bath,” *The Journal of Chemical Physics*, vol. 81, no. 8, pp. 3684–3690, **1984**. DOI: 10.1063/1.448118

[135] P. K. Persson and B. A. Bergenståhl, "Repulsive forces in lecithin glycol lamellar phases," *Biophysical Journal*, vol. 47, no. 5, pp. 743–746, **1985**. DOI: 10.1016/S0006-3495(85)83974-6

[136] H. K. Christenson and R. G. Horn, "Solvation forces measured in non-aqueous liquids," *Chemica scripta*, vol. 25, pp. 37–41, **1985**.

[137] N. Kuznetsova, D. C. Rau, V. A. Parsegian, and S. Leikin, "Solvent hydrogen-bond network in protein self-assembly: solvation of collagen triple helices in non-aqueous solvents," *Biophysical Journal*, vol. 72, no. 1, pp. 353–362, **1997**. DOI: 10.1016/S0006-3495(97)78674-0

[138] K. J. Mysels, "Solvation Forces in Soap Films," *Nature*, vol. 218, no. 5138, pp. 265–266, **1968**. DOI: 10.1038/218265a0

[139] R. M. Pashley and J. P. Quirk, "The effect of cation valency on DLVO and hydration forces between macroscopic sheets of muscovite mica in relation to clay swelling," *Colloids and Surfaces*, vol. 9, no. 1, pp. 1–17, **1984**. DOI: 10.1016/0166-6622(84)80138-9

[140] H. I. Petrache, N. Gouliaev, S. Tristram-Nagle, R. Zhang, R. M. Suter, and J. F. Nagle, "Interbilayer interactions from high-resolution x-ray scattering," *Physical Review E*, vol. 57, no. 6, pp. 7014–7024, **1998**.

[141] H. I. Petrache, T. Zemb, L. Belloni, and V. A. Parsegian, "Salt screening and specific ion adsorption determine neutral-lipid membrane interactions," *Proceedings of the National Academy of Sciences*, vol. 103, no. 21, pp. 7982–7987, **2006**. DOI: 10.1073/pnas.0509967103

[142] A. Aroti, E. Leontidis, M. Dubois, and T. Zemb, "Effects of Monovalent Anions of the Hofmeister Series on DPPC Lipid Bilayers Part I: Swelling and In-Plane Equations of State," *Biophysical Journal*, vol. 93, no. 5, pp. 1580–1590, **2007**. DOI: 10.1529/biophysj.106.094482

[143] E. Schneck, B. Demé, C. Gege, and M. Tanaka, "Membrane Adhesion via Homophilic Saccharide-Saccharide Interactions Investigated by Neutron Scattering," *Biophysical Journal*, vol. 100, no. 9, pp. 2151–2159, **2011**. DOI: 10.1016/j.bpj.2011.03.011

[144] N. Radić and S. Marčelja, "Solvent contribution to the debye screening length," *Chemical Physics Letters*, vol. 55, no. 2, pp. 377–379, **1978**. DOI: 10.1016/0009-2614(78)87043-2

[145] E. Ruckenstein and D. Schiby, “On the origin of repulsive hydration forces between two mica plates,” *Chemical Physics Letters*, vol. 95, no. 4–5, pp. 439–443, **1983**. DOI: 10.1016/0009-2614(83)80590-9

[146] P. Attard and M. T. Batchelor, “A mechanism for the hydration force demonstrated in a model system,” *Chemical Physics Letters*, vol. 149, no. 2, pp. 206–211, **1988**. DOI: 10.1016/0009-2614(88)87223-3

[147] S. J. Marrink, M. Berkowitz, and H. J. C. Berendsen, “Molecular dynamics simulation of a membrane/water interface: the ordering of water and its relation to the hydration force,” *Langmuir*, vol. 9, no. 11, pp. 3122–3131, **1993**. DOI: 10.1021/la00035a062

[148] U. Essmann, L. Perera, and M. L. Berkowitz, “The origin of the hydration interaction of lipid bilayers from MD simulation of dipalmitoylphosphatidylcholine membranes in gel and liquid crystalline phases,” *Langmuir*, vol. 11, no. 11, pp. 4519–4531, **1995**.

[149] M. Kanduč, A. Schlaich, A. H. d. Vries, J. Jouhet, E. Maréchal, B. Demé, R. R. Netz, and E. Schneck, “Tight cohesion between glycolipid membranes results from balanced water–headgroup interactions,” *Nature Communications*, vol. 8, p. 14899, **2017**. DOI: 10.1038/ncomms14899

[150] A. A. Kornyshev and S. Leikin, “Fluctuation theory of hydration forces: The dramatic effects of inhomogeneous boundary conditions,” *Physical Review A*, vol. 40, no. 11, pp. 6431–6437, **1989**. DOI: 10.1103/PhysRevA.40.6431

[151] S. Leikin and A. A. Kornyshev, “Mean-field theory of dehydration transitions,” *Physical Review A*, vol. 44, no. 2, pp. 1156–1168, **1991**. DOI: 10.1103/PhysRevA.44.1156

[152] S. Kirchner and G. Cevc, “Hydration of polar interfaces. A generalised mean-field model,” *Journal of the Chemical Society, Faraday Transactions*, vol. 90, no. 13, pp. 1941–1951, **1994**. DOI: 10.1039/FT9949001941

[153] R. Podgornik and B. ZEKS, “Hydration force and hydration regulation,” *STUDIA BIOPHYSICA*, vol. 111, no. 2-3, pp. 135–142, **1986**.

[154] S. Y. Bhide and M. L. Berkowitz, “Structure and dynamics of water at the interface with phospholipid bilayers,” *The Journal of Chemical Physics*, vol. 123, no. 22, pp. 224 702–224 702–16, **2005**. DOI: doi:10.1063/1.2132277

[155] H. Fröhlich, *Theory of dielectrics: dielectric constant and dielectric loss.* Clarendon Press, 1958.

[156] A. Schlaich, E. W. Knapp, and R. R. Netz, "Water Dielectric Effects in Planar Confinement," *Physical Review Letters*, vol. 117, no. 4, p. 048001, **2016**. DOI: 10.1103/PhysRevLett.117.048001

[157] K. Gawrisch, D. Ruston, J. Zimmerberg, V. A. Parsegian, R. P. Rand, and N. Fuller, "Membrane dipole potentials, hydration forces, and the ordering of water at membrane surfaces." *Biophysical Journal*, vol. 61, no. 5, pp. 1213–1223, **1992**.

[158] N. Markova, E. Sparr, L. Wadsö, and H. Wennerström, "A Calorimetric Study of Phospholipid Hydration. Simultaneous Monitoring of Enthalpy and Free Energy," *The Journal of Physical Chemistry B*, vol. 104, no. 33, pp. 8053–8060, **2000**. DOI: 10.1021/jp001020q

[159] G. Cevc, M. Hauser, and A. A. Kornyshev, "Effects of the Interfacial Structure on the Hydration Forces between Laterally Uniform Surfaces," *Langmuir*, vol. 11, no. 8, pp. 3103–3110, **1995**. DOI: 10.1021/la00008a041

[160] S. Páll, M. J. Abraham, C. Kutzner, B. Hess, and E. Lindahl, "Tackling Exascale Software Challenges in Molecular Dynamics Simulations with GROMACS," in *Solving Software Challenges for Exascale.* Springer, Cham, 2014, pp. 3–27.

[161] M. R. Shirts and J. D. Chodera, "Statistically optimal analysis of samples from multiple equilibrium states," *The Journal of Chemical Physics*, vol. 129, no. 12, p. 124105, **2008**. DOI: 10.1063/1.2978177

[162] D. P. Tieleman and H. J. C. Berendsen, "Molecular dynamics simulations of a fully hydrated dipalmitoylphosphatidylcholine bilayer with different macroscopic boundary conditions and parameters," *The Journal of Chemical Physics*, vol. 105, no. 11, pp. 4871–4880, **1996**. DOI: 10.1063/1.472323

[163] E. Lindahl and O. Edholm, "Mesoscopic Undulations and Thickness Fluctuations in Lipid Bilayers from Molecular Dynamics Simulations," *Biophysical Journal*, vol. 79, no. 1, pp. 426–433, **2000**. DOI: 10.1016/S0006-3495(00)76304-1

[164] T. Schubert, E. Schneck, and M. Tanaka, "First order melting transitions of highly ordered dipalmitoyl phosphatidylcholine gel phase membranes in molecular dynamics simulations with atomistic detail," *The Journal of Chemical Physics*, vol. 135, no. 5, p. 055105, **2011**. DOI: 10.1063/1.3615937

[165] G. Bussi, D. Donadio, and M. Parrinello, "Canonical sampling through velocity rescaling," *The Journal of Chemical Physics*, vol. 126, no. 1, p. 014101, **2007**. DOI: 10.1063/1.2408420

[166] B. Kowalik, T. Schubert, H. Wada, M. Tanaka, R. R. Netz, and E. Schneck, "Combination of MD Simulations with Two-State Kinetic Rate Modeling Elucidates the Chain Melting Transition of Phospholipid Bilayers for Different Hydration Levels," *The Journal of Physical Chemistry B*, vol. 119, no. 44, pp. 14 157–14 167, **2015**. DOI: 10.1021/acs.jpcb.5b05501

[167] P. S. Coppock and J. T. Kindt, "Determination of Phase Transition Temperatures for Atomistic Models of Lipids from Temperature-Dependent Stripe Domain Growth Kinetics," *The Journal of Physical Chemistry B*, vol. 114, no. 35, pp. 11 468–11 473, **2010**. DOI: 10.1021/jp104529m

[168] J. Ulminus, H. Wennerström, G. Lindblom, and G. Arvidson, "Deuteron nuclear magnetic resonance studies of phase equilibriums in a lecithin-water system," *Biochemistry*, vol. 16, no. 26, pp. 5742–5745, **1977**. DOI: 10.1021/bi00645a014

[169] C. Grabielle-Madelmont and R. Perron, "Calorimetric studies on phospholipid—water systems," *Journal of Colloid and Interface Science*, vol. 95, no. 2, pp. 471–482, **1983**. DOI: 10.1016/0021-9797(83)90207-2

[170] M. Kanduč, E. Schneck, and R. R. Netz, "Hydration Interaction between Phospholipid Membranes: Insight into Different Measurement Ensembles from Atomistic Molecular Dynamics Simulations," *Langmuir*, vol. 29, no. 29, pp. 9126–9137, **2013**. DOI: 10.1021/la401147b

[171] I.-C. Yeh and M. L. Berkowitz, "Ewald summation for systems with slab geometry," *The Journal of Chemical Physics*, vol. 111, no. 7, pp. 3155–3162, **1999**. DOI: 10.1063/1.479595

[172] M. G. Cottam, D. R. Tilley, and B. Zeks, "Theory of surface modes in ferroelectrics," *Journal of Physics C: Solid State Physics*, vol. 17, no. 10, p. 1793, **1984**. DOI: 10.1088/0022-3719/17/10/022

[173] A. Schlaich, B. Kowalik, M. Kanduč, E. Schneck, and R. R. Netz, "Physical mechanisms of the interaction between lipid membranes in the aqueous environment," *Physica A: Statistical Mechanics and its Applications*, vol. 418, pp. 105–125, **2015**. DOI: 10.1016/j.physa.2014.06.088

[174] D. Andelman, "Chapter 12 Electrostatic properties of membranes: The poisson-boltzmann theory," in *Handbook of Biological Physics*, ser. Structure and Dynamics of Membranes, R. Lipowsky and E. Sackmann, Ed. North-Holland, 1995, vol. Volume 1, pp. 603–642.

[175] A. G. Moreira and R. R. Netz, "Strong-coupling theory for counter-ion distributions," *Europhysics Letters (EPL)*, vol. 52, no. 6, pp. 705–711, **2000**. DOI: 10.1209/epl/i2000-00495-1

[176] M. Kanduč and R. R. Netz, "From hydration repulsion to dry adhesion between asymmetric hydrophilic and hydrophobic surfaces," *Proceedings of the National Academy of Sciences*, vol. 112, no. 40, pp. 12 338–12 343, **2015**. DOI: 10.1073/pnas.1504919112

[177] A. Khan, B. Joensson, and H. Wennerström, "Phase equilibria in the mixed sodium and calcium di-2-ethylhexylsulfosuccinate aqueous system. An illustration of repulsive and attractive double-layer forces," *The Journal of Physical Chemistry*, vol. 89, no. 24, pp. 5180–5184, **1985**. DOI: 10.1021/j100270a012

[178] H. Wennerström, A. Khan, and B. Lindman, "Ionic surfactants with divalent counterions," *Advances in Colloid and Interface Science*, vol. 34, pp. 433–449, **1991**. DOI: 10.1016/0001-8686(91)80054-N

[179] M. Turesson, J. Forsman, T. Åkesson, and B. Jönsson, "Simulation of Phase Equilibria in Lamellar Surfactant Systems," *Langmuir*, vol. 20, no. 12, pp. 5123–5126, **2004**. DOI: 10.1021/la049858i

[180] S. Rentsch, H. Siegenthaler, and G. Papastavrou, "Diffuse Layer Properties of Thiol-Modified Gold Electrodes Probed by Direct Force Measurements," *Langmuir*, vol. 23, no. 17, pp. 9083–9091, **2007**. DOI: 10.1021/la700987u

[181] V. Kuznetsov and G. Papastavrou, "Ion Adsorption on Modified Electrodes as Determined by Direct Force Measurements under Potentiostatic Control," *The Journal of Physical Chemistry C*, vol. 118, no. 5, pp. 2673–2685, **2014**. DOI: 10.1021/jp500425g

[182] M. Kanduč, A. Schlaich, E. Schneck, and R. R. Netz, "Water-Mediated Interactions between Hydrophilic and Hydrophobic Surfaces," *Langmuir*, vol. 32, no. 35, pp. 8767–8782, **2016**. DOI: 10.1021/acs.langmuir.6b01727

[183] D. Horinek, S. I. Mamatkulov, and R. R. Netz, "Rational design of ion force fields based on thermodynamic solvation properties," *The Journal of Chemical Physics*, vol. 130, no. 12, p. 124507, **2009**. DOI: 10.1063/1.3081142

[184] D. E. Smith and L. X. Dang, "Computer simulations of NaCl association in polarizable water," *The Journal of Chemical Physics*, vol. 100, no. 5, pp. 3757–3766, **1994**. DOI: 10.1063/1.466363

[185] D. J. Bonthuis, Y. Uematsu, and R. R. Netz, “Interfacial layer effects on surface capacitances and electro-osmosis in electrolytes,” *Phil. Trans. R. Soc. A*, vol. 374, no. 2060, p. 20150033, **2016**. DOI: 10.1098/rsta.2015.0033

[186] N. Schwierz, D. Horinek, and R. R. Netz, “Specific Ion Binding to Carboxylic Surface Groups and the pH Dependence of the Hofmeister Series,” *Langmuir*, vol. 31, no. 1, pp. 215–225, **2015**. DOI: 10.1021/la503813d

[187] S. Dewan, V. Carnevale, A. Bankura, A. Eftekhari-Bafrooei, G. Fiorin, M. L. Klein, and E. Borguet, “Structure of Water at Charged Interfaces: A Molecular Dynamics Study,” *Langmuir*, vol. 30, no. 27, pp. 8056–8065, **2014**. DOI: 10.1021/la5011055

[188] K. F. Rinne, S. Gekle, and R. R. Netz, “Dissecting ion-specific dielectric spectra of sodium-halide solutions into solvation water and ionic contributions,” *The Journal of Chemical Physics*, vol. 141, no. 21, p. 214502, **2014**. DOI: 10.1063/1.4901927

[189] M. Kanduč and R. Podgornik, “Electrostatic image effects for counterions between charged planar walls,” *The European Physical Journal E*, vol. 23, no. 3, pp. 265–274, **2007**. DOI: 10.1140/epje/i2007-10187-2

[190] Y. S. Jho, M. Kanduč, A. Naji, R. Podgornik, M. W. Kim, and P. A. Pincus, “Strong-Coupling Electrostatics in the Presence of Dielectric Inhomogeneities,” *Physical Review Letters*, vol. 101, no. 18, p. 188101, **2008**. DOI: 10.1103/PhysRevLett.101.188101

[191] A. G. Moreira and R. R. Netz, “Counterions at charge-modulated substrates,” *Europhysics Letters (EPL)*, vol. 57, no. 6, pp. 911–917, **2002**. DOI: 10.1209/epl/i2002-00597-2

[192] D. B. Lukatsky, S. A. Safran, A. W. C. Lau, and P. Pincus, “Enhanced counterion localization induced by surface charge modulation,” *EPL (Europhysics Letters)*, vol. 58, no. 5, p. 785, **2002**. DOI: 10.1209/epl/i2002-00418-8

[193] D. B. Lukatsky and S. A. Safran, “Universal reduction of pressure between charged surfaces by long-wavelength surface charge modulation,” *EPL (Europhysics Letters)*, vol. 60, no. 4, p. 629, **2002**. DOI: 10.1209/epl/i2002-00264-2

[194] Y. S. Jho, G. Park, C. S. Chang, P. Pincus, and M. W. Kim, “Interaction between two inhomogeneously charged parallel surfaces in the strong coupling regime,” *Physical Review E*, vol. 73, no. 2, p. 021502, **2006**. DOI: 10.1103/PhysRevE.73.021502

[195] W. Pezeshkian, N. Nikoofard, D. Norouzi, F. Mohammad-Rafiee, and H. Fazli, "Distribution of counterions and interaction between two similarly charged dielectric slabs: Roles of charge discreteness and dielectric inhomogeneity," *Physical Review E*, vol. 85, no. 6, p. 061925, **2012**. DOI: 10.1103/PhysRevE.85.061925

[196] D. B. Hough and L. R. White, "The calculation of hamaker constants from liftshitz theory with applications to wetting phenomena," *Advances in Colloid and Interface Science*, vol. 14, no. 1, pp. 3–41, **1980**. DOI: 10.1016/0001-8686(80)80006-6

[197] H. Oshima, Y. Inoko, and T. Mitsui, "Hamaker constant and binding constants of Ca2+ and Mg2+ in dipalmitoyl phosphatidylcholine/water system," *Journal of Colloid and Interface Science*, vol. 86, no. 1, pp. 57–72, **1982**. DOI: 10.1016/0021-9797(82)90041-8

[198] A. P. dos Santos, M. Girotto, and Y. Levin, "Simulations of Coulomb systems with slab geometry using an efficient 3D Ewald summation method," *The Journal of Chemical Physics*, vol. 144, no. 14, p. 144103, **2016**. DOI: 10.1063/1.4945560

[199] S. Engstrom and H. Wennerström, "Ion condensation on planar surfaces. A solution of the Poisson-Boltzmann equation for two parallel charged plates," *The Journal of Physical Chemistry*, vol. 82, no. 25, pp. 2711–2714, **1978**. DOI: 10.1021/j100514a017

[200] D. Andelman, "Introduction to electrostatics in soft and biological matter," *Proceedings of the Nato ASI & SUSSP on Soft condensed matter physics in molecular and cell biology*, pp. 97–122, **2006**.

[201] F. Bowden and D. Tabor, *The Friction and Lubrication of Solids.* Oxford: Clarendon Press, 1950.

[202] J. Gao, W. D. Luedtke, D. Gourdon, M. Ruths, J. N. Israelachvili, and U. Landman, "Frictional Forces and Amontons' Law: From the Molecular to the Macroscopic Scale," *The Journal of Physical Chemistry B*, vol. 108, no. 11, pp. 3410–3425, **2004**. DOI: 10.1021/jp036362l

[203] H. Sakuma, K. Otsuki, and K. Kurihara, "Viscosity and Lubricity of Aqueous NaCl Solution Confined between Mica Surfaces Studied by Shear Resonance Measurement," *Physical Review Letters*, vol. 96, no. 4, p. 046104, **2006**. DOI: 10.1103/PhysRevLett.96.046104

[204] T.-D. Li, J. Gao, R. Szoszkiewicz, U. Landman, and E. Riedo, "Structured and viscous water in subnanometer gaps," *Physical Review B*, vol. 75, no. 11, p. 115415, **2007**. DOI: 10.1103/PhysRevB.75.115415

[205] A. Labuda, K. Kobayashi, K. Suzuki, H. Yamada, and P. Grütter, "Monotonic Damping in Nanoscopic Hydration Experiments," *Physical Review Letters*, vol. 110, no. 6, p. 066102, **2013**. DOI: 10.1103/PhysRevLett.110.066102

[206] S. H. Khan, G. Matei, S. Patil, and P. M. Hoffmann, "Dynamic Solidification in Nanoconfined Water Films," *Physical Review Letters*, vol. 105, no. 10, p. 106101, **2010**. DOI: 10.1103/PhysRevLett.105.106101

[207] N. Dhopatkar, A. P. Defante, and A. Dhinojwala, "Ice-like water supports hydration forces and eases sliding friction," *Science Advances*, vol. 2, no. 8, p. e1600763, **2016**. DOI: 10.1126/sciadv.1600763

[208] A. Maali, T. Cohen-Bouhacina, G. Couturier, and J.-P. Aimé, "Oscillatory Dissipation of a Simple Confined Liquid," *Physical Review Letters*, vol. 96, no. 8, p. 086105, **2006**. DOI: 10.1103/PhysRevLett.96.086105

[209] S. C. Clear and P. F. Nealey, "Chemical Force Microscopy Study of Adhesion and Friction between Surfaces Functionalized with Self-Assembled Monolayers and Immersed in Solvents," *Journal of Colloid and Interface Science*, vol. 213, no. 1, pp. 238–250, **1999**. DOI: 10.1006/jcis.1999.6139

[210] J. Chen, I. Ratera, J. Y. Park, and M. Salmeron, "Velocity Dependence of Friction and Hydrogen Bonding Effects," *Physical Review Letters*, vol. 96, no. 23, p. 236102, **2006**. DOI: 10.1103/PhysRevLett.96.236102

[211] R. C. Major, J. E. Houston, M. J. McGrath, J. I. Siepmann, and X.-Y. Zhu, "Viscous Water Meniscus under Nanoconfinement," *Physical Review Letters*, vol. 96, no. 17, p. 177803, **2006**. DOI: 10.1103/PhysRevLett.96.177803

[212] R. Villey, E. Martinot, C. Cottin-Bizonne, M. Phaner-Goutorbe, L. Léger, F. Restagno, and E. Charlaix, "Effect of Surface Elasticity on the Rheology of Nanometric Liquids," *Physical Review Letters*, vol. 111, no. 21, p. 215701, **2013**. DOI: 10.1103/PhysRevLett.111.215701

[213] S. H. Lee and P. J. Rossky, "A comparison of the structure and dynamics of liquid water at hydrophobic and hydrophilic surfaces—a molecular dynamics simulation study," *The Journal of Chemical Physics*, vol. 100, no. 4, pp. 3334–3345, **1994**. DOI: 10.1063/1.466425

[214] Y. Leng and P. T. Cummings, "Fluidity of Hydration Layers Nanoconfined between Mica Surfaces," *Physical Review Letters*, vol. 94, no. 2, p. 026101, **2005**. DOI: 10.1103/PhysRevLett.94.026101

[215] J. M. D. Lane, M. Chandross, M. J. Stevens, and G. S. Grest, "Water in Nanoconfinement between Hydrophilic Self-Assembled Monolayers," *Langmuir*, vol. 24, no. 10, pp. 5209–5212, **2008**. DOI: 10.1021/la704005v

[216] I. Fedyanin, A. Pertsin, and M. Grunze, "Quasistatic computer simulations of shear behavior of water nanoconfined between mica surfaces," *The Journal of Chemical Physics*, vol. 135, no. 17, p. 174704, **2011**. DOI: 10.1063/1.3657858

[217] C. Sendner, D. Horinek, L. Bocquet, and R. R. Netz, "Interfacial Water at Hydrophobic and Hydrophilic Surfaces: Slip, Viscosity, and Diffusion," *Langmuir*, vol. 25, no. 18, pp. 10 768–10 781, **2009**. DOI: 10.1021/la901314b

[218] A. Boţan, L. Joly, N. Fillot, and C. Loison, "Mixed Mechanism of Lubrication by Lipid Bilayer Stacks," *Langmuir*, vol. 31, no. 44, pp. 12 197–12 202, **2015**. DOI: 10.1021/acs.langmuir.5b02786

[219] P. A. Thompson and M. O. Robbins, "Shear flow near solids: Epitaxial order and flow boundary conditions," *Physical Review A*, vol. 41, no. 12, pp. 6830–6837, **1990**. DOI: 10.1103/PhysRevA.41.6830

[220] R. Zangi and A. E. Mark, "Monolayer Ice," *Physical Review Letters*, vol. 91, no. 2, p. 025502, **2003**. DOI: 10.1103/PhysRevLett.91.025502

[221] B. Halle and M. Davidovic, "Biomolecular hydration: From water dynamics to hydrodynamics," *Proceedings of the National Academy of Sciences*, vol. 100, no. 21, pp. 12 135–12 140, **2003**. DOI: 10.1073/pnas.2033320100

[222] W. H. Briscoe, "Aqueous boundary lubrication: Molecular mechanisms, design strategy, and terra incognita," *Current Opinion in Colloid & Interface Science*, vol. 27, pp. 1–8, **2017**. DOI: 10.1016/j.cocis.2016.09.002

[223] R. Zwanzig, "Time-Correlation Functions and Transport Coefficients in Statistical Mechanics," *Annual Review of Physical Chemistry*, vol. 16, no. 1, pp. 67–102, **1965**. DOI: 10.1146/annurev.pc.16.100165.000435

[224] P. J. Daivis and D. J. Evans, "Comparison of constant pressure and constant volume nonequilibrium simulations of sheared model decane," *The Journal of Chemical Physics*, vol. 100, no. 1, pp. 541–547, **1994**. DOI: 10.1063/1.466970

[225] T. Chen, B. Smit, and A. T. Bell, "Are pressure fluctuation-based equilibrium methods really worse than nonequilibrium methods for calculating viscosities?" *The Journal of Chemical Physics*, vol. 131, no. 24, p. 246101, **2009**. DOI: 10.1063/1.3274802

[226] D. J. Bonthuis, D. Horinek, L. Bocquet, and R. R. Netz, “Electrohydraulic Power Conversion in Planar Nanochannels,” *Physical Review Letters*, vol. 103, no. 14, p. 144503, **2009**. DOI: 10.1103/PhysRevLett.103.144503

[227] A. Gaisinskaya, L. Ma, G. Silbert, R. Sorkin, O. Tairy, R. Goldberg, N. Kampf, and J. Klein, “Hydration lubrication: exploring a new paradigm,” *Faraday Discussions*, vol. 156, no. 0, pp. 217–233, **2012**. DOI: 10.1039/C2FD00127F

[228] B. Widom, “Some Topics in the Theory of Fluids,” *The Journal of Chemical Physics*, vol. 39, no. 11, pp. 2808–2812, **1963**. DOI: 10.1063/1.1734110

[229] A. Schlaich, “Modified GROMACS sources for TPI insertion into a slab; available on GitHub,” **2014**.

[230] T. Oliphant, “A Bayesian perspective on estimating mean, variance, and standard-deviation from data,” *All Faculty Publications*, **2006**.

Erklärung

Hiermit erkläre ich, dass ich die vorliegende Dissertationsschrift mit dem Titel

Water effects on the interaction and friction between polar surfaces

selbständig angefertigt und hierfür keine anderen als die angegebenen Hilfsmittel verwendet habe. Die Arbeit ist weder in einem früheren Promotionsverfahren angenommen noch als ungenügend beurteilt worden.

Berlin, den 12. Juli 2017

Danksagung

An dieser Stelle möchte ich mich bei all denjenigen bedanken, die mich während meiner Promotion unterstützt haben. An allererster Stelle möchte ich meine Familie nennen, meinen wunderbaren Sohn Leandro und meine Frau Riccarda - ohne eure Unterstützung wäre diese Arbeit nicht zu Stande gekommen. Großer Dank gilt meinem Doktorvater Prof. Dr. Roland Netz für die stets gute Betreuung während der letzten Jahre, viele Diskussionen und der Vermittlung umfangreichen Wissens der theoretischen Physik. Ich bedanke mich bei Prof. Dr. Joachim Dzubiella für die Übernahme der Zweitbegutachtung dieser Arbeit.

Ich bedanke mich für die anregenden Diskussionen und die Entwicklung der Forschungsprojekte bei meinen Koautoren und Kollegen, insbesondere Emanuel Schneck, Matej Kanduč, Bartosz Kowalik, Julian Kappler und Jan Daldrop, sowie Sunsanne Liese, Philip Loche, Douwe Bonthuis und Julius Schulz für ihre Hilfe bei allen forschungs- und technischen Problemen. Allen ehemaligen und aktuellen Kollegen und Annette Schumann-Welde danke ich für die immer angenehme Arbeitsatmosphäre und Unterstützung wann immer es nötig war. Dank auch an Stefan Kesselheim, der mich für theoretische Physik und Soft Matter begeistert hat. Besonders hervorheben möchte ich hier noch Jens Dreger, ohne dessen Engagement und Improvisation für die Bereitstellung von Rechenzeit diese Arbeit so nicht möglich gewesen wäre.